



## Review

# Electrosynthesis of H<sub>2</sub>O<sub>2</sub> through a two-electron oxygen reduction reaction by carbon based catalysts: From mechanism, catalyst design to electrode fabrication

Jingkun An <sup>a</sup>, Yujie Feng <sup>a,b,\*\*</sup>, Qian Zhao <sup>c</sup>, Xin Wang <sup>c</sup>, Jia Liu <sup>a</sup>, Nan Li <sup>a,\*</sup><sup>a</sup> School of Environmental Science and Engineering, Academy of Environment and Ecology, Tianjin University, No. 92 Weijin Road, Nankai District, Tianjin, 300072, China<sup>b</sup> State Key Laboratory of Urban Water Resource and Environment, Harbin Institute of Technology, No. 73 Huanghe Road, Nangang District, Harbin, 150090, China<sup>c</sup> MOE Key Laboratory of Pollution Processes and Environmental Criteria, Tianjin Key Laboratory of Environmental Remediation and Pollution Control, Nankai University, No. 38 Tongyan Road, Jinnan District, Tianjin, 300350, China

## ARTICLE INFO

## Article history:

Received 16 December 2021

Received in revised form

24 March 2022

Accepted 24 March 2022

## Keywords:

H<sub>2</sub>O<sub>2</sub> production  
Oxygen reduction reaction  
Catalytic mechanism  
Catalyst design  
Electrode fabrication

## ABSTRACT

Hydrogen peroxide (H<sub>2</sub>O<sub>2</sub>) is an efficient oxidant with multiple uses ranging from chemical synthesis to wastewater treatment. The in-situ H<sub>2</sub>O<sub>2</sub> production via a two-electron oxygen reduction reaction (ORR) will bring H<sub>2</sub>O<sub>2</sub> beyond its current applications. The development of carbon materials offers the hope for obtaining inexpensive and high-performance alternatives to substitute noble-metal catalysts in order to provide a full and comprehensive picture of the current state of the art treatments and inspire new research in this area. Herein, the most up-to-date findings in theoretical predictions, synthetic methodologies, and experimental investigations of carbon-based catalysts are systematically summarized. Various electrode fabrication and modification methods were also introduced and compared, along with our original research on the air-breathing cathode and three-phase interface theory inside a porous electrode. In addition, our current understanding of the challenges, future directions, and suggestions on the carbon-based catalyst designs and electrode fabrication are highlighted.

© 2022 Published by Elsevier B.V. on behalf of Chinese Society for Environmental Sciences, Harbin Institute of Technology, Chinese Research Academy of Environmental Sciences. This is an open access article under the CC BY-NC-ND license (<http://creativecommons.org/licenses/by-nc-nd/4.0/>).

## 1. Introduction

1.1. Multiple applications of H<sub>2</sub>O<sub>2</sub>

Hydrogen peroxide (H<sub>2</sub>O<sub>2</sub>) is a universal oxidizing agent which can be utilized either alone or in combination with other reagents for various purposes, such as pulp and textile bleaching [1], chemical synthesis [2], and wastewater treatment [3]. In the environmental field, H<sub>2</sub>O<sub>2</sub> is used in many advanced oxidation processes (AOPs), such as H<sub>2</sub>O<sub>2</sub>/UV, H<sub>2</sub>O<sub>2</sub>/Fe<sup>2+</sup>, and H<sub>2</sub>O<sub>2</sub>/O<sub>3</sub> [4]. In these H<sub>2</sub>O<sub>2</sub>-based AOPs, strong oxidant ·OH radicals (E°(·OH/H<sub>2</sub>O) = 2.80 V<sub>SHE</sub>) are generated in situ. Afterwards, this free radical

can non-selectively oxidize various contaminants at relatively high rate constants in the order of 10<sup>6</sup>-10<sup>10</sup> M<sup>-1</sup> s<sup>-1</sup> [5]. Moreover, the self-quenching of ·OH radicals makes their lifetime in water as short as a few nanoseconds [5]. AOPs have been widely applied for the degradation of various pollutants such as antibiotics, herbicides, insecticides, endocrine-disrupting chemicals, pharmaceutical and personal care products (PPCPs), and effluent organic matter [6], showing their potential for water and wastewater treatment in the future [7,8].

1.2. Current status of H<sub>2</sub>O<sub>2</sub> production

## 1.2.1. Anthraquinone oxidation process

Currently, over 95% of commercially produced H<sub>2</sub>O<sub>2</sub> worldwide is derived from the anthraquinone oxidation (AO) process (the alternate name is auto-oxidation process) [9]. Hydrogen, anthraquinone, and air are employed as raw materials in the AO process. The alkylanthraquinone precursor dissolved in an admixture of

\* Corresponding author.

\*\* Corresponding author. School of Environmental Science and Engineering, Academy of Environment and ecology, Tianjin University, No. 92 Weijin Road, Nankai District, Tianjin, 300072, China.

E-mail address: [nli@tju.edu.cn](mailto:nli@tju.edu.cn) (N. Li).

## Abbreviations

### Carbon materials

AC	activated carbon
CB	carbon black
CF/GF	carbon felt/graphite felt
CNF	carbon nanofiber
CNT	carbon nanotube
EEGr	electrochemically exfoliated graphene
HPC	hierarchical porous carbons
MC	mesoporous carbon
MWCNT	multiwall carbon nanotube
OMC	ordered mesoporous carbon
rGO	reduced graphene oxide
RVC	reticulated vitreous carbon
RSAC	reed straw activated carbon
SPG	spectrographically pure graphite
SWCNT	single-wall carbon nanotube

### Techniques & systems

BES	bioelectrochemical system
DFT	density functional theory
EAOP	electrochemical advanced oxidation process
HER	hydrogen evolution reaction
LCD	liquid crystal display

MAS	magic angle spinning
MEC	microbial electrolysis cell
MFC	microbial fuel cell
NMR	nuclear magnetic resonance
OER	oxygen evolution reaction
ORR	oxygen reduction reaction
PC	peroxy-coagulation
POP	persistent organic pollution
RDE	rotating disk electrode
RRDE	rotating ring-disk electrode
SRS	statistical Raman spectroscopy

### Reagents

AQDS	anthraquinonedisulphonate
BMP-dca	N-butyl-3-methylpyridinium dicyanamide
CoPPy	Co-polypyrrole
CoTMPP	cobalt tetra-methoxy-phenyl porphyrin
DHN	dihydroxynaphthalene
EMIM-dca	1-Ethyl-3-methylimidazolium dicyanamide
HMT	hexamine
PANI	polyaniline
PEI	polyethylenimine
Ppy	Polypyrrole
PTFE	polytetrafluoroethylene
TBAQ	tert-butyl-antraquinone
TETA	Triethylenetetramine

organic solvents is catalytically hydrogenated and then oxidized to obtain a diluted solution of  $\text{H}_2\text{O}_2$  at 0.9–1.8% (wt). The following liquid-liquid extraction and distillation processes produce concentrated  $\text{H}_2\text{O}_2$  solution at 35–50% (wt) (Fig. 1a). The major drawbacks of the AO process are (1) the use of large quantities of hazardous organic solvents, (2) highly concentrated  $\text{H}_2\text{O}_2$  is explosive, which brings potential risks during transport and

storage, (3) about 0.1% (wt)  $\text{H}_2\text{O}_2$  at most is needed in the wastewater treatment process, which makes the concentration-dilution process a waste of cost and energy. These disadvantages and the decentralized requirements of users motivated the academic community and industry to develop other  $\text{H}_2\text{O}_2$  synthesis methods and go beyond the AO process.

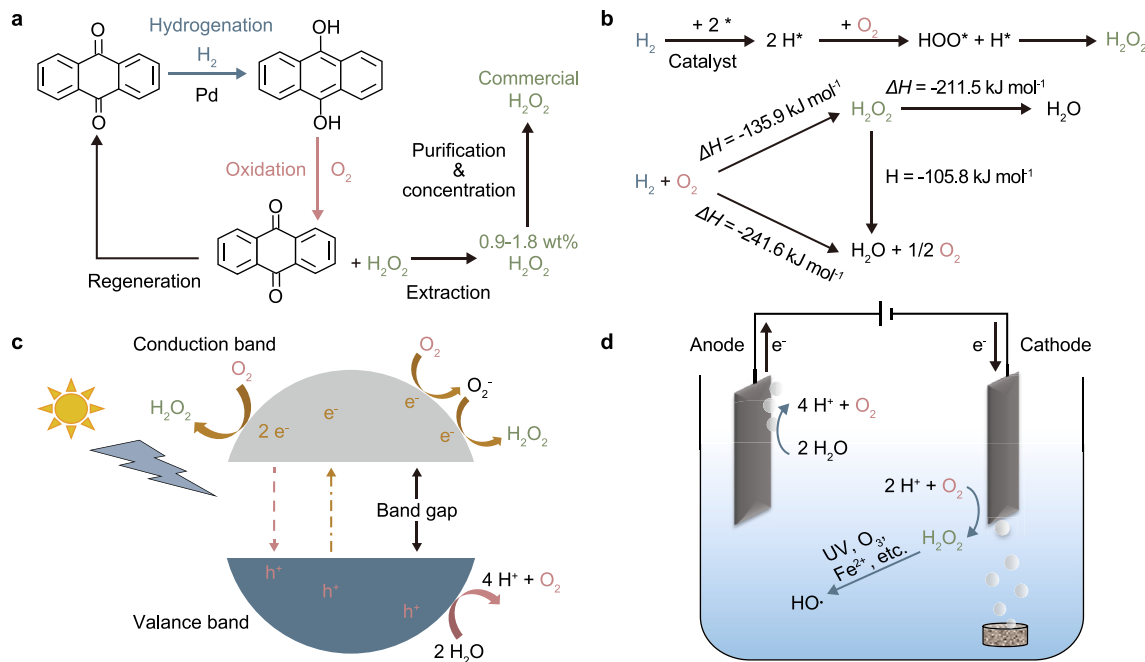


**Fig. 1.** **a**, Schematic of the anthraquinone process. **b**, The direct synthesis of  $\text{H}_2\text{O}_2$  from  $\text{H}_2$  and  $\text{O}_2$ . **c**, The Photo-catalysis to generate  $\text{H}_2\text{O}_2$ . **d**, The electrochemical  $\text{H}_2\text{O}_2$  production.

### 1.2.2. Direct synthesis

An alternative method is the direct synthesis of H<sub>2</sub>O<sub>2</sub> from H<sub>2</sub> and O<sub>2</sub>. In this straightforward batch process [10], gaseous H<sub>2</sub> and O<sub>2</sub> are introduced into the liquid medium with catalysts. The proposed catalytic mechanism for direct synthesis is sequential hydrogenation of molecular oxygen. Firstly, the H<sub>2</sub> molecule is dissociated into H atoms on the surface of the catalyst. Afterwards, an O<sub>2</sub> molecule adsorbs onto the surface of the catalyst, followed by reacting with the H atom and thus forming the HOO\* intermediate. H<sub>2</sub>O<sub>2</sub> is finally obtained by hydrogenating the HOO\* intermediate (Fig. 1b) [11]. Although the first patent was granted in 1914, there is still no industrial process based on the direct synthesis for over 100 years because of the following three critical disadvantages [12,13]: (1) Safety - the direct synthesis avoids transportation of H<sub>2</sub>O<sub>2</sub> to the site, but H<sub>2</sub> is more explosive relative to H<sub>2</sub>O<sub>2</sub>. The H<sub>2</sub> and O<sub>2</sub> mixture gas has to be diluted by other “inert” gases (N<sub>2</sub> or CO<sub>2</sub>) to operate below the lowest explosive limit, which also limits the productivity of H<sub>2</sub>O<sub>2</sub>; (2) Competing side reactions - the hydrogenation of O<sub>2</sub> towards H<sub>2</sub>O<sub>2</sub> ( $\Delta H = -135.9 \text{ kJ mol}^{-1}$ ) is along with the direct formation of H<sub>2</sub>O ( $\Delta H = -241.6 \text{ kJ mol}^{-1}$ ), the further reduction to H<sub>2</sub>O ( $\Delta H = -105.8 \text{ kJ mol}^{-1}$ ) and H<sub>2</sub>O<sub>2</sub> decomposition reaction ( $\Delta H = -211.5 \text{ kJ mol}^{-1}$ ) (Fig. 1b), which are all thermodynamically more favored than the desired main synthesis reaction; (3) Cost of catalyst - Although noble metal catalysts, such as Pd, Pd–Au and Pd–Sn, are proven to be effective, the rareness and high price of these materials make the direct synthesis hard for large-scale applications.

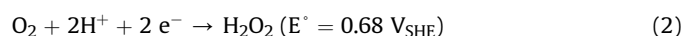
### 1.2.3. Photo-catalysis

Photo-catalysis through proton-coupled electron transfer is another alternative to generate H<sub>2</sub>O<sub>2</sub>. Briefly, in the heterogeneous photocatalytic process, an optical semiconductor is activated by irradiation of an appropriate light source to form photo-generated electron/hole (e<sup>-</sup>/h<sup>+</sup>, Fig. 1c) pairs, which under certain conditions induces the reduction of O<sub>2</sub> to produce H<sub>2</sub>O<sub>2</sub> [14]. Currently, it is accepted that H<sub>2</sub>O<sub>2</sub> can be produced via either a one-step two-electron direct reduction or a two-step one-electron indirect reduction route [15]. Photo-catalysis has emerged as a promising alternative since it only requires an optical semiconductor, water, oxygen, as well as sufficient and renewable light as the driving force. As a hot topic in recent research, multiple photo-catalysts have been investigated and employed, including TiO<sub>2</sub>, graphite carbon nitride (g-C<sub>3</sub>N<sub>4</sub>), metal-organic compounds and their modification materials. However, photocatalytic H<sub>2</sub>O<sub>2</sub> generation is still in its initial stage with several problems that need to be solved, such as poor selectivity toward 2 e<sup>-</sup> O<sub>2</sub> reduction, relatively low response to sunlight, and high recombination rate of photo-generated species [15]. Moreover, the H<sub>2</sub>O<sub>2</sub> can be further reduced with e<sup>-</sup> or decomposed by the irradiated UV light ( $\lambda < 400 \text{ nm}$ ), which causes the H<sub>2</sub>O<sub>2</sub> production rate to be lower than the above two methods [14,16].

### 1.2.4. Oxygen reduction reaction

The electrosynthesis of H<sub>2</sub>O<sub>2</sub> via two-electron oxygen reduction reaction (ORR) is attracting growing attention. The electrosynthesis of H<sub>2</sub>O<sub>2</sub> was first reported by Berl et al., in 1939 by applying activated carbon as a cathode to achieve a 90% current efficiency [17]. Based on the two-electron ORR pathway, the Huron-Dow process was developed in the 1980s (by Dow and Huron Technologies, Inc.) to produce dilute alkaline H<sub>2</sub>O<sub>2</sub> onsite (Eq. (1)) for pulp and paper bleaching (Fig. 1d) [9]. Although it was successfully commercialized in 1991, the inherent disadvantages includes corrosion of the electrodes from the highly alkaline environment, carbonate formation from CO<sub>2</sub> and the high Ohmic resistance in the system limiting its further development [12]. As a variant of the Huron-Dow process, the electro-Fenton (EF) process was first investigated and developed by Brilla's research group and Oturan's group

in the 1990s [18,19]. The EF technology is based on the continuous H<sub>2</sub>O<sub>2</sub> generation on a cathode (Eq. (2)) in an acidic electrolyte. ·OH radicals are generated via Fenton's reaction (Eq. (3)) with the addition of a sufficient amount of Fe<sup>2+</sup> ions. The homogeneous regeneration of Fe<sup>2+</sup> on the cathode (Eq. (4)) makes the persistent organic pollution (POPs) continuously degraded in EF. Until now, EF has become the most popular electrochemical technology to degrade a variety of POPs, including pesticides [19], dyestuffs [20], PPCPs [21,22], and industrial pollutants [18]. Moreover, novel electrochemical advanced oxidation processes (EAOPs) based on the cathodic generation of H<sub>2</sub>O<sub>2</sub> were developed for remediation of wastewater, such as photoelectro-Fenton [23], sono-electro-Fenton [24], peroxy-coagulation [25], and electro-peroxone processes [26].



Highly efficient cathode and the optimized system are two crucial prerequisites for the development of these EAOPs. Recently, substantial research has been devoted to the prediction and design of catalysts for electrochemical two-electron ORR and some of the progress has been previously presented in several reviews [12,27–35]. However, systematic and comprehensive reviews on carbonaceous two-electron ORR catalysts from the angle of mechanism and catalyst design to electrode fabrication have not been reported. As an emerging research field, it is necessary and indispensable to review and summarize the latest work on the development of these areas. Furthermore, from our point of view, the rapid development of electrode fabrication technology requires solid theoretical research in material science and catalytic science, as well as continuous optimization in engineering. In this review, we discuss the recently discovered mechanistic understanding of carbon materials catalysis and present important developments in carbon-based catalysts for two-electron ORR. Currently there are only a few comprehensive studies on two-electron ORR materials and the close correlation between two-electron ORR and four-electron ORR reactions. In the following sections we present some enlightening mechanisms and research results on four-electron ORR for the first time, including the predictive design by density functional theory (DFT) calculations and controllable doping/functionalization configurations as well as the construction of porous structures and defects to guide two-electron ORR design (Chapter 4). The remaining uncertainty on the real active sites for two-electron ORR are illustrated and discussed. Depending on the raw carbonaceous material and the operation mode, we also systematically summarize the preparation and modification methods for the formed carbon-based electrodes (Chapters 6, 7, and 8). Finally, we provide a detailed perspective on the challenges and opportunities in this rapidly developing field. We attempt to take full advantage of carbon-based materials in constructing highly efficient two-electron ORR catalysts and provide a thought for the amplification and application of electrocatalytic synthesis H<sub>2</sub>O<sub>2</sub> with high efficiency and low cost. Additionally, based on the knowledge amassed from the references and our former work experience, we hope to provide guidance and suggestions for future research by summarizing the inconsistent or divergent experimental and computational methods. We encourage future studies to use more unified experimental methods and expressions, while avoiding the oversights from previous studies.

## 2. Mechanism of the oxygen reduction reaction

The mechanism of electrochemical ORR is outlined in Fig. 2a. Generally, the ORR involves either a four-electron transfer pathway,

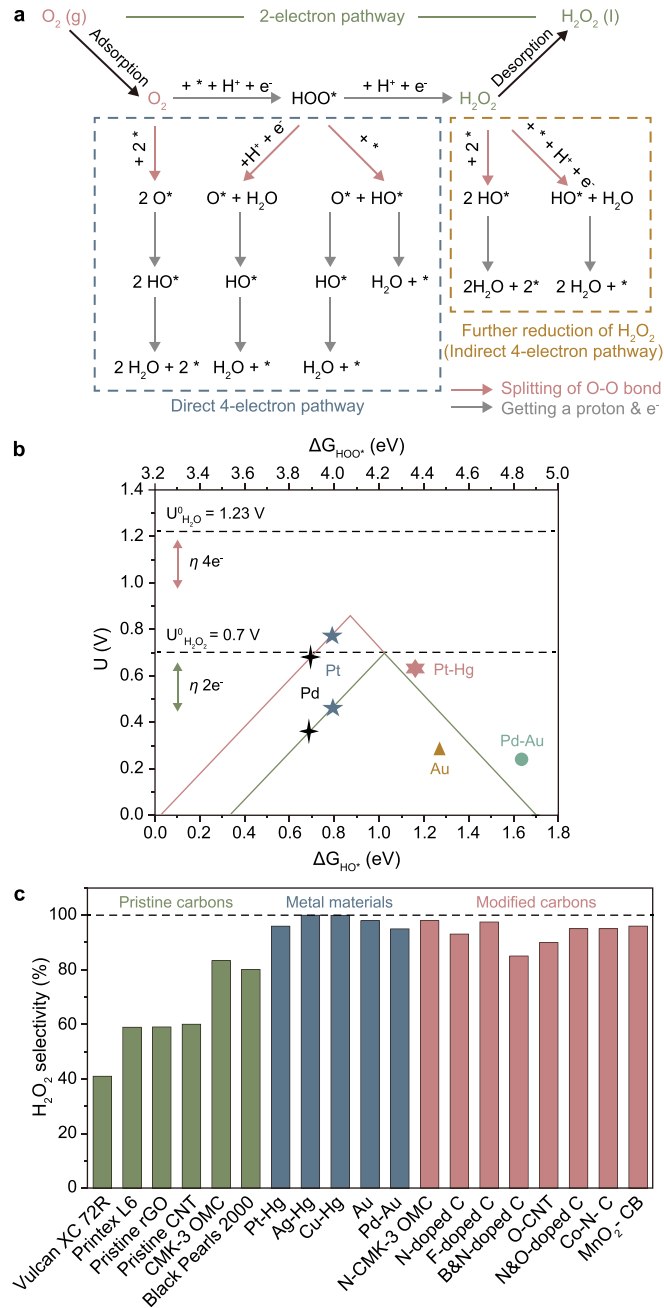
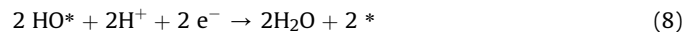


**Fig. 2.** a, Schematic of unified two and four-electron oxygen reduction reaction pathways. The dissociation of O–O bond (red arrows) engenders the undesired four-electron pathway. b, Theoretically calculated Sabatier volcano plots for the two-electron (green) and four-electron (red) oxygen reduction. The limiting potential (vertical axis) was plotted as a function of  $\Delta G_{HOO^*}$  (upper horizontal axis) and  $\Delta G_{HO^*}$  (lower axis). Two-electron pathway equilibrium potential ( $U^0_{O_2/H_2O} = 0.7 \text{ V}$ ) is shown in the dotted line, and the four-electron pathway equilibrium potential ( $U^0_{O_2/H_2O} = 1.23 \text{ V}$ ) is plotted as the dashed line [36]. c, Corresponding H<sub>2</sub>O<sub>2</sub> selectivity for previously developed electro-catalysts. Data adapted from literature [141] for Vulcan XC 72R; literature [151] for Printex L6 and pristine rGO; literature [120] for CNT; literature [87] for CMK-3 OMC, N-doped CMK-3 OMC and black pearl 2000; literature [36] for Pt-Hg; literature [72] for Ag–Hg and Cu–Hg; literature [44] for Au and Pd–Au; literature [85] for N-doped C; literature [102] for F-doped C; literature [107] for B&N-doped C; literature [118] for O-CNT; literature [121] for N&O-doped C; literature [137] for Co–N–C; literature [145] for MnO<sub>2</sub>-CB.

which reduces O<sub>2</sub> to H<sub>2</sub>O (Eq. (5)) and is attractive for fuel cells, or a two-electron pathway to produce H<sub>2</sub>O<sub>2</sub> (Eq. (2)), which is desirable for environmental remediation [36]. Overall, the direct four-electron ORR involves multiple steps and intermediates (HOO\*, HO\*, O\*), which can be divided into the dissociative and associative way, depending on the oxygen dissociation barrier on the catalyst surface (Eqs. (6)–(13)) [37,38].



Dissociative pathway: the O–O bond breaks into two O\*<sup>·</sup>, which could be reduced to H<sub>2</sub>O as the final product.



Associative pathway: the activated O<sub>2</sub> molecule firstly couples the proton & electron to produce HOO\*, and then the O–O bond of HOO\* is cleaved and reduced to H<sub>2</sub>O.

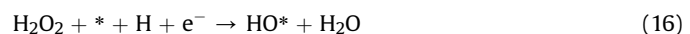


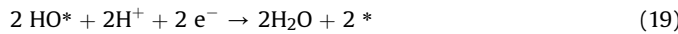
Where \* denotes an unoccupied active site, and HOO<sup>·</sup>, HO<sup>·</sup>, O<sup>·</sup> represent the single adsorbed intermediates on the catalyst surface [36].

Conversely, the two-electron pathway is comprised of two coupled electron & proton transfers together with one intermediate (HOO<sup>·</sup>) (Eqs. (14) and (15)) [39].



From the above reactions and the schematic diagram shown in Fig. 2a, it is observed that breaking the O–O bond (Eqs. (6) and (10)) is a necessary step in both dissociative and associative four-electron pathways. Therefore, preventing the O–O bond from dissociation is critical in the selective catalysis for H<sub>2</sub>O<sub>2</sub> synthesis [30]. Moreover, the obtained H<sub>2</sub>O<sub>2</sub> could be further reduced to H<sub>2</sub>O, making the process an indirect four-electron ORR to reduce the H<sub>2</sub>O<sub>2</sub> production (Eqs. (16)–(19)). Consequently, shortening the H<sub>2</sub>O<sub>2</sub> residence time on the catalyst surface is also critical to maintaining the stability of H<sub>2</sub>O<sub>2</sub> during electro-synthesis. In summary, the ideal electrocatalyst with high activity and high selectivity toward two-electron ORR should have the property of minimizing the kinetic barriers for Eqs. 14 and 15 and maximizing the barrier for H<sub>2</sub>O<sub>2</sub> reduction and HOO<sup>·</sup> dissociation to HO<sup>·</sup> and O<sup>·</sup> [36].





The performance of the electrocatalyst depends on the binding energy of the reaction intermediates to the catalyst surface [36]. However, because of the existence of scaling relationships Eq. (20) between these intermediates, the activity is governed by a single parameter  $\Delta G_{\text{HO}^*}$  [40,41]. Benefiting from the development of DFT calculations on numerous close-packed metal surfaces, a volcano framework has established that the theoretical overpotential relates to the free energy of  $\text{HO}^*$  for the ORR activity (Fig. 2b) [42,43]. In brief, for the materials that bind  $\text{HO}^*$  too weakly (i.e., to the right side of the peak), the ORR is limited by the activation of  $\text{O}_2$ . The weak interaction with  $\text{O}^*$  and  $\text{HO}^*$  increases the selectivity toward two-electron ORR, but simultaneously lowers the ORR activity. For the materials that bind  $\text{HO}^*$  too strongly (i.e., to the left side of the peak), the limiting step for the  $\text{H}_2\text{O}_2$  and  $\text{H}_2\text{O}$  production is associated with removing  $\text{HOO}^*$  and  $\text{HO}^*$ , respectively. Considering the two-electron pathway is determined by only one intermediate, it is feasible to find an electrocatalyst with zero theoretical overpotential that has an optimal  $\Delta G_{\text{HOO}^*}$ , binding  $\text{HOO}^*$  neither too strongly nor weakly [43].

$$\Delta G_{\text{HOO}^*} = \Delta G_{\text{HO}^*} + 3.2 \pm 0.2 \text{ eV}$$
 (20)

The electrocatalysts for two-electron ORR covers a wide range from noble metals (Pb, Au, etc.) and metal alloys to carbonaceous materials. The metal alloys, such as Pd–Au [44,45] and Pt–Hg [36], were verified to have high selectivity toward  $\text{H}_2\text{O}_2$  (70.8–92.5% under 0.1–0.3 V vs. RHE at pH 1). However, the wide application of these noble-metal catalysts is impacted by their scarcity and high cost [46]. Accordingly, metal-free and non-noble-metal catalysts are developed as sustainable alternatives. Carbon materials are a promising alternative for  $\text{H}_2\text{O}_2$  electrosynthesis because of their high abundance, conductivity, activity, and lower price. Most importantly, with a variety of allotropes, the carbon materials have multiple morphologies and highly tunable electronic structures. This unique feature makes them an ideal platform for designing electrocatalysts at the atomic level [47].

### 3. Evaluation parameters of two-electron ORR electrocatalyst

The characterization of electrocatalyst performance via the rotating ring disk electrode (RRDE) technique in a three-electrode system is necessary for evaluating ORR activity and  $\text{H}_2\text{O}_2$

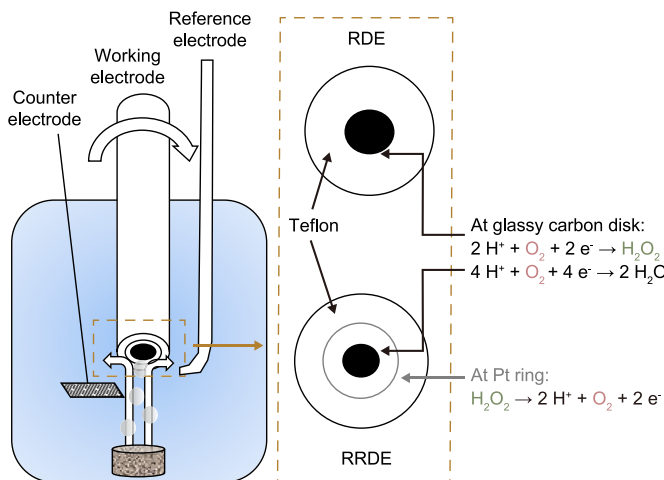


Fig. 3. Schematic of RRDE & RDE set-up and basic operating principles.

selectivity in the material design. RRDE is a convective electrode system containing a disk electrode, a coaxial Pt ring electrode together with a rotating shaft (Fig. 3) [48]. In the RRDE, the ORR takes place on the disk electrode to generate both  $\text{H}_2\text{O}_2$  and  $\text{H}_2\text{O}$ . Thereafter,  $\text{H}_2\text{O}_2$  is radially transferred to the coaxial Pt ring electrode by the forced convection resulting from the rotation of the electrode. Subsequently,  $\text{H}_2\text{O}_2$  is oxidized back to  $\text{O}_2$  (Eq. (21)) at the ring electrode. The overall ORR activity and  $\text{H}_2\text{O}_2$  selectivity could be quantified by analyzing the corresponding reduction disk current ( $i_D$ ) and oxidation ring currents ( $i_R$ ), respectively [49]. The selectivity of  $\text{H}_2\text{O}_2$  is quantified by the Faradaic efficiency ( $\lambda_{\text{Faradaic}}$ ) and the average transferred electrons number ( $n$ ).



$$\lambda_{\text{Faradaic}} = \frac{i_R}{i_D} \times 100\%$$
 (22)

$$n = \frac{4|i_D|}{|i_D| + i_R}$$
 (23)

where  $N$  represents the collection efficiency of the RRDE, which means the fraction of product from the disk to the ring, based on the geometries of the ring and disk electrodes [30].

Rotating disk electrode (RDE) is another tool for assessing the catalyst ORR activity. Compared with RRDE, the coaxial ring electrode is removed in the RDE system (Fig. 3). The hydrodynamic and electrochemical properties of RDE are related to the Koutecky-Levich (K-L) equation [50].

$$\frac{1}{j} = \frac{1}{j_K} + \frac{1}{j_L} = \frac{1}{nFkC_0} + \frac{1}{0.62nFC_0D_0^{3/2}\nu^{-1/6}w^2} \quad (24)$$

where  $j_K$  and  $j_L$  are the kinetic-limiting current density and diffusion-limiting current density ( $\text{mA cm}^{-2}$ ),  $n$  stands for the electron-transfer number,  $F$  is the Faraday constant ( $\text{C mol}^{-1}$ ),  $C_0$  and  $D_0$  are the bulk concentration ( $\text{mol cm}^{-3}$ ) and  $\text{O}_2$  diffusion coefficient ( $\text{cm}^2 \text{s}^{-1}$ ) in the electrolyte,  $\nu$  is the kinematic viscosity of the electrolyte ( $\text{cm}^2 \text{s}^{-1}$ ),  $\omega$  represents the angular velocity ( $\text{rad s}^{-1}$ ), and  $k$  is the electron-transfer rate constant.  $n$  and  $k$  can be obtained from the slope and intercept of K-L equation, respectively.

Typically the onset potential or overpotential ( $\eta$ ) in (R)RDE tests are used to compare the activities among different electrocatalysts. And the selectivity of newly designed electrocatalysts toward  $\text{H}_2\text{O}_2$  is mainly quantified in terms of  $n$  and  $\lambda$ . In Tables 1 and 2, the performance of newly developed electrocatalysts on (R)RDE are systematically summarized.

### 4. Design of high-performance carbonaceous electrocatalysts

#### 4.1. Pristine carbon materials

Before discussing the carbon catalysts, it is vital to discuss the different types of obtained carbon materials. There are three allotropes as dictated by the carbon precursor [51]: graphite ( $sp^2$  bonding), diamond ( $sp^3$ ), and amorphous carbon (disordered mixture of  $sp^2$  and  $sp^3$ ). Due to the different combinations of carbon atom hybridization, carbon allotropes with different structures and properties are obtained. Until now, most of the two-electron ORR catalysts are graphite carbon and amorphous carbon.

Graphite is formed by multilayered two-dimensional (2D) sheets of  $sp^2$  hybridized carbon atoms with hexagonal lattice in the basal plane. The edges of its planes have terminations with carbon atoms arranged with zigzag or armchair configurations, and a van

**Table 1**

RRDE settings and results of the new developed carbon-based materials summarized in Chapter 4.

Material Type	RRDE test settings				RRDE test results						Reference
	Electrolyte Conditions ( $O_2$ -saturated)	Rotating speed (rpm)	Scan rate ( $mV\ s^{-1}$ )	Ring Potential	Onset Potentials		Selectivity (%)	Electron transfer number	Potential window		
					Current density to define onset potential	Potential					
N-doped porous carbon	0.1 M KOH	900	5	unknown	-0.03 mA cm <sup>-2</sup>	0.72 V vs. RHE	93	2.1	<0.6V vs. RHE	[87]	
N-doped MC	0.5 M H <sub>2</sub> SO <sub>4</sub>	1500	5	1.2 V vs. RHE	unknown	unknown	95	2.1	0.3 V vs. RHE	[89]	
N-doped CMK-3 by EMIM-dca	0.5 M H <sub>2</sub> SO <sub>4</sub>	1600	5	1.2 V vs. RHE	-0.03 mA cm <sup>-2</sup>	0.55 V vs. RHE	98	2.1	0.3 V vs. RHE	[85]	
N-doped CMK-3 by PEI	0.5 M H <sub>2</sub> SO <sub>4</sub>	1600	5	1.2 V vs. RHE	-0.01 mA cm <sup>-2</sup>	0.49 V vs. RHE	98.5	2.01	0.35 V vs. RHE	[86]	
N-doped macroporous carbon	0.5 M H <sub>2</sub> SO <sub>4</sub>	1600	10	1.1 V vs. RHE	unknown	unknown	~97	2.06	0.6 V vs. RHE	[91]	
F-doped HPC	0.05 M H <sub>2</sub> SO <sub>4</sub>	800	10	1.3 V vs. RHE	-0.2 mA cm <sup>-2</sup>	0.43 V vs. RHE	97.5	2.05	0.2 V vs. RHE	[100]	
N, S-doped MC	0.5 M H <sub>2</sub> SO <sub>4</sub>	1600	5	1.25 V vs. SHE	unknown	0.32 V vs. SHE	75	2.5	0.06V vs. SHE	[102]	
B, N-doped Carbon	0.1 M KOH	1600	10	1.2 V vs. RHE	-0.5 mA cm <sup>-2</sup>	0.8 V vs. RHE	85	2.3	0.5 V vs RHE	[107]	
N, O-doped OMC	0.5 M H <sub>2</sub> SO <sub>4</sub>	2500	10	1.2 V vs. RHE	-0.1 mA cm <sup>-2</sup>	0.55 V vs. RHE	~95	2.1	0.4 V vs. RHE	[119]	
O-CNT	0.1 M KOH	1600	10	1.2 V vs. RHE	-0.05 mA	unknown	~90	2.2	0.4–0.65 V vs. RHE	[116]	
oxidized CB	0.1 M Na <sub>2</sub> SO <sub>4</sub>	unknown	5	-0.4 V vs. Ag/AgCl	unknown	-0.14 V vs. Ag/AgCl	52.6–56.1	~2.9	-0.35 to -0.6 V vs. Ag/AgCl	[117]	
Co-CB composite	0.1 M HClO <sub>4</sub>	900	5	1.2 V vs. RHE	unknown	unknown	80–90	unknown	0.1–0.4 V vs. RHE	[120]	
CeO <sub>2</sub> -CB composite	1 M NaOH	1600	5	0.2 V vs. Hg/HgO	unknown	unknown	44	3.1	unknown	[139]	
SnNi-CB composite	1 M NaOH	1600	5	0.2 V vs. Hg/HgO	unknown	unknown	88	2.2	unknown	[141]	
V <sub>2</sub> O <sub>5</sub> -CB composite	1 M NaOH	1600	5	0.2 V vs. Hg/HgO	unknown	unknown	68	2.6	unknown	[140]	
WO <sub>2.72</sub> -CB composite	1 M NaOH	1600	5	0.3 V vs. Hg/HgO	unknown	unknown	87	2.3	unknown	[144]	
MnO <sub>2</sub> -CB composite	1 M NaOH	1600	5	unknown	unknown	unknown	96	2.1	unknown	[143]	
CeO <sub>2</sub> -CB composite	1 M NaOH	1600	5	0.2 V vs. Hg/HgO	unknown	unknown	88	2.2	-0.4V vs. Hg/HgO	[147]	
Nb <sub>2</sub> O <sub>5</sub> -rGO composite	0.1 M K <sub>2</sub> SO <sub>4</sub> , pH = 2	900	5	1.0 V vs. Ag/AgCl	unknown	unknown	85.3	2.28	-0.2 to -0.4V vs. Ag/AgCl	[149]	
Ta <sub>2</sub> O <sub>5</sub> -CB composite	0.1 M K <sub>2</sub> SO <sub>4</sub> , pH = 2	900	5	1.0 V vs. Ag/AgCl	unknown	unknown	83.2	2.3	-0.3 to -0.5 V vs. Ag/AgCl	[146]	
Pd-CB composite	0.1 M K <sub>2</sub> SO <sub>4</sub> , pH = 2.5	900	5	1.0 V vs. Ag/AgCl	unknown	0.35 V vs. Ag/AgCl	—	2.9	-0.15 to 0.51 V vs. Ag/AgCl	[148]	
Fe <sub>3</sub> O <sub>4</sub> -rGO composite	1 M KOH	1600	10	1.3V vs. SCE	unknown	unknown	62	2.8	-0.6 V vs. SCE	[150]	
Fe <sub>3</sub> O <sub>4</sub> -CB composite	1 M KOH	1600	10	1.3 V vs. SCE	unknown	unknown	68	2.7	-0.6 V vs. SCE	[150]	
Co-N <sub>x</sub> & OFGs-C	0.1 M KOH	1600	10	unknown	unknown	0.84 V vs. RHE	85.6	2.3	0.78V vs. RHE	[135]	
Co-TETA-C catalysts	0.1 M HClO <sub>4</sub>	1600	20	1.2 V vs. RHE	unknown	unknown	~95	2.1	0 V vs. RHE	[131]	
CoTMPP-CB	0.05 M H <sub>2</sub> SO <sub>4</sub>	200	2	1.1 V vs. SCE	unknown	unknown	80	2.4	0.3–0.4 V vs. SCE	[125]	
defective OMC	0.1 M KOH	1600	10	1.2 V vs. RHE	unknown	0.7 V vs. RHE	80	2.4	0.5 V vs. RHE	[158]	
N-Doped Graphene	0.1 M KOH	1600	10	1.2 V vs. RHE	-0.01 mA cm <sup>-2</sup>	unknown	82	2.4	0.1–0.5 V vs. RHE	[160]	
O-CB	0.1 M KOH	1600	10	unknown	dj <sub>D</sub> /dE > 0	0.8 V vs. RHE	~60	~2.8	0.26–0.36 V vs. RHE	[118]	
Mn–O/N@NCs	0.1 M HClO <sub>4</sub>	900	unknown	1.2 V vs. RHE	unknown	0.47 V vs. RHE	74	2.5	0.2 V vs. RHE	[134]	
B-CB	0.1 M KOH	1600	5	1.2 V vs. RHE	-0.1 mA cm <sup>-2</sup>	0.773 V vs. RHE	85	2.3	0.4–0.7 V vs. RHE	[101]	
OGFs modified activated coke	0.1 M KOH	1600	10	1.2 V vs. RHE	-0.15 mA cm <sup>-2</sup>	0.83 V vs. RHE	~80	2.4	0.2–0.8 V vs. RHE	[115]	
N-rGO & CNT	0.05 M Na <sub>2</sub> SO <sub>4</sub> , pH = 3	1600	10	1.2 V vs. SCE	unknown	-0.072 V vs. SCE	unknown	unknown	unknown	[259]	

**Table 2**

RDE settings and results of the new developed carbon-based materials summarized in Chapter 4.

Material Type	RDE test settings			RDE test results				Ref	
	Electrolyte Conditions (O <sub>2</sub> -saturated)	Rotating speed (rpm)	Scan rate (mV s <sup>-1</sup> )	Onset Potentials		Selectivity (%)	Electron transfer number		
				Current density to define onset potential	Potential				
N-doped OMC	0.1 M KOH	2500	10	unknown	-0.1 V vs. Ag/AgCl	~85	2.3	-0.35 V vs. Ag/AgCl [90]	
P-doped MWCNT	0.1 M Na <sub>2</sub> SO <sub>4</sub>	1600	5	unknown	unknown	47	3.06	-0.4 vs. SCE [256]	
N,S-doped MC	0.1 M KOH	1600	10	0.02 mA cm <sup>-2</sup>	0.8 V vs. RHE	~100	2	0.15–0.5 V vs. RHE [105]	
HPC derived from MOF-5	0.05 M H <sub>2</sub> SO <sub>4</sub>	unknown	10	unknown	unknown	~90	2.1–2.38	-0.1 to -0.5 V vs. RHE [158]	

MC: mesoporous carbon.

der Waals interaction along the transverse direction between the layers that is relatively weak. Apart from naturally existing graphite, the discovery of graphene and carbon nanotubes (CNTs) expanded the categories of *sp*<sup>2</sup> carbon materials. Graphene (a single layer form of graphite) is a 2D sheet honeycomb structure composed of *sp*<sup>2</sup> carbon atoms. Due to the remarkable electrical, thermal, physical, optical, and mechanical properties together with high specific surface area, it has received increasing attention [28,52]. Graphene can be prepared by a variety of processes, including mechanical cleavage [53], chemical vapor deposition growth [54], epitaxial growth [55], electrochemical exfoliation of graphite [56], and thermal/chemical/electrochemical reduction of graphene oxide (GO) [57]. Among those, the mechanical cleavage method results in high-quality graphene sheets but low yield, which cannot meet the large demand for graphene. The GO reduction method is considered to be one of the most promising routes for large-scale graphene production, which restores the essential properties. However, the production of graphene with minimum defects remains challenging. CNTs are tubular cylinders of carbon atoms that can be conceptually viewed as one or up to dozen graphene sheet(s) that are rolled up into a single-wall carbon nanotube (SWCNT) or a multiwall carbon nanotube (MWCNT) [51]. CNTs have been at the forefront of materials research in the last decade due to their high electrical conductivity (~5000 S cm<sup>-1</sup>) [58], high surface area (~2630 m<sup>2</sup> g<sup>-1</sup>) [59], high charge mobility (~100,000 cm<sup>2</sup> V<sup>-1</sup> s<sup>-1</sup>) [60], as well as chemical stability, and significant mechanical strength. Currently, SWCNTs and MWCNTs are mainly produced by three techniques: arc-discharge [61], laser-ablation [62], and catalytic growth [63]. Among these methods, catalytic growth of nanotubes by the chemical vapor deposition (CVD) is the dominant mode of high-volume CNT production. In 2013, bulk purified MWCNTs were sold for less than 100 \$ kg<sup>-1</sup> [64]. The decrease in CNTs price increases their potential for application in various technological areas such as the chemical, medical, aerospace, energy, and automotive industries.

Carbon black (CB) is an amorphous particle of nearly pure elemental carbon, consisting of grape-like aggregates of spherical primary particles, with the aggregates clustered into larger-sized agglomerates [65]. CB has relatively low quantities of extractable organic compounds and total inorganics (usually <1%) [66]. As a manufactured commercial product for over a century, it has plentiful applications as well as a variety of different trade names and physicochemical properties. A variety of CB grades with different properties (surface area, structure, aggregate size, abrasion resistance, etc.) are manufactured by controlling the conditions of the oil furnace production process. The most widely used CB material is Vulcan XC-72(R) (produced by Cabot Corporation, US) which is used in 80% of electrocatalysts [67], due to the large surface area (~250 m<sup>2</sup> g<sup>-1</sup>), high mesopore and macropore percentage (54%),

and good electric conductivity (4.0 S cm<sup>-1</sup> at the packing fraction of 0.3 and 7.4 S cm<sup>-1</sup> at 0.4) [68,69]. In addition to Vulcan XC-72(R), there are some other commercial CB materials such as Printex L6, Black Pearls 2000, Acetylene Black, and Macsorb [70].

Ordered mesoporous carbon (OMC) is a type of carbon material with regular arrays of uniform mesopores. The OMCs with different compositions vary from pure organic/inorganic frameworks to organic-inorganic hybrid frameworks have been widely investigated and reported in the past two decades. Normally, OMCs can be prepared by two different methods, the hard templating process (nano-casting strategy) by using mesoporous silicas and a soft templating process (direct synthesis) via self-assembly of block copolymers/surfactants and carbon precursors [71]. Except for high surface areas, OMCs also have outstanding special properties, including tunable pore sizes, alternative pore shapes, periodically arranged monodispersed mesopore space, and uniform nano-sized frameworks [72].

Because of the above outstanding physical and chemical properties, tremendous investigations have been conducted to reveal the ORR catalytic characteristics of graphene, CNTs, CB, and OMCs. However, the electroactivity of pristine carbon catalysts still lags behind that of their metal counterparts because pristine carbon materials are inert to the adsorption and activation of O<sub>2</sub> and ORR intermediates (Fig. 2c) [36,44,73]. They always show high overpotentials and thus unpromising catalytic property toward ORR [74]. Therefore, the catalytic properties of carbon materials need to be improved by doping, functionalization, and structural regulation.

## 4.2. Heteroatom doping

Heteroatom doping refers to replacing part of carbon atoms in the carbon skeleton by other heteroatoms, including N, O, B, P, S, halogens, etc. (Fig. 4a) Because of the differences in atomic size, electronegativity, and binding states, heteroatom doping can regulate the spin and charge distribution, tune the absorption and activation of the ORR intermediates, and further change the catalytic performance of carbon [74,75]. For instance, B and P dopants tend to give electrons to carbon due to their lower electronegativity (B: 2.04; P: 2.19) compared with carbon (2.55), which creates a partial positive charge on the dopant atoms [76]. In contrast, nitrogen with higher electronegativity (N: 3.04) tends to rob electrons from carbon to generate a partial positive charge on the carbon atoms. Typically, the formation of partial positive/negative charges can both promote the interaction between the catalyst and O<sub>2</sub>, and the adsorption of O<sub>2</sub> on the carbon materials. Though S doping does not disrupt the charge uniformity of carbon materials because of its similar electronegativity (2.58), larger size, and greater polarizability of the S atom enhance the spin density and

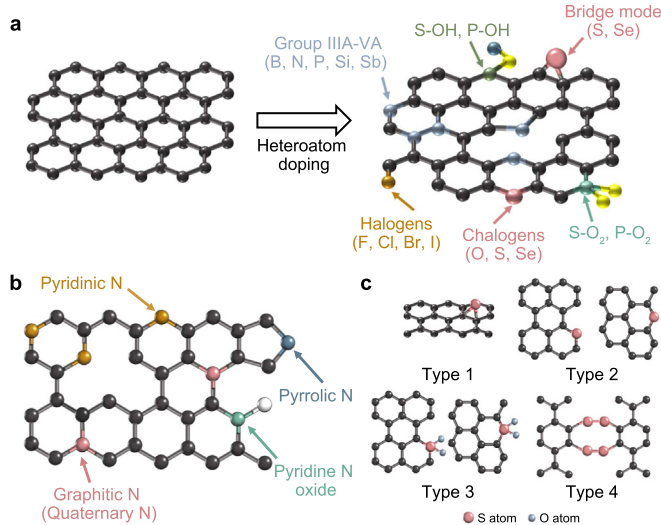


**Fig. 4.** **a**, Schematic illustration of the X-doped graphene lattice, which shows the possible positions of different dopants. **b**, Typical nitrogen species in N-doped carbon skeleton. **c**, Schematic of S-doped graphene clusters, including S atoms adsorbed on the graphene cluster surface (Type 1) replacing S atoms at zigzag or armchair edges (Type 2); SO<sub>2</sub> replaced at zigzag or armchair edges (Type 3); and S ring connecting two pieces of graphene (Type 4) [98].

charge delocalization on the neighboring carbon atoms to promote the ORR [77,78].

As a convenient method to tune the electrochemical catalytic properties of carbon materials, doping has been utilized widely in developing ORR catalyst materials. Here, carbon materials with multiple heteroatoms doping for H<sub>2</sub>O<sub>2</sub> production are reviewed.

#### 4.2.1. Single doping by N

N-doping is the most extensively and promising form to modify sp<sup>2</sup> carbon for ORR for two reasons: one, N has a similar atomic radius as C, allowing it to easily replace C atoms without lattice mismatch; and two, the higher electron affinity of N makes the N dopant easy to change the atomic structures and electron arrangements of the carbon skeleton [46,74,78]. First synthesized by Gong et al. [75], N-doped carbon materials for four-electron ORR have attracted much attention. Typically, there are two strategies for fabricating N-doped carbon catalysts. The first one is post-doping of porous carbons in the presence of nitrogen-containing precursors, which can effectually control the structures of the catalyst. However, the N-doping efficiency of post-doping is low and diverse. The other method is direct (*in-situ*) doping during the synthesis of catalysts to enhance the N-doping content and vary the N-doping structure. Nevertheless, the pore size and porosity of the catalyst are difficult to be precisely controlled in direct doping.

Resulting from different synthetic precursors, catalysts, conditions, and procedures, there are various forms of N dopant that exist in the carbon skeleton, such as pyridinic N, pyrrolic N, graphitic N (or quaternary N), and pyridine-N-oxide (Fig. 4b). However, not all N dopant-related dopants on the carbon materials constitute highly catalytic active species. There is debate on the real active sites in N-doped carbon for ORR. In general, planar pyridinic-N can enhance the electron-donating capability and weaken the O–O bond due to its lone electron pair. As a result, pyridinic-N is thought to be the active site for four-electron ORR [79]. Guo et al. [80] reported that carbon atoms adjacent to pyridinic-N are the real active sites for ORR in acidic media. Others have suggested that pyrrolic-N plays a key role in reducing O<sub>2</sub> to H<sub>2</sub>O<sub>2</sub>, and pyridinic-N is the site for reducing H<sub>2</sub>O<sub>2</sub> to H<sub>2</sub>O [81,82]. Conflictingly, Geng,

et al. [83] believed that graphitic-N instead of pyridinic-N might be responsible for the two-electron ORR. Kabir et al. [84] claimed graphitic-N contributes significantly to peroxide generation in 0.5 M H<sub>2</sub>SO<sub>4</sub>. The co-generation and co-existence of different types of N-doping species in the carbon materials are inevitable, making it difficult to distinguish their contributions. Moreover, the inter-transition of the different doping types induced by temperature makes the situation even more complex.

In the recent 7–8 years, the N-doped carbon two-electron ORR catalysts have been systematically investigated to obtain different results on two-electron ORR active pores. N-doped OMC with a mean pore diameter of 13.2 nm was obtained from the ionic liquid N-butyl-3-methylpyridinium dicyanamide (BMP-dca) at 800 °C by hard-templating strategy using silica nanoparticles [85]. H<sub>2</sub>O<sub>2</sub> production rate reached 0.17 g g<sub>cat</sub><sup>-1</sup> h<sup>-1</sup> with a current efficiency of 65.2% at 0.1 V (vs. RHE). The RDE verified that the resultant material was highly active for the selective H<sub>2</sub>O<sub>2</sub> generation. However, a comparable material synthesized at 1000 °C was favorable to the four-electron ORR [86]. The authors assumed the lower degree of delocalization, higher N content, and exposure of pyrrolic-N sites may favor the two-electron process.

Sun et al. [87] fabricated a series of N-doped OMC materials by pyrolyzing the mixture of 1-Ethyl-3-methylimidazolium dicyanamide (EMIM-dca) and CMK-3 at different temperatures. Compared with six potentially suitable two-electron ORR carbon materials (Ketjen black EC 300J, Ketjen black EC 600JD, Black pearls 2000, Vulcan XC 72R, Graphene nano-plates, and CMK-3), the structural, compositional, and other physical properties were correlated with their catalytic performance. For six pristine carbon materials, large BET surface areas, positive zeta potentials, and high defect sites were all beneficial for H<sub>2</sub>O<sub>2</sub> generation. Dissimilarly, the H<sub>2</sub>O<sub>2</sub> selectivity of N-doped carbon catalyst is governed more by the N doping effect. The selectivity of the optimal N-doped material reached 95–98% in the potential range of 0.1–0.3 V (vs. RHE). In order to get a better understanding of the potentially related mechanistic roles of the different N species during the two-electron ORR, a novel N-doped OMC was prepared by annealing the mixture of CMK-3 and polyethylenimine (PEI) in the N<sub>2</sub> atmosphere; achieving the highest H<sub>2</sub>O<sub>2</sub> selectivity of 95–98.5% with the potential range of 0.1–0.4 V [88]. Analyzing chemical state trajectories of N species in the catalysts suggested pyridinic-N played a key role as an active site in acidic solution, while graphitic-N groups seemed to be active catalytic moieties in neutral and alkaline conditions.

Other N-doped porous carbons were prepared from paraformaldehyde cross-linked collagen by sintering at various temperatures (400–800 °C) [89]. Higher carbonization temperature brought more porous and sheet-like structures into the materials, and led to the formation of graphitic-N structure, the removal of oxygen-containing functional groups, and the decrease of N content, thus enhancing graphitic crystallinity. According to the electrochemical tests, N-doped carbon prepared at 400 °C showed excellent two-electron ORR with a selectivity of 93% over a wide potential range from 0.17 to 0.6 V (vs. RHE) due to the combination of pyridinic-N, pyrrolic-N, and the surface oxygen-containing functional groups.

Since ORR generally proceeds on the surface of the catalysts, the unexposed active sites hidden in the catalyst body contribute little to the catalytic activity [74]. Therefore, the appropriate doping location and catalyst micro-configuration are more crucial than the gross doping content.

To obtain a special carbon material with N-doping mainly at the surface, to provide active sites and high graphitic carbonaceous core to provide high electrical conductivity, N-doped graphitic carbon materials were fabricated by sequential pyrolysis of aniline and dihydroxynaphthalene (DHN) inside the SBA-15 hard silica template (Fig. 5a) [90]. To cover the template surface with

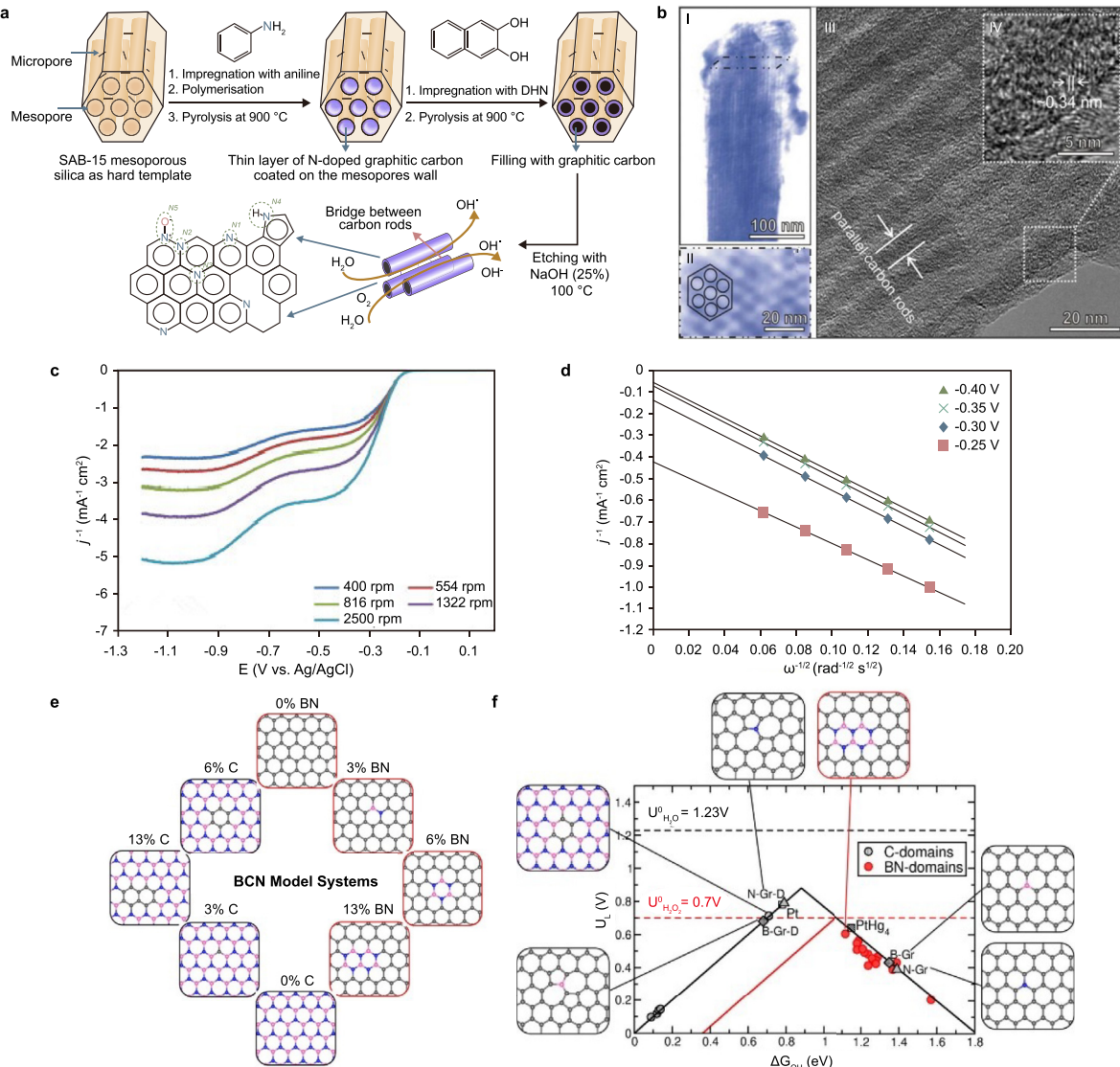


**Fig. 5.** **a**, Schematic of the N-doped OMC formation using SBA-15 as hard template. The N atoms in the N-doped OMC are illustrated: pyridinic-N ( $N_1$ ), graphitic-N ( $N_2$ ,  $N_3$ ), pyrrolic-N ( $N_4$ ), and oxidized pyridinic-N ( $N_5$ ). **b**, Reconstructions of the N-doped OMC sample from different orientations (I and II). HR-TEM images of N-doped OMC (III and IV), with the illustration of the parallel carbon rods position and the graphitic layers (0.34 nm spacing). **c**, LSV curves of the N-doped OMC conducted in 0.1 M KOH  $O_2$ -saturated solution at the scan rate of 10 mV s<sup>-1</sup> under different rotation speeds. **d**, the corresponding K-L plots ( $j^{-1}$  vs.  $\omega^{-1/2}$ ) at different potentials for N-doped OMC Adapted from the literature [90], with permission from Elsevier. **e**, Schematic of the BCN materials models calculated in this research. C atoms: gray; N atoms: blue; B atoms: pink. %X is defined as the amounts of C atoms replaced in h-BN substrate over the total substrate atoms amounts. Likely, for BN domains configurations %X composition is determined as the number of BN pairs replaced in graphene substrate over the total substrate atoms number. **f**, Theoretical volcano plots for two-electron (red) and four-electron (black) ORR respectively (II). The volcano plots are based on the RHE. Triangle marks or diamond marks represent the ORR activity of the N or B doped in the raw (N-Gr or B-Gr) and defect (N-Gr-D or B-Gr-D) graphene, respectively. The performance of N-Gr-D is from literature [110], while the catalytic performances of Pt (111) metal and PtHg<sub>4</sub> alloy are from literature [36,111], respectively. Adapted from the literature [109], with permission from American Chemical Society.

monolayered aniline, the amount of aniline employed was determined based on the precise calculation of the molecular cross-sectional area of precursor and total pore volume of the template. The resultant materials displayed an ordered, hexagonal array of carbon rods, with a narrow pore size distribution centred at 4.3 nm, and specific surface area of 877 m<sup>2</sup> g<sup>-1</sup> (Fig. 5b). The novel N-doped OMC exhibited outstanding performance with a transfer number of 2.1, and a  $H_2O_2$  selectivity of 95% (Fig. 5c). Which attributed to the high surface area, regular mesopores structure, a graphitic character, high content graphitic-N and pyridinic-N configurations.

Except for the N species, other influence factors were also investigated. Park et al. [91] studied the effect of the mesopores to discover that N-doped carbon materials with 3.4–4 nm well-

ordered mesopores had high activity and selectivity (>90%) for  $H_2O_2$  synthesis. In comparison, micropore-dominant N-doped activated carbon showed a higher onset potential than N-doped OMC, but a lower selectivity (56–60%). The excellent mass transfer of mesoporous structure enhanced the release of  $H_2O_2$  within a relatively short contact time, which resulted in high selectivity toward  $H_2O_2$  synthesis. Hasché et al. [92] proposed that the electrochemical formation mechanisms for peroxide are dependent on the pH and the species of electrolyte, as well as the respective change of the peroxide species from  $H_2O_2$  to hydroperoxide. In order to obtain a kinetic understanding of N-doped carbon catalysts in acidic media, a porous N-doped carbon with a surface area of 992 m<sup>2</sup> g<sup>-1</sup> was obtained by carbonization of polyimide

nanoparticles through a two-step pyrolysis [93]. RRDE revealed that lower catalyst loading on the disk suppresses the further reduction of  $\text{H}_2\text{O}_2$  in the catalyst matrix layer. When the catalyst loading density decreased to  $30 \mu\text{g cm}^{-2}$ , the  $\text{H}_2\text{O}_2$  selectivity was much higher than 80%. This study provided quantitative insight into the ORR mechanism over an N-doped carbon catalyst.

#### 4.2.2. Single doping by other heteroatoms

Although N-doped carbon materials have been investigated extensively, carbon materials doped with B, P, S, and halogens have also been explored recently for their potential applications for electrocatalysis of ORR. However, almost all of the B/P/S doped carbon materials demonstrated an affinity for four-electron ORR instead of two-electron ORR for  $\text{H}_2\text{O}_2$  generation [94–97].

Zhang et al. [98] studied the formation energy, electronic structures, transition states, and energy barriers of S-doped graphene clusters by DFT calculation to predict ORR activity of four types of S-doped graphene clusters (Fig. 4c); including S atoms adsorbed on the graphene cluster surface (Type 1), S atom replacement at the graphene cluster armchair edge or zigzag (Type 2),  $\text{SO}_2$  substitution at the graphene edge (zigzag and armchair). Type 3), and two graphene clusters connected by an S ring (Type 4). Carbon atoms with high spin density or positive charge density are the active catalytic sites, which are often located at the zigzag edges or close to the  $\text{SO}_2$  doping structure. Two-electron ORR proceeds on the substitutional S atom with a high charge density, while four-electron ORR occurs simultaneously on the carbon atoms with a high positive spin or charge density.

Considering the high electronegativity of Fluorine (3.98), the carbon electronic structure can be adjusted significantly by F atom doping. In addition, F-doping regulated the electron transfer properties by inducing polarization and changing the Fermi level [99,100]. Recently, a F-doped hierarchically porous carbon catalyst was developed from an aluminum-based metal-organic framework (MOF, MIL-53) precursor [101,102]. The selectivity of the ORR pathway strongly depended on the F doping species configurations. The covalent  $\text{CF}_2$  and  $\text{CF}_3$  facilitate the two-electron pathway because of the strong adsorption of  $\text{O}_2$  and the weak binding energy of the  $\text{HO}^*$  intermediate. Hence, the fabricated F-doped catalysts exhibited a high  $\text{H}_2\text{O}_2$  yield of  $113\text{--}793 \text{ mmol h}^{-1} \text{ g}_{\text{cat}}^{-1}$ , and selectivity reached 97.5–83% in the potential range of  $-0.1 \text{ V}$  to  $-0.6 \text{ vs. RHE}$  (pH 1).

In 2021, Xia et al. [103] systematically studied the effects of different dopants (B, N, P, S) in carbon material on its performance in  $2\text{e}^-$  ORR performance. Among all these dopants, B-doped carbon shows the highest activity and selectivity, with an onset potential of  $0.773 \text{ V}$  (vs. RHE) while maintaining over 85% selectivity across a broad potential window in  $0.1 \text{ M KOH}$ . BET, XPS, XAS, and Raman results excluded the possible morphological, structural, and electronic side effects on  $2\text{e}^-$  ORR. DFT calculations revealed the B-doped at single vacancy has nearly-zero overpotential, while molecule dynamics at constant potential indicates that the energy barrier for the  $2\text{e}^-$  pathway is lower than its  $4\text{e}^-$  counterpart.

#### 4.2.3. Co-doping by various heteroatoms

It has been recently proven that the co-doping of multiple types of heteroatom into carbon materials would increase the density of electrocatalytic active sites for two-electron or four-electron ORR processes [78]. N & S, N & B, and N & P co-doped carbon materials have been investigated for catalyzing two-electron ORR. The comparison of N-doped, S-doped, and N & S co-doped mesoporous carbons showed that a higher N content enhanced the catalytic activity while the effect of sulfur was opposite [104]. Though the N & S co-doped carbon showed a lower activity, the selectivity toward  $\text{H}_2\text{O}_2$  (75%) was higher than N-doped samples (67–69%). In similar

work, mesoporous carbons doped with either N, S, or both, were obtained by a one-pot molecular precursor auto-assembly followed by hydrothermal carbonization [105]. The dopant molecule was found to govern the ensuing structure and resulted in different average mesopore sizes (3.5 nm, 8.2 nm, 32 nm, and 34 nm corresponding to un-doped, N-doped, S-doped, and N & S co-doped carbons). The RDE test demonstrated that no beneficial effect was achieved by the co-doping of S & N. The best performance for two-electron ORR was achieved by N-doped catalyst with 4% (wt) N content and about 80% pore volume in the mesopore range. Dissimilarly, Zhu et al. introduced N, S atoms into a carbon-based cathode [106]. Results showed the optimized N & S co-doped cathode presented over 42% improvement of  $\text{H}_2\text{O}_2$  yield, which was higher than single N/S doping. Mechanism studies show that “End-on”  $\text{O}_2$  adsorption was achieved by adjusting electronic nature via N doping, while  $\text{HO}^*$  binding capability was tuned by spin density variation via S doping.

Hybrid boron-carbon-nitrogen (BCN) materials have been tested for several catalytic applications [107,108]. To increase the selectivity toward  $\text{H}_2\text{O}_2$  production, B & N co-doped carbons were prepared. BET surface area, together with the total content of B and N dopants were modulated by controlling the initial co-monomer precursor ratios [109]. Compared to solely N-doped carbon, the final loading of N by co-incorporating B with N increased significantly due to the formed isolated patches of  $h\text{-BN}$ , which provided higher activity and selectivity for the two-electron ORR. Moreover, systematic DFT calculations were performed to study the structures of different size  $h\text{-BN}$  domains doped into graphene, and different size C domains doped into an  $h\text{-BN}$  lattice [110,111]. The relationship between stimulated limiting potential and  $\text{HO}^*$  adsorption energy is shown in Fig. 5d. The results predicted 13%  $h\text{-BN}$  to have the best two-electron ORR performance.

Li et al. confirmed that N & P co-doping increases the two-electron ORR activity of cotton-stalk-derived activated carbon fibers significantly [112]. Co-doping N & P in the carbon lattice slightly changed the pore structures. Remarkably,  $(\text{NH}_4)_3\text{PO}_4$  treatment could not only embed N and P into the carbon skeleton but also introduced additional mesopores on the catalyst.

### 4.3. Functionalization

Chemical functionalization is another powerful “regulation screw” to tailor the electron density and/or electron density distribution in the materials by introducing specific electrophilic/nucleophilic, ionic, or chiral sites. Oxygen functional groups (OFGs) are the most popular species modified onto carbon-based materials.

Surface OFGs are often introduced into carbon materials by oxidation treatment. OFGs break the electrical neutrality of  $sp^2$  carbon lattice to enhance the ORR activity. Zhong et al. [113] discovered that the carboxyl group ( $\text{O}=\text{C}-\text{OH}$ ) could weaken the  $\text{CNF}-\text{O}$  bond more easily and exhibit the highest four-electron ORR activity. Moreover, all the OFGs on CNFs were found to be easily bonded with  $\text{H}_2\text{O}_2$  to furtherly reduce  $\text{H}_2\text{O}_2$  to  $\text{H}_2\text{O}$ , thus making  $n$  of the resultant materials close to 4. Until now, this was the challenge to further pinpoint the active site to a specific group still remains.

Recently, it was found reactivity of OFGs will change in different environments [114]. Kim et al. [115] prepared a mildly reduced graphene oxide (mrGO) by heating purified GO at  $100^\circ\text{C}$  flowing  $\text{N}_2$  overnight. The mrGO, which kept parts of the OFGs, showed stable peroxide formation activity together with highly selective at low overpotentials (about  $0.01 \text{ V}$ ) in  $0.1 \text{ M KOH}$  solution. The experiments proved that carbonaceous catalysts with epoxy or ring ether groups situated either at plane edges or on their basal planes,

exhibited remarkable two-electron reactivity, which was able to produce  $\text{HO}_2^-$  with nearly 100% selectivity and high stability (15 h at 0.45 V vs. RHE) in alkaline conditions. In other research with N-doped rGO [116],  $sp^2$  carbon sites located next to oxide regions were identified as dominating the ORR activity by experimental and DFT calculation, which underlined the importance of OFGs rather than nitrogen functional groups (NFGs). These references suggested that the enhancement effect of OFGs on  $\text{H}_2\text{O}_2$  production activity requires a synergistic contribution of the carbon lattice environments. Based on this assumption, Sun, et al. [117] provided a novel idea into the coupling role of carbon cluster size and OFGs in  $\text{H}_2\text{O}_2$  production. An activated coke electrocatalyst with size-tailored amorphous carbon clusters modified by OFGs yielded high activity (onset potential 0.83 V vs. RHE), high  $\text{H}_2\text{O}_2$  selectivity (~90%), and long-term stability. Based on this result and a series of control experiments, it was concluded that the size-reduced amorphous carbon lattices with abundant edges contributed to the high activity, while the basal carbon atoms in ether-modified small-size carbon planes are the most active sites towards  $\text{H}_2\text{O}_2$  selectivity.

Lu et al. [118] demonstrated a facile approach to oxidize the raw CNTs by  $\text{HNO}_3$  to obtain O-CNTs. The O-CNTs drastically lowered the needed overpotential by ~130 mV at 0.2 mA compared with raw CNTs and increased the selectivity from ~60 to ~90%. Based on DFT calculations, ester groups ( $\text{C}-\text{O}-\text{C}$ ) in the basal plane of the graphene and  $\text{O}=\text{C}-\text{OH}$  in the armchair edge were proved active and selective for  $\text{H}_2\text{O}_2$  production.

Zhang et al. [119] introduced OFGs onto the Vulcan XC-72 CB by a simple calcination method at 200–600 °C exposed to air. Characterization results showed both structural defects and OFGs content increased with the calcination temperature. Furthermore, many types of OFGs, such as  $\text{C}-\text{O}-\text{C}$ ,  $\text{C}-\text{OH}$ ,  $\text{C}=\text{O}$ , and  $\text{O}=\text{C}-\text{OH}$ , were successfully introduced onto the CB surface. With calcination at 600 °C, the RRDE onset potential increased from −0.27 V to −0.14 V (vs. Ag/AgCl) and the  $\text{H}_2\text{O}_2$  selectivity increased slightly from 47.0–56.2% to 52.6–56.1% at −0.35 to −0.6 V (vs. Ag/AgCl).

In order to reveal the nature and quantity of two-electron ORR active sites in the alkaline media, Lu, et al. [120] synthesized various oxidized carbon black (OCB) with adjustable surface OFGs ( $\text{C}=\text{O}$ ,  $\text{O}=\text{C}-\text{OH}$ ,  $-\text{C}-\text{OH}$ ) by  $\text{HNO}_3$  treatment at 30–120 °C. The OCB-120 °C had the most stable ring current and  $\lambda$  of ~60% at 0.26–0.36 V (vs. RHE). It was also observed that the intrinsic activity of  $\text{O}=\text{C}-\text{OH}$  is much higher than that of  $\text{C}=\text{O}$ .

To investigate the synergistic influence of different N doping species and OFGs in carbon materials on the  $\text{H}_2\text{O}_2$  production, N & O co-doped OMC was fabricated from HMT (hexamine), Pluronic F127, and resorcinol by a one-step hydrothermal method at 600–900 °C [121]. The 700 °C carbonization sample had 443  $\text{m}^2 \text{g}^{-1}$  BET surface area, and COOH,  $\text{C}=\text{O}$ , total N, graphitic N content together with the highest zeta potential and pyridinic N,  $\text{C}-\text{O}-\text{C}$  content (Fig. 6). DFT calculations on the account of the adsorption energy of  $\text{HOO}^*$  were applied to study the interactive effects between N species and OFGs (Fig. 6i). Compared with the pure graphitic carbon (−0.608 eV), pyridinic N (−0.289 eV), graphitic N (−0.494 eV), COOH (−0.362 eV),  $\text{C}-\text{O}-\text{C}$  (−0.175 eV) doped carbon possessed a lower  $\text{HOO}^*$  adsorption energy, which positively affects the production of  $\text{H}_2\text{O}_2$ . Among these, pyridinic N &  $\text{C}-\text{O}-\text{C}$  co-doped carbonaceous catalyst exhibited the lowest  $\text{HOO}^*$  adsorption energy (−0.092 eV), which accelerated the  $\text{HOO}^*$  protonation toward  $\text{H}_2\text{O}_2$ . Combined with the ideal dispersed performance, the 700 °C carbonization sample had the highest activity and selectivity (~95%) at 0.4 V vs. RHE.

OFGs can also be in-situ introduced onto the carbon-based electrode by physical/chemical/electrochemical methods to promote  $\text{H}_2\text{O}_2$  yield. These will be described in detail in Chapters 6 and 7 based on the electrode type and the method.

#### 4.4. Metal and metallic compound

##### 4.4.1. Non-precious metals decorated carbon

Non-noble metal (NPM)-based materials have been investigated as four-electron ORR electrocatalysts for more than a few decades. Recently, some researchers tried to load NPMs onto the carbon to test their catalytic performance for two-electron ORR. In 2011, series transition metal-carbon composite catalysts ( $M = \text{V}, \text{Fe}, \text{Co}, \text{Ni}, \text{Cu}, \text{Zn}, \text{Sn}, \text{Ba}, \text{Ce}$ ) were obtained by heating the mixture of Vulcan XC-72 CB and metal nitrate salts at a high temperature of 900 °C in  $\text{N}_2$  [122]. As shown in Fig. 7a, it is clear that Co-activated samples have outstanding performance for the electrosynthesis of  $\text{H}_2\text{O}_2$  than other samples in an acid medium. An optimized catalyst with 4% (wt) Co showed a high  $\text{H}_2\text{O}_2$  selectivity of 80–90% at 0.1–0.4 V (vs. RHE). The selectivity of ORR is also related to the geometric arrangement of atoms on the surface of the catalyst [123].  $\text{HOO}^*$  normally binds onto atop sites, whereas  $\text{O}^*$  binds onto hollow sites. Eliminating hollow sites will specifically destabilize  $\text{O}^*$  without necessarily changing the activity. Therefore, Siahrostami, et al. [36] predicted that catalysts such as Co-porphyrins that lack hollow sites might have high selectivity toward  $\text{H}_2\text{O}_2$ . Zhang et al. [124] developed a Co-based catalyst with a negligible amount of onset overpotential and nearly 100% selectivity by modulating the oxygen functional groups near the atomically dispersed cobalt sites. It was revealed that the presence of epoxy groups near the  $\text{Co}-\text{N}_4$  centers exceptionally enhanced  $\text{H}_2\text{O}_2$  generation.

##### 4.4.2. Metal carbonitrides

Because of the incremental improvement witnessed in NPM electrocatalysts, various novel efficient NPM-based catalysts were developed. Among these NPM-based electrocatalysts, metal carbonitrides, including non-pyrolyzed transition metal macrocycles and pyrolyzed NPM-N-doped carbon ( $M-\text{N}-\text{C}$ ) ( $M = \text{Fe}, \text{Ni}, \text{Co}$ , etc.) catalysts, have shown the most promising potential because of their efficient activity toward ORR.

The investigation of non-pyrolyzed transition metal macrocycles on ORR dates back to the 1960s since Jasinski [125] first discovered the promoted ORR performance by cobalt phthalocyanine with a metal- $\text{N}_4$  center. The electronic configuration of the metal centers is beneficial to bond with the  $\text{O}_2$  molecule and subsequent reduction of  $\text{O}_2$  [125]. Subsequently, multiple  $M - \text{N}_4$  macrocycles, such as porphyrins, phthalocyanines, and tetra-zaannulenes, have been widely investigated [126]. It was found that these catalysts are prone to catalyze two-electron reductions if they are adsorbed onto the surface of the electrode. The surface electrochemical behavior of adsorbed Co tetra-methoxy-phenyl porphyrin (CoTMPP) was investigated at different pH values [127]. The Co center one-electron redox process and the  $\text{N}_4$ -ring two-electron redox process were recognized during the ORR. The adsorbed CoTMPP displayed strong activity for both  $\text{O}_2$  reduction and peroxide reduction.  $\text{O}_2$  can only be reduced to the stage of  $\text{H}_2\text{O}_2$  in acidic conditions. In contrast, in neutral or alkaline solutions, the ORR was observed through a two-electron pathway in the low potential polarization range (0.13 to −0.5 V vs. SCE) and the overall four-electron pathway to  $\text{H}_2\text{O}$  in the high potential polarization range (about −0.5 to −1.5 V vs. SCE). However, the major problem of these non-pyrolyzed transition metal macrocycles is demetallation from the active sites resulting from the collapse of the macrocyclic structure caused by peroxide and superoxide intermediates during ORR [128,129].

Enlightened by the high ORR performances of the transition metal macrocyclic complexes, pyrolyzed NPM-N-doped carbon ( $M-\text{N}-\text{C}$ ), prepared via the thermal treatment of either metal  $\text{N}_4$ -macrocylic complexes or the mixture of metal salts, carbon and nitrogen precursors, have been extensively investigated. Until now,

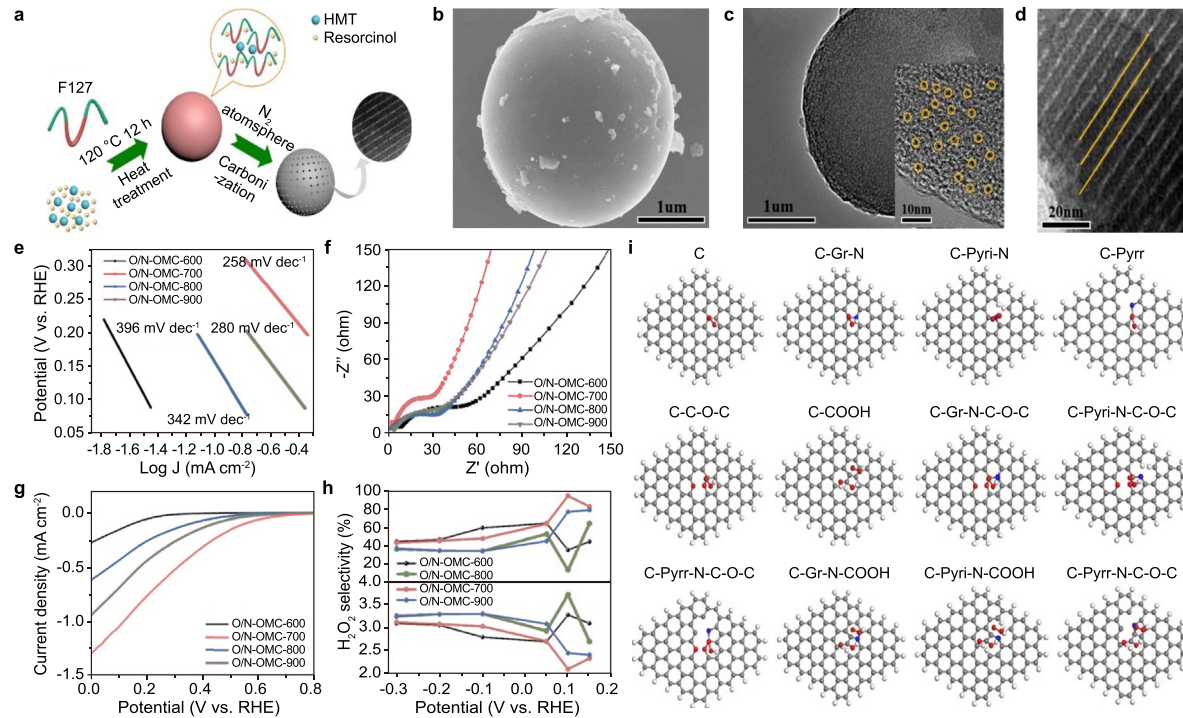


**Fig. 6.** **a**, Schematic of O and N co-doped OMC materials preparation. SEM results (**b**), TEM results (**c**) and HRTEM results (**d**) of O/N-OMC-700. Tafel plots at 1600 rpm (**e**) and EIS data (**f**) of different O, N co-doped OMCs. **g**, RDE LSV curves at 1600 rpm **h**, The selectivity toward  $\text{H}_2\text{O}_2$  and electron transfer number of different materials. **i**, The computational models for  $\text{HOO}^*$  adsorption on pure carbon materials and different types of N and OFGs co-doping. Adapted from the literature [121], with permission from Elsevier.

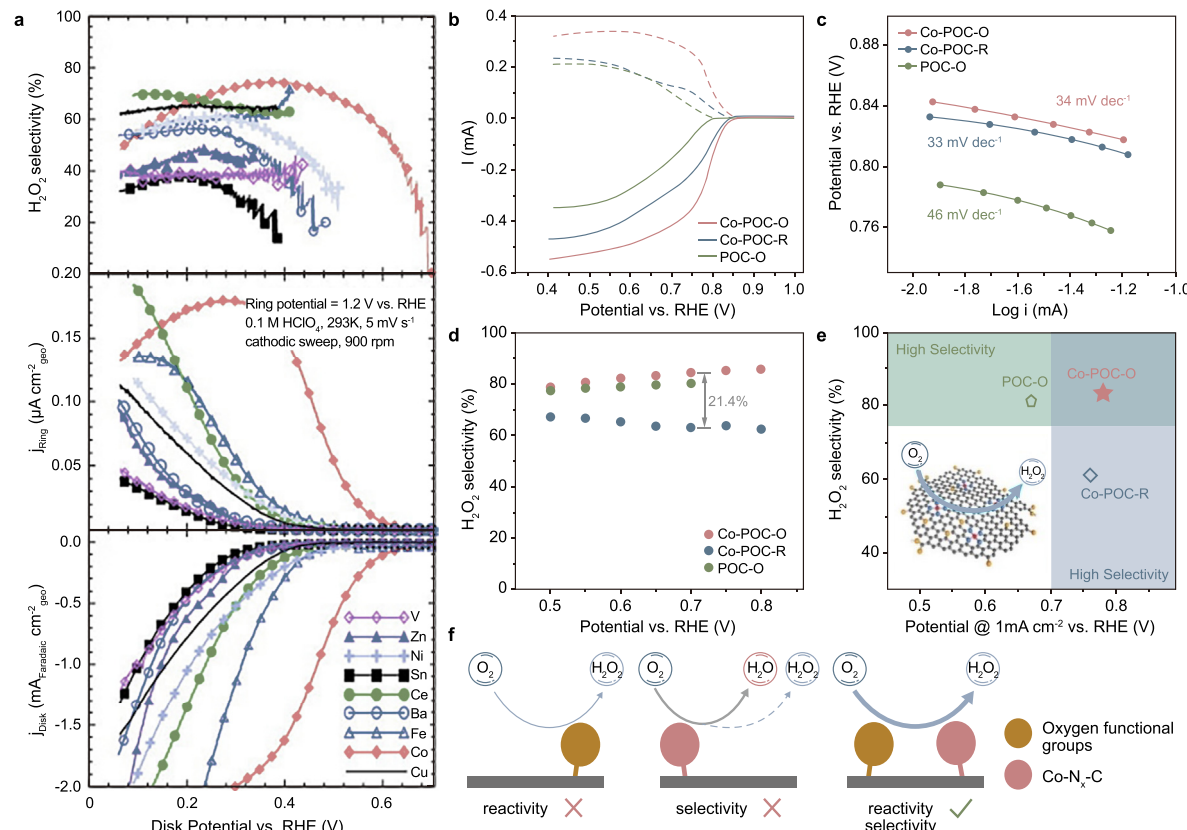


**Fig. 7.** **a**, RRDE results of different transition metal loading catalysts. The experiments were conducted in 0.1 M  $\text{HClO}_4$  electrolyte at 295 K Adapted from the literature [122], with permission from Elsevier. Mechanistic research on the Co-POC-O electro-catalyst. LSV curves at  $10 \text{ mV s}^{-1}$  (**b**), corresponding Tafel plots (**c**) of three catalysts. **d**, Calculated  $\text{H}_2\text{O}_2$  selectivity of Co-POC-O, Co-POC-R, and POC-O catalysts. **e**, Performance comparison regarding to activity and selectivity for  $\text{H}_2\text{O}_2$  generation on three catalysts. The inset in (**e**) indicates the synergistic  $\text{H}_2\text{O}_2$  generation mechanism scheme. C, O, N, and Co atoms are marked with black, yellow, blue, red, respectively. **f**, Schematic illustration of the synergistic strategy of atomic  $\text{Co-N}_x\text{-C}$  sites and OFGs for  $\text{H}_2\text{O}_2$  generation on the designed catalysts. Adapted from the literature [137], with permission from Wiley.

the role of the transition metals in the M-N-C catalysts is still controversial, and numerous types of active sites were inferred to be responsible for four-electron ORR activity [126,128,130], while the investigation on two-electron ORR was limited.

Jaouen and Dodelet [131] have confirmed that Fe or Co, together with N, followed by a pyrolysis treatment, resulted in catalytic sites highly active for two-electron or four-electron ORR. Fe-activated carbons are active for H<sub>2</sub>O production, and Co-activated carbons are reported to be responsible for reducing O<sub>2</sub> toward H<sub>2</sub>O<sub>2</sub>. However, according to the review by Bezerra et al., 2008, both Fe—N—C and Co—N—C materials catalyze the ORR mainly through a four-electron process instead of a two-electron process [132]. Campos et al. [133] reported that the electrocatalytic performance of Co catalysts obtained from nitrogen-ligands is greatly affected by heat treatment. Once the heat temperature exceeded 500 °C, a drop in H<sub>2</sub>O<sub>2</sub> selectivity resulted from the progressive formation of metallic cobalt particles. H<sub>2</sub>O<sub>2</sub> reduction was almost invisible without cobalt or when the cobalt is in the form of a complex. Olson et al. [134] have studied the ORR mechanism of Co-polypyrrole-C (CoPPy/C) in alkaline media through structure-to-property analyze. Initially, two-electron ORR occurred on a Co-Nx type site to form HO<sub>2</sub><sup>·</sup>. The HO<sub>2</sub><sup>·</sup> species further reacted either to form OH<sup>−</sup> via electrochemical reduction or to form OH<sup>−</sup> and O<sub>2</sub> by chemical decomposition. It was speculated that decorating CoxOy/Co nanoparticles appears to be the site of HO<sub>2</sub><sup>·</sup> destruction.

In summary, the M-N-C catalysts (where M = Fe or Co) were thought to exhibit high activity towards the four-electron ORR following the peroxide formation-reduction pathway (O<sub>2</sub> – H<sub>2</sub>O<sub>2</sub> – H<sub>2</sub>O) in acidic media [135]. The active sites for H<sub>2</sub>O<sub>2</sub> generation and reduction all exist in the catalysts. To obtain efficient M-N-C catalysts for H<sub>2</sub>O<sub>2</sub> formation, the suppression of H<sub>2</sub>O<sub>2</sub> further reduction is pivotal. Recently, researchers have tried to obtain highly active and selective M-N-C two-electron ORR catalysts by introducing other functional groups. Byeon et al. [136] demonstrated that co-doping of MnO nanoparticles together with Mn-Nx moieties into carbon are efficient for peroxide production  $\lambda$  of 74% at 0.2 V (vs. RHE). The favored two-electron ORR resulted from the increasing number of Mn-Nx sites inside the mesoporous N-doped carbon. Moreover, strong evidence showed that a further reduction of H<sub>2</sub>O<sub>2</sub> was remarkably suppressed by adjacent MnO species. Li et al. [137] pointed out that the atomic Co-Nx-C sites improve the ORR activity but lack the selectivity for H<sub>2</sub>O<sub>2</sub> generation, while OFGs promote the selectivity for the two-electron ORR but exhibit limited kinetics for ORR. Therefore, a rational combination of Co-Nx-C sites and OFGs into 3D interconnected conductive hosts was prepared by heating the predesigned precursor prior to HNO<sub>3</sub> treatment (noted as Co-POC-O). The Co-POC-O exhibited excellent catalytic performance in KOH (0.1 M) with a high onset potential (0.84 V vs. RHE) and selectivity of over 80%. Moreover, the synergy effect of atomic Co-Nx-C reactive sites and OFGs was identified by the control samples with only atomic Co-Nx-C reactive sites (Co-POC-R) or only OFGs (POC-O) (Fig. 7b–f).

#### 4.4.3. Metal alloy/oxide decorated carbon

Multiple metal oxides, especially group IV and V metals, are proven to be catalyst supports to replace carbon materials due to their abundant surface hydroxyl groups and chemical stability in acidic electrolytes [130,138]. However, their bulk form exhibit extremely low ORR activity resulting from the poor electrical conductivity and reduced reactive sites for oxygen species adsorption. Recently, alloying, forming highly dispersed nanoparticles, and reducing the crystalline sizes have been reported as an effective way to enhance the catalytic activities of metal oxides by increasing their exposed reactive sites, surface available defects, and electrical conductivity. Different carbon varieties were modified by various

metal alloys or metal oxides with nanostructure to improve the two-electron ORR of carbonaceous electrocatalysts. Typically, the synthesized or purchased metal composites were supported onto the carbon by a modified polymeric precursor method [139] or sol-gel method [140]. Vulcan XC-72(R) with  $n = 3.1\text{--}2.5$  and  $\lambda = 41\text{--}73\%$  was used frequently in Santos' team as the support to study the catalytic capacity of two-electron ORR. After being modified with V<sub>2</sub>O<sub>5</sub>, SnNi, WO<sub>2.72</sub>, MnO<sub>2</sub>, or W@Au, the  $n$  of metallic nanostructure modified CB decreased to 2–2.6, while  $\lambda$  increased to 68–96% [141–146]. Among them, a core-shell type W@Au nanostructures (1% W@Au/CB) presented the highest selectivity toward H<sub>2</sub>O<sub>2</sub> with  $n$  of ~2 [147].

Printex L6 CB (BET surface area of ~250 m<sup>2</sup> g<sup>−1</sup>, primary particle size of 18 nm and density of 1.8 g cm<sup>−3</sup>) with a  $\lambda$  of 65.3–68% and  $n$  of 2.6–2.7 was another important carrier to develop metal compounds nanoparticles modified carbonaceous electrocatalysts for two-electron ORR [148,149]. After preparation optimization, 4% CeO<sub>2</sub>/CB specimen showed a  $\lambda = 88\%$  and  $n = 2.2$  at −0.4 V vs. Hg/HgO, while Ta<sub>2</sub>O<sub>5</sub>/CB (5% (w/w) Ta/C) exhibited a  $\lambda = 83.2\%$  and  $n = 2.3$  at −0.3 to −0.5 V (vs. Ag/AgCl). A  $\lambda$  of 1% Pd/CB was over 80% at about 0 V (vs. Ag/AgCl) [150]. In another work, the synthesized rGO with mean particle size of 5.7 ± 0.8 nm showed  $\lambda = 73.7\%$  and  $n = 2.52$ . With the Nb<sub>2</sub>O<sub>5</sub> loading, Nb<sub>2</sub>O<sub>5</sub>/rGO composite (Nb/GO = 15% w/w) exhibited  $\lambda = 85.3\%$  and  $n = 2.28$  (−0.20 to −0.40 V vs. Ag/AgCl) [151]. In contrast, after loading 5% Fe<sub>3</sub>O<sub>4</sub> nanoparticles, the  $\lambda$  of Fe<sub>3</sub>O<sub>4</sub>/rGO was only 62% [152].

Based on the above research, the conclusions were that the decoration of metallic nanostructures would bring more acidic oxygen species or special morphology to the surface of the carbons, resulting in a more acidic and hydrophilic surface, and thus improving H<sub>2</sub>O<sub>2</sub> generation by enhancing oxygen adsorption or oxygen diffusion.

#### 4.5. Engineering defect and porosity

Some researchers claimed the doped heteroatoms are the real ORR active sites in the carbon structures [81,82,84,87], however, another group of research recently proved that defects created by heteroatoms might be the actual active sites [153,154]. Some novel carbon-based electrocatalysts were developed with the guidance of this newly established defect-driven catalysis mechanism. In this section, we will not discuss this mechanism debate. Instead, we will provide a new insight on the mechanism for ORR and give specific examples on promoting two-electron ORR by creating different defective carbon materials.

Perfect and defective graphene clusters are summarized and plotted in Fig. 8a. The Graphene with G585 divacancy defects (consisting of two pentagons and one octagonal) facilitated the O<sub>2</sub> adsorption and lowered the following reaction energy barriers. DFT calculations showed that the point and line defects in graphene could tailor the local electronic structures and the distributions of nearby carbon atoms [155]. A pentagon ring located at the zigzag edge, the odd number of octagon ring, and fused pentagon ring line at the edge of the defective graphene are all proposed to be ORR active sites (Fig. 8). Hu and co-workers proposed that pentagon and zigzag edge defects are more reactive in four-electron ORR [156]. Moreover, defective graphene fabricated by N doping following a removal approach was a trifunctional catalyst for the four-electron ORR, hydrogen evolution reaction, and oxygen evolution reaction [157]. DFT models predicted N-doped into the graphene is beneficial to lower the adsorption energy of O<sub>2</sub> but unfavorable for the reduction.

These results proved the versatility of the defect-driven catalysis for electrocatalysis. However, until now, insufficient effort has been placed on understanding what defective active sites selectively promote the two-electron ORR. Only a few research applied the

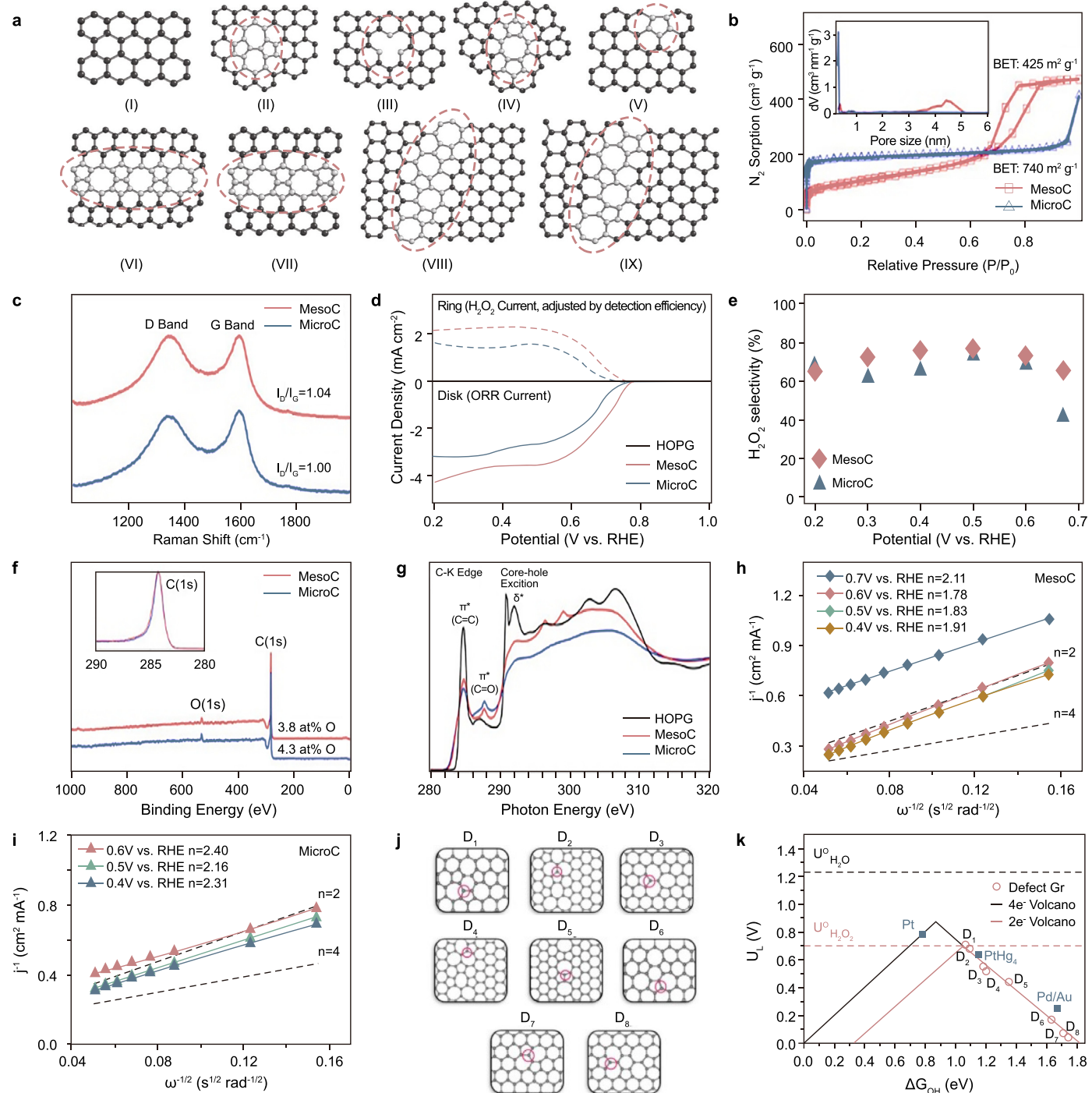


**Fig. 8.** **a**, Perfect and typical defective graphene clusters. (I) Perfect graphene cluster, (II) Stone-Wales defect, (III) single vacancy, (IV) double vacancies, (V) edge defect with pentagon ring at zigzag edge, octagon, and fused pentagon carbon rings line defect with (VI) an odd number of octagon rings (GLD-558-01) and (VII) an even number of octagon rings (GLD-558-02), and pentagon-heptagon pairs line defects with (VIII) an odd number of heptagon rings (GLD-57-01) and (IX) an even number of heptagon rings (GLD-57-02). All these defect styles are re-drawn from literature [155]. **b**, Nitrogen adsorption-desorption isotherms together with pore size distributions of obtained MesoC and MicroC. **c**, Raman spectra of obtained MesoC and MicroC. **d**, XPS survey scan for obtained MesoC and MicroC. The C1s peak spectrum is shown in the inset. **e**, NEXAFS spectra of the C-K edge for different catalysts. **f**, RRDE LSV curves at 1600 rpm in 0.1 M KOH O<sub>2</sub>-saturated electrolyte. **g**, H<sub>2</sub>O<sub>2</sub> selectivity at a different applied potential. Corresponding K-L plots of MesoC (**h**) and MicroC (**i**) at different applied potentials. **j**, Different defect type configurations were investigated in the study. D1-D8 are double-vacancy defects with nonhexagonal ring members. D1 and D6 show different active sites in 555-6-777 double vacancies. D2 and D4 stand for 555-777 line defects, and D2 represents 55-8-55 line defects. D3, D7, and D8 are 555-777, 55-77, and 5555-6-7777 double vacancy defects. **k**, ORR-related volcano plots are displayed as a function of ΔG<sub>OH</sub>. Blue squares display the activities of the Pt (111) surface from literature [111]. PtHg<sub>4</sub> and Pd-Au alloys are from literature [36]. Adapted from the literature [160], with permission from the American Chemical Society.

defect-driven catalysis mechanism to design and explore two-electron ORR materials.

Carbonization of MOF-5 under H<sub>2</sub> will transform *sp*<sup>2</sup>-C bonds to *sp*<sup>3</sup>-C bonds [158]. The harvested hierarchical porous carbons (HPC)

exhibited H<sub>2</sub>O<sub>2</sub> selectivity of 80.9–95% in acid solution (pH 1 and 4), with both defects and *sp*<sup>3</sup>-C acting as active sites of two-electron ORR. This research certified the un-doped and un-functionalized defective carbon also has potential for the two-electron

mechanism. However, later researchers presented opposing views about the active sites. For example, Tao, et al. [159] confirmed that the defect  $sp^3$  carbon atoms served as main active sites for four-electron ORR instead of two-electron ORR. Chen et al. [160], Kim, et al. [161] all stated the active sites of two-electron ORR are from  $sp^2$  carbons.

Chen et al. [160] have experimentally and theoretically investigated the defect and pore size effect to the electrochemical  $H_2O_2$  synthesis. Two porous carbon catalysts (predominantly microporous/mesoporous carbon, Micro C, and Meso C) were synthesized from similar precursors but different synthetic procedures. Characterizations showed the two materials had similar chemical identity and content of defects but different pore structures (surface area, pore size, and pore volume) (Fig. 8b–e). Electrochemical tests showed both carbons exhibit high activity with an onset potential of about 0.7 V (vs. RHE) and selectivity of >70% toward  $H_2O_2$  (Fig. 8f–i). The better performance of the Meso C was attributed to the easier mass transfer in mesoporous structures. Spectroscopic analyses revealed that microporous/mesoporous carbon (Micro C and Meso C) contain  $sp^2$ -type defects that might be the reactive sites for the two-electron ORR. DFT calculations indicated that the pentagon edge, single vacancies (SV), and 585 double vacancies (DV) in 2D graphene sheets are too reactive to contribute to ORR. While some of the defect configurations (555-6-777, 555-777 line defect, and 555-777 point defects) were identified as having comparable activity with PtHg<sub>4</sub> (Fig. 8j and k) (the ideal catalyst until now shown in Fig. 2b and c) for the two-electron ORR. Kim et al. [161] developed two N-rGO materials with different defect compositions. Based on the nuclear magnetic resonance technique and other X-ray-based tools,  $sp^2$  carbon defects associated with epoxy or ether groups were identified to play a more critical role in promoting  $H_2O_2$  formation than other functionalities, such as N defects or carboxylic acid edge sites.

In recent research [162], the functionalized graphene sample with the largest electrochemical active surface area and the highest in-plane carbon defect density did not show the most efficient ORR activity and  $H_2O_2$  selectivity, which was due to excess in-plane carbon defects that would lead to a conductivity decrease. In comparison, the graphene sample with the lowest in-plane carbon defect density had the highest  $H_2O_2$  selectivity. These results emphasized that the optimization of graphene precursors defect site density is pivotal for adjusting the catalysts' catalytic activity and reaction pathway. Defect modulation is regarded as a burgeoning strategy to regulate the electronic structure of carbon-based materials.

## 5. Evaluation parameters of $H_2O_2$ -generating electrodes

The Electrode is the key component of the electrochemical cell because it contacts the electrolyte and provides the reaction sites for the reactants. Ideal carbon-based electrodes must possess a large surface area, suitable porosity, internal channels, and low electronic resistance for high electrochemical activity. The following chapters mainly introduce the development of formed carbon-based electrodes, including general electrode preparation methods, various physical and chemical modification methods, and their applications. There are two kinds of modification methods for enhancing two-electron ORR activity of the electrodes: (1) modify the pristine electrodes (graphite plate & rod, graphite felt, reticulated vitreous carbon, and activated carbon fibers, Fig. 9a) by physical/chemical methods to tune the surface properties or to load effective two-electron ORR functional groups (N, O) onto the electrode surface; (2) use the pristine carbon electrodes as support and introduce other highly active & selective carbon materials, such as CNTs, CB, and graphene (Fig. 10a). For example, carbon felt and

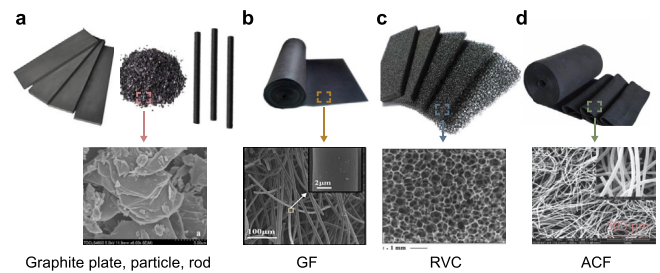


**Fig. 9.** Photos and SEM images of graphite (a), graphite felt (b), reticulated vitreous carbon (RVC) (c), and activated carbon fibers or fabrics (ACF) materials (d). Adapted from the literature [168,192,218,232], with permission from Elsevier.

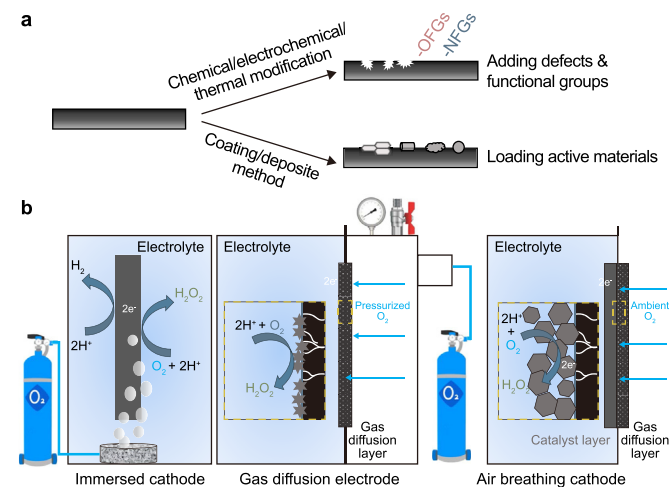


**Fig. 10.** a. Different types of carbon electrode modification. b. Schematic mechanism on  $H_2O_2$  production on conventionally submerged electrodes, GDE, and air-breathing cathode.

carbon paper are often used as soft current collectors for in situ construction of electroactive nano-carbon structures due to their simple handling and excellent conductivity.

Various electrochemical testing techniques can be applied to investigate the electrochemical activity and interface properties of formed electrodes, including linear sweeping voltammetry (LSV), cyclic voltammetry (CV), electrochemical impedance spectroscopy (EIS), chronoamperometry (CA), and scanning electrochemical microscopy (SECM) in the three-electrode system [163]. The above test results can be used to support the demonstration of electrode performance and mechanism analysis. In our estimation, the most critical parameter is the  $H_2O_2$  yield and the current efficiency of the electrodes. In order to contrast the performance of electrodes clearly and intuitively, the expression of  $H_2O_2$  yield in this paper was uniformly transformed to  $mg\text{ h}^{-1}$  unless specially noted. The current efficiency (CE, also known as Faradaic efficiency) of the cathodes was calculated from Eq. (25):

$$\text{CE} = \frac{nFC_{H_2O_2}V}{It} \times 100\% \quad (25)$$

where  $n$  is the number of the transferred electrons from  $O_2$  to  $H_2O_2$  ( $n = 2$ ),  $F$  represents the Faraday constant ( $96,486\text{ C mol}^{-1}$ ),  $C_{H_2O_2}$  represents the concentration of  $H_2O_2$  ( $\text{mol L}^{-1}$ ),  $V$  stands for the bulk volume (L),  $I$  is the current (A), and  $t$  is the time (s). The performances of all mentioned cathodes are summarized in Table 3, including the electrolyte conditions, operation mode,  $H_2O_2$  yield, and CE.

**Table 3**

$\text{H}_2\text{O}_2$  yield with CE of the cathodes and their operation conditions in literature summarized in Chapter 6,7 and 8. The value with 'cal' means the value was not given directly and it was calculated by us. The value with 'obs' means the value was not given directly and it was observed in the figure.

Electrode type	Electrode Size	Electrolyte Conditions	Potential/ Current	Air/ $\text{O}_2$ Flow Rate	$\text{H}_2\text{O}_2$ Yield	Current Efficiency (%)	Ref
PPy/AQDS modified graphite	3 × 3.5 cm	100 mM $\text{Na}_2\text{SO}_4$ , pH = 3, 200 mL	-0.65 V vs. SCE	$\text{O}_2$ : 20 L $\text{h}^{-1}$	4 mg $\text{h}^{-1}$	64–73	[172]
anodized GF	5 × 2 × 0.5 cm	50 mM $\text{Na}_2\text{SO}_4$ , pH = 6.4, 130 mL	-0.65 V vs. SCE	$\text{O}_2$ : 0.4 L $\text{min}^{-1}$	15.3 mg $\text{h}^{-1}$	79	[196]
hydrazine hydrate modified GF	5 × 2 × 0.5 cm	50 mM $\text{Na}_2\text{SO}_4$ , pH = 6.4, 130 mL	-0.65 V vs. SCE	$\text{O}_2$ : 0.4 L $\text{min}^{-1}$	11.5 mg $\text{h}^{-1}$	81	[189]
CB modified GF	5 × 4 × 0.5 cm	50 mM $\text{Na}_2\text{SO}_4$ , pH = 7, 100 mL	100 mA	no external aeration	47.3 mg $\text{h}^{-1}$	75	[202]
$\text{HNO}_3$ modified GF	27 × 7 cm	50 mM $\text{Na}_2\text{SO}_4$ , pH = 3, 2500 mL	20 V	$\text{O}_2$ : 4 L $\text{min}^{-1}$	742.5 mg $\text{h}^{-1}$	unknown	[194]
KOH activated GF at 900 °C	2 × 2 cm	100 mM $\text{Na}_2\text{SO}_4$ , pH = 3, volume unknown	-0.7 V vs. SCE	$\text{O}_2$ : 0.6 L $\text{min}^{-1}$	40 mg $\text{L}^{-1} \text{ h}^{-1}$	unknown	[192]
KOH activated GF at 400 °C	6 × 4 × 0.5 cm	50 mM $\text{Na}_2\text{SO}_4$ , pH = 3, 300 mL	50 mA	$\text{O}_2$ : 0.6 L $\text{min}^{-1}$	~30 mg $\text{L}^{-1}$	~94.6 (cal)	[193]
N,O and S doped GF	8 × 8 × 0.5 cm	50 mM $\text{Na}_2\text{SO}_4$ , pH = 3, 400 mL	640 mA	$\text{O}_2$ : 0.36 L $\text{min}^{-1}$	47.9 mg $\text{h}^{-1}$	11.8 (cal)	[191]
gaseous acetic acid activated GF polarity reversal anodized GF	unknown unknown	50 mM $\text{Na}_2\text{SO}_4$ , pH = 7, 30 mL 50 mM $\text{Na}_2\text{SO}_4$ , pH = 7, 180 mL	-0.7 V vs. SCE 100 mA	$\text{O}_2$ : 0.6 L $\text{min}^{-1}$ no external aeration	10.3 mg $\text{h}^{-1}$ 8.1 mg $\text{h}^{-1}$	75 ~13 (cal)	[195] [197]
graphene ink-coated carbon cloth Commercial graphene foam cathode (Graphene Supermarket USA)	5 × 3 cm 5 × 4 cm	50 mM $\text{K}_2\text{SO}_4$ , pH = 3, 80 mL 50 mM $\text{K}_2\text{SO}_4$ , pH = 3, 150 mL	1.25 mA $\text{cm}^{-2}$ 0.4 mA $\text{cm}^{-2}$	air: 0.2 L $\text{min}^{-1}$ air: rate unknown	2.72 mg $\text{h}^{-1}$ 1 mg $\text{h}^{-1}$	11.4 (cal) 18.1 (cal)	[211] [207]
EEGr & CB modified GF	2 × 2.5 cm	50 mM $\text{Na}_2\text{SO}_4$ , pH = 7, 100 mL	-0.9 V vs. SCE	air: 0.7 L $\text{min}^{-1}$	38.5 mg $\text{h}^{-1}$	~57 (obs)	[214]
MWCNT & CB modified GF	2 × 5 cm	50 mM $\text{Na}_2\text{SO}_4$ , pH = 5.5, 300 mL	120 mA	air: 0.6 L $\text{min}^{-1}$	48 mg $\text{h}^{-1}$	63	[206]
ErGO on LCD glass electrode	10 cm <sup>2</sup>	50 mM $\text{Na}_2\text{SO}_4$ , pH = 3.5, 150 mL	-1.5 V vs. Ag/ AgCl	air: 1 L $\text{min}^{-1}$	2.25 mg $\text{h}^{-1}$	59	[210]
$\text{N}_3$ -doped EEGr & CB modified GF	4 × 2.5 cm	50 mM $\text{Na}_2\text{SO}_4$ , pH = 7, 100 mL	-1.1 V vs. SCE	air: 0.75 L $\text{min}^{-1}$	86 mg $\text{h}^{-1}$	unknown	[216]
N-doped EEGr & CB modified GF	4 × 2.5 cm	50 mM $\text{Na}_2\text{SO}_4$ , pH = 7, 100 mL	-0.9 V vs. SCE	air: 0.7 L $\text{min}^{-1}$	62 mg $\text{h}^{-1}$	unknown	[215]
electrochemically oxidized GF	2 × 3 × 0.5 cm	5g $\text{L}^{-1}$ $\text{Na}_2\text{SO}_4$ , pH = 7, 120 mL	100 mA	$\text{O}_2$ : 0.5 L $\text{min}^{-1}$	9 mg $\text{h}^{-1}$	~14 (cal)	[198]
N-doped carbon modified GF	2 × 2 cm	50 mM $\text{Na}_2\text{SO}_4$ , pH = 7, 150 mL	100 mA	no external aeration	6 mg $\text{h}^{-1}$	~9.3 (cal)	[200]
N-doped carbon electrodeposited on GF	2.5 × 3 cm	50 mM $\text{Na}_2\text{SO}_4$ , pH = 3, 100 mL	-0.6 V vs. Ag/ AgCl	air: 0.6 L $\text{min}^{-1}$	4.6 mg $\text{h}^{-1}$	unknown	[201]
Janus GF	2 × 3 × 0.32 cm	50 mM $\text{Na}_2\text{SO}_4$ , pH = 7, 150 mL	50 mA	no external aeration	8.9 mg $\text{h}^{-1}$	28.1 (cal)	[278]
QEEGr composite electrode	5 × 2 cm	50 mM $\text{Na}_2\text{SO}_4$ , pH = 3, 100 mL	-1.2 V vs. Ag/ AgCl	air: 1 L $\text{min}^{-1}$	5 mg $\text{h}^{-1}$	unknown	[213]
CNTs immobilized on graphite	4 × 9 cm	50 mM $\text{Na}_2\text{SO}_4$ , pH = 3, 1000 mL	100 mA	air: 2.5 L $\text{min}^{-1}$	1.4 mg $\text{h}^{-1}$	~2.1 (cal)	[173]
graphite-CNT sandwich-like cathode	8 × 2 × 1 cm	100 mM $\text{Na}_2\text{SO}_4$ , pH = 3, 100 mL	-1.3 V vs. SCE	air: 2.5 L $\text{min}^{-1}$	37.6 mg $\text{h}^{-1}$	40	[178]
ppy/MWCNT modified on graphite	10 cm <sup>2</sup>	100 mM $\text{Na}_2\text{SO}_4$ , pH = 3, volume unknown	-0.55 V vs. SCE	air: 0.3 L $\text{min}^{-1}$	3.4 mg $\text{h}^{-1}$	unknown	[176]
PANI/MWCNT modified on stainless steel	6 cm <sup>2</sup>	100 mM $\text{Na}_2\text{SO}_4$ , pH = 2, 150 mL	-0.6 V vs. SCE	air: 0.3 L $\text{min}^{-1}$	1.1 mg $\text{h}^{-1}$	~42 (obs)	[177]
N & S co-doped electrode	1 × 2 cm	50 mM $\text{Na}_2\text{SO}_4$ , pH = 3, 100 mL	50 mA	$\text{O}_2$ : 0.4 L $\text{min}^{-1}$	1.59 mg $\text{h}^{-1}$	5 (cal)	[106]
Commercial ACF felt	20 cm <sup>2</sup>	50 mM $\text{Na}_2\text{SO}_4$ , pH = 3, 500 mL	500 mA	$\text{O}_2$ : 0.1 L $\text{min}^{-1}$	3.6 mg $\text{h}^{-1}$	~1.1 (cal)	[226]
Commercial ACF	10 × 9 cm	50 mM $\text{Na}_2\text{SO}_4$ , pH = 3, 1000 mL	8.89 mA $\text{cm}^{-2}$	air: 0.45 L $\text{min}^{-1}$	4.7 mg $\text{h}^{-1}$	~1 (cal)	[228]
ACF@rGO@OMC Cathode	3 × 3 cm	100 mM $\text{Na}_2\text{SO}_4$ , pH = 7, 100 mL	-0.7 V vs. SCE	$\text{O}_2$ : 0.3 L $\text{min}^{-1}$	2.8 mg $\text{h}^{-1}$	40.4	[231]
ACSS composite electrode	2 × 4 cm	50 mM $\text{Na}_2\text{SO}_4$ , pH = 7, 180 mL	100 mA	no external aeration	1.9 mg $\text{h}^{-1}$	~3 (cal)	[230]
Commercial ACF felt	4 × 5 cm	50 mM $\text{Na}_2\text{SO}_4$ , pH = 3, 125 mL	18 mA $\text{cm}^{-2}$	unknown	4.1 mg $\text{h}^{-1}$	1.8 (cal)	[229]
anodically polarized RVC electrode	3.2 × 2.5 × 0.5 cm	250 mg $\text{L}^{-1}$ $\text{Na}_2\text{SO}_4$ , pH = 7, 400 mL	24 mA	$\text{O}_2$ : 0.4 L $\text{min}^{-1}$	6.4 mg $\text{h}^{-1}$	43 (4 h average)	[222]
Commercial RVC electrode	2 × 2.5 × 1 cm	$\text{Na}_2\text{SO}_4/\text{NaHSO}_4$ buffer solution, 100 mL	35 mA	$\text{O}_2$ : 0.2 L $\text{min}^{-1}$	9.6 mg $\text{h}^{-1}$	~43 (cal)	[221]
Vulcan XC-72 CB PTFE GDE	3.1 cm <sup>2</sup>	50 mM $\text{Na}_2\text{SO}_4$ , pH = 3, 100 mL	300 mA	$\text{O}_2$ : 0.02 L $\text{min}^{-1}$	53.2 mg $\text{h}^{-1}$	unknown	[237]
TBAQ/Printex L6 CB GDE	19 cm <sup>2</sup>	100 mM $\text{K}_2\text{SO}_4$ , pH = 1, 400 mL	-1.0 V vs. SCE	$\text{O}_2$ : 0.2 bar	80.3 mg $\text{h}^{-1}$	unknown	[246]
Ta <sub>2</sub> O <sub>5</sub> /Printex L6 GDE	3.4 cm <sup>2</sup>	100 mM $\text{K}_2\text{SO}_4$ , pH = 2, 400 mL	-1.0 V vs. Ag/ AgCl	$\text{O}_2$ : 0.2 bar	11.2 mg $\text{h}^{-1}$	unknown	[148]

**Table 3** (continued)

Electrode type	Electrode Size	Electrolyte Conditions	Potential/ Current	Air/O <sub>2</sub> Flow Rate	H <sub>2</sub> O <sub>2</sub> Yield	Current Efficiency (%)	Ref
Pd/Printex L6 GDE	2.7 cm <sup>2</sup>	50 mM Na <sub>2</sub> SO <sub>4</sub> , pH = 2.5, 150 mL	33.3 mA cm <sup>-2</sup> O <sub>2</sub> : 0.5 L min <sup>-1</sup>	15.1 mg h <sup>-1</sup>	26.5 (cal)	[150]	
W@Au/Vulcan XC-72R GDE	4.9 cm <sup>2</sup>	100 mM K <sub>2</sub> SO <sub>4</sub> , 100 mM H <sub>2</sub> SO <sub>4</sub> , 350 mL	-1.1 V vs. Ag/ O <sub>2</sub> : 0.2 bar AgCl	21 mg h <sup>-1</sup>	unknown	[147]	
WO <sub>2.72</sub> /Vulcan XC-72R GDE	4.9 cm <sup>2</sup>	100 mM K <sub>2</sub> SO <sub>4</sub> , 100 mM H <sub>2</sub> SO <sub>4</sub> , 350 mL	-1.3 V vs. Ag/ O <sub>2</sub> : 0.2 bar AgCl	102.4 mg h <sup>-1</sup>	unknown	[144]	
V <sub>2</sub> O <sub>5</sub> /Vulcan XC-72R GDE	19 cm <sup>2</sup>	100 mM K <sub>2</sub> SO <sub>4</sub> , 100 mM NaOH, 250 mL	-1.5 V vs. Ag/ O <sub>2</sub> : 0.2 bar AgCl	77.5 mg h <sup>-1</sup>	unknown	[142]	
CeO <sub>2</sub> /Vulcan XC-72R GDE	19 cm <sup>2</sup>	100 mM NaOH, 250 mL	-1.1 V vs. Ag/ O <sub>2</sub> : 0.2 bar AgCl	50.8 mg h <sup>-1</sup>	unknown	[141]	
MnO <sub>2</sub> /Vulcan XC-72 GDE	3 cm <sup>2</sup>	100 mM K <sub>2</sub> SO <sub>4</sub> , 100 mM H <sub>2</sub> SO <sub>4</sub> , 350 mL	-1.1 V vs. Ag/ O <sub>2</sub> : 0.2 bar AgCl	68.4 mg h <sup>-1</sup>	unknown	[145]	
Vulcan XC-72R CB GDE	5 × 2 × 0.05 cm	200 mM Na <sub>2</sub> SO <sub>4</sub> , pH = 4, 15 mL	520 mA	air: 0.055 L min <sup>-1</sup>	158 mg h <sup>-1</sup>	~48 (cal)	[241]
CNT GDE	diameter 2.5 cm	50 mM Na <sub>2</sub> SO <sub>4</sub> , pH = 3, 250 mL	100 mA	O <sub>2</sub> : 0.14 L min <sup>-1</sup>	24.3 mg h <sup>-1</sup>	~38 (cal)	[247]
TBAQ modified CNT GDE	diameter 3 cm	50 mM Na <sub>2</sub> SO <sub>4</sub> , pH = 3, 300 mL	50 mA	air: 0.4 L min <sup>-1</sup>	30.1 mg h <sup>-1</sup>	94.8	[250]
(Co, S, P)-decorated MWCNT GDE	20 cm <sup>2</sup>	50 mM Na <sub>2</sub> SO <sub>4</sub> , pH = 3, 2500 mL	800 mA	air: 8.6 kPa	225.3 mg h <sup>-1</sup>	51–54	[255]
CoS <sub>2</sub> -MWCNTs GDE	3 cm <sup>2</sup>	50 mM Na <sub>2</sub> SO <sub>4</sub> , pH = 3, 150 mL	300 mA	O <sub>2</sub> : 0.2 bar, 0.5 L min <sup>-1</sup>	95.2 mg h <sup>-1</sup>	~50 (cal)	[254]
N-rGO & CNT-PTFE GDE	2 × 2 cm	50 mM Na <sub>2</sub> SO <sub>4</sub> , pH = 3, 100 mL	-0.2 V vs SCE	O <sub>2</sub> : 0.45 L min <sup>-1</sup>	1.1 mg h <sup>-1</sup>	unknown	[261]
MWCNT&CB-PTFE GDE	28.3 cm <sup>2</sup>	50 mM Na <sub>2</sub> SO <sub>4</sub> , pH = 7, 123.5 mL	100 mA	O <sub>2</sub> : 0.09 L min <sup>-1</sup>	41.3 mg h <sup>-1</sup>	65.1	[262]
P-doped CNT GDE	4.5 × 6 cm	100 mM Na <sub>2</sub> SO <sub>4</sub> , pH = 7, 160 mL	-0.7 V vs SCE	O <sub>2</sub> : 0.21 L min <sup>-1</sup>	206.6 mg h <sup>-1</sup>	88.5	[256]
CB & graphite-PTFE GDE	diameter 3.5 cm	50 mM Na <sub>2</sub> SO <sub>4</sub> , pH = 7, 840 mL	86 mA	no external aeration	50.3 mg h <sup>-1</sup>	92	[267]
CB & graphite-PTFE <sub>0.57</sub> GDE	diameter 3.5 cm	50 mM Na <sub>2</sub> SO <sub>4</sub> , pH = 7, 28 mL	140 mA	no external aeration	74.6 mg h <sup>-1</sup>	84	[273]
rGO & graphite-PTFE GDE	12 cm <sup>2</sup>	50 mM Na <sub>2</sub> SO <sub>4</sub> , pH = 3, 200 mL	24 mA	O <sub>2</sub> : 20 L h <sup>-1</sup>	12.5 mg h <sup>-1</sup>	~40 (obs)	[257]
F-doped HPC coated on carbon paper floating cathode from Oxidized CB	7.5 cm <sup>2</sup> 9.6 cm <sup>2</sup>	50 mM Na <sub>2</sub> SO <sub>4</sub> , pH = 2, 30 mL 100 mM Na <sub>2</sub> SO <sub>4</sub> , pH = 6.8, 50 mL	-0.6 V vs SCE -1.0 V vs. Ag/ AgCl	O <sub>2</sub> : 0.3 L min <sup>-1</sup> no external aeration	65.8 mg h <sup>-1</sup> 51.8 mg h <sup>-1</sup>	unknown ~62.7	[101] [119]
Quinone Compounds Modified CB GDE	19 cm <sup>2</sup>	100 mM K <sub>2</sub> SO <sub>4</sub> , 100 mM H <sub>2</sub> SO <sub>4</sub> , 400 mL	1900 mA	O <sub>2</sub> : 0.2 bar	77.1 mg h <sup>-1</sup>	~6.4	[171]
CB@CF NADE	3 × 1.7 cm	50 mM Na <sub>2</sub> SO <sub>4</sub> , pH = 7, 250 mL	1200 mA	no external aeration	518.5 mg h <sup>-1</sup>	66.8	[277]
GF-HNO <sub>3</sub> -EC-N <sub>2</sub> floating GF electrode	2 × 2 cm 2 × 3 × 0.32 cm	50 mM Na <sub>2</sub> SO <sub>4</sub> , pH = 3, 50 mL 50 mM Na <sub>2</sub> SO <sub>4</sub> , pH = 7, 180 mL	0 V vs RHE 100 mA	O <sub>2</sub> : 0.08 L min <sup>-1</sup> no external aeration	9 mg h <sup>-1</sup> 13.3 mg h <sup>-1</sup>	86 21	[199] [283]
g-C <sub>3</sub> N <sub>4</sub> @GDE Anthraquinone modified C <sub>3</sub> N <sub>4</sub> GDE	1 cm × 2 cm 1 cm <sup>2</sup>	50 mM Na <sub>2</sub> SO <sub>4</sub> , pH = 3, 50 mL 500 mM PBS, pH = 7.4, volume unknown	50 mA -0.22 V vs RHE	O <sub>2</sub> : 0.4 L min <sup>-1</sup> O <sub>2</sub> purge, rate unknown	5.2 mg h <sup>-1</sup> 1.02 mg h <sup>-1</sup>	16.3 (cal) 42.2	[263] [245]
Ni–O–C GDE	1 cm <sup>2</sup>	1 M Na <sub>2</sub> SO <sub>4</sub> , pH = 7, 20 mL	0 V vs RHE	O <sub>2</sub> flow, rate unknown	59.3 mg h <sup>-1</sup>	90.4	[276]

## 6. Development of immersed carbon-based materials electrodes

### 6.1. Graphite based cathodes

#### 6.1.1. Graphite rods, plates, and particles

Graphite has excellent chemical stability and electrical conductivity. Furthermore, it is relatively easy to get at a low price. Early graphite-based electrodes were usually made of graphite rods or plates (Fig. 9a) [164,165]. In 2010, a spectrographically pure graphite (SPG) rod was applied as a cathode in a microbial fuel cell (MFC) without any energy input to synthesize H<sub>2</sub>O<sub>2</sub> with a yield of 0.46 mg h<sup>-1</sup> and the CE of 69.5% [166]. 3D graphite particle electrodes (GPE) prepared via extrusion-spheronization method from graphite-polytetrafluoroethylene (PTFE) were also used in MFCs to generate H<sub>2</sub>O<sub>2</sub> [167]. Although anodic COD removal, electricity generation, and cathodic H<sub>2</sub>O<sub>2</sub> production were realized in one single system, H<sub>2</sub>O<sub>2</sub> yield was relatively low as 0.13 mg h<sup>-1</sup>. Acidic pretreatment on raw graphite powder promoted the surface area

and the OFGs content of GPE to increase the H<sub>2</sub>O<sub>2</sub> yield of MFC by 41% (0.19 mg h<sup>-1</sup>) [168]. Whereas the yield of H<sub>2</sub>O<sub>2</sub> in the MFCs was still sparse due to the relatively low current density provided by the bio-anode.

In the abiotic electrochemical system, the H<sub>2</sub>O<sub>2</sub> yield mostly depends on the performance of the cathode. Thus research efforts aimed to improve H<sub>2</sub>O<sub>2</sub> yield by modifying graphite electrodes.

Polymer-modified electrocatalysts are very promising materials for ORR [169]. Consider quinonoid compounds were often used to modify electrodes because they can stop the ORR at the peroxide stage [170,171]. Polypyrrole/anthraquinonedisulphonate (PPy/AQDS) composite film modified graphite produced H<sub>2</sub>O<sub>2</sub> with the yield of 4.2 mg h<sup>-1</sup> and CE of 64–73% at -0.65 V (vs. SCE) [172]. Quinonoid compounds were also employed to modify other kinds of carbon-based cathodes, and they will be discussed in the following chapters. In 2011, commercial MWCNTs (surface area 233 m<sup>2</sup> g<sup>-1</sup>, outer diameters 8–15 nm, inside diameters 3–5 nm) were immobilized onto graphite surface by Khataee and co-workers [173]. 1.4 mg h<sup>-1</sup> of H<sub>2</sub>O<sub>2</sub> was yielded while a CE of about 2.1% was achieved

at 100 mA. Conducting polymers, such as Ppy and polyaniline (PANI), are widely used as catalysts or catalyst supports for ORR due to their stability, ease of electro-polymerization, and high conductivity [174]. Rabl et al. [175] presented results that Ppy and PANI coating on carbon electrodes considerably improved the  $\text{H}_2\text{O}_2$  selectivity by preventing undesired side or further reactions of  $\text{H}_2\text{O}_2$  to  $\text{H}_2\text{O}$ . Based on the above properties, Ppy/MWCNT and PANI/MWCNT nanocomposites were fabricated and electro-polymerized onto the graphite electrode or stainless steel [176,177]. ORR activity of different concentrations of MWCNT was investigated. The PANI/MWCNT nanocomposite modified stainless steel cathode with MWCNT content of 2% (wt) generated  $1.1 \text{ mg h}^{-1}$  of  $\text{H}_2\text{O}_2$  with a CE of about 42% at  $-0.6 \text{ V}$  (vs. SCE), 2.5 times higher than raw stainless steel, which was due to the superior electrocatalytic activity of MWCNT. Meanwhile, 2.5% w/w Ppy/MWCNT had the highest ORR electrocatalytic activity and  $\text{H}_2\text{O}_2$  yield was increased by 70% to  $3.4 \text{ mg h}^{-1}$  at  $-0.55 \text{ V}$  (vs. SCE). Recently, Chu, et al. [178] fabricated multi-layer super-hydrophobic cathode by mixing graphite powder with CNT and PTFE. The hydrophobic property of carbon powder and heat treatment induced strong aerophily of cathodes, by which the cathode could adsorb more air bubbles under the air aeration than the hydrophilic cathode, and it exhibited an ideal performance for  $\text{H}_2\text{O}_2$  generation at  $37.6 \text{ mg h}^{-1}$  with an observed CE of 40% with 60 min of electrolysis.

$\text{H}_2\text{O}_2$  yield on graphite-based cathodes is not usually satisfactory because of the small surface area of graphite rods, plates, or particles. The graphite cathodes could only be used under very low current density in the early prototype design. Although modification led to a significant improvement in the performance of ORR, the  $\text{H}_2\text{O}_2$  yield and CE of graphite-based electrodes were still relatively low for application. Recently, 3D porous electrodes are becoming increasingly popular to counteract the low yield limitations of 2D electrodes in the electrochemical cells [179].

#### 6.1.2. Graphite felt based cathodes

Graphite felt (GF) or carbon felt (CF) are the most frequently used commercially available carbon materials. (GF is obtained from the graphitisation of the CF). As a typical 3D electrode (Fig. 9b), GF has excellent features such as good electrical conductivity ( $370.4 \text{ S m}^{-1}$ ) [180], high volumetric surface area ( $22,100\text{--}22,700 \text{ m}^2 \text{ m}^{-3}$ ), good mechanical integrity, high chemical resistance and stability, it is easy to fabricate and scale-up, and has a low cost [181]. It has been extensively used for  $\text{H}_2\text{O}_2$  production in the field of EAOPs for wastewater treatment.

Raw CFs (provided by Carbon-Lorraine Company) were applied as electrodes in EAOPs to electrogenerate  $\text{H}_2\text{O}_2$  and fabricate an electro-Fenton system to successfully degrade 2, 4-dichlorophenoxyacetic acid, *p*-Nitrophenol, pentachlorophenol, methyl parathion, malachite green, and phenol [182–187]. In early studies of EAOPs, pollutant degradation pathway and intermediates, optimal technical and economical degradation conditions, the kinetic mechanism of degradation were the major concern, rather than the performance of  $\text{H}_2\text{O}_2$  production. Nevertheless, as demand continues to increase, researchers are demanding higher performance of GF/CF based cathode, which gave rise to surface modification or coating techniques.

OFGs were verified to increase the hydrophilicity of carbon materials and thus promote the transfer of both electrons and dissolved oxygen [188]. Furthermore, OFGs or defects associated with OFGs are identified as two-electron reactive sites of carbon materials [115,118,161]. Therefore, increasing the number of OFGs on the electrode surface becomes the primary choice for electrode modification.

Zhou et al. [189,190] used hydrazine hydrate to increase O and N functional species content on the GF microfilaments surface. With

the stronger hydrophilicity and faster electron transportation of modified GF, the  $\text{H}_2\text{O}_2$  yield improved 160% to  $11.5 \text{ mg h}^{-1}$  with CE of 82% at  $-0.65 \text{ V}$  (vs. SCE). Ou et al. [191] successfully loaded O, N, and S-containing functional groups onto the GF by modification through the concentrated  $\text{H}_2\text{SO}_4$ ,  $\text{KMnO}_4$ , and  $\text{NH}_3$  activation. With better hydrophilicity and conductivity, the modified GF realized  $47.9 \text{ mg h}^{-1}$  of  $\text{H}_2\text{O}_2$  yield with CE of 11.8% at 640 mA, which was 73% higher than the raw GF. Wang et al. [192] activated GF with KOH at a high temperature ( $900^\circ\text{C}$ ) to harvest electrodes with higher surface area, higher hydrophilicity, and more OFGs for higher  $\text{H}_2\text{O}_2$  yield. The  $\text{H}_2\text{O}_2$  yield of activated GF reached  $40 \text{ mg L}^{-1} \text{ h}^{-1}$  (volume unknown) at  $-0.7 \text{ V}$  (vs. SCE). After activating the GF cathode, the apparent rate constant of dimethyl phthalate degradation in the electro-Fenton system increased from  $0.02 \text{ min}^{-1}$  to  $0.20 \text{ min}^{-1}$ . However, large amounts of energy were required due to the high temperature in this method. In 2020, Lai et al. [193] demonstrated GF cathodes treated with NaOH at a lower temperature ( $400^\circ\text{C}$ ) facilitated the OFGs loading and enhanced hydrophilicity. As a result, the modified GF realized about  $30 \text{ mg h}^{-1}$  of  $\text{H}_2\text{O}_2$  yield with CE of 94.6% at 50 mA. In order to develop simple methods to achieve large-scale modification, Jiang, et al. [194] investigated the  $\text{HNO}_3$  and KOH reagents treatment under a much milder temperature ( $70^\circ\text{C}$ ). Though both methods could increase the OFGs content, surface area, hydrophilicity, and  $\text{HNO}_3$  treated GF exhibited better performance to synthesis; resulting in  $742.5 \text{ mg h}^{-1}$  of  $\text{H}_2\text{O}_2$  at 20 V applied voltage, 8% and 69% higher than the KOH modified GF and unmodified GF, respectively. Acid pretreatment was also applied to activate GF via a low-cost and simple gaseous acetic acid activation [195]. The  $\text{H}_2\text{O}_2$  yield of activated GF is enhanced by 6 fold– $10.3 \text{ mg h}^{-1}$  with the CE of 75% at  $-0.7 \text{ V}$  (vs. SCE) due to higher contents of macropores, micropores,  $sp^3$  carbon bonds, defects, and OFGs.

Anodization was applied on GFs to increase the  $\text{H}_2\text{O}_2$  yield of electrochemical modified GFs by 170% due to the generation of carbonyl, carboxyl, quinone, and ester groups [196]. However, CE of anodized GF decreased from 87% to 79%, indicating the anodizing modification encouraged both two-electron ORR and four-electron ORR. Electrode polarity reversal was also applied for *situ* anodically modification of GF to improve the hydrophilicity of the electrode surface and  $\text{O}_2$  mass transfer [197]. With high contents of carbonyl and hydroxyl groups, the  $\text{H}_2\text{O}_2$  yield of GFs increased by 2.9 times, reaching  $8.1 \text{ mg h}^{-1}$  at 100 mA.

Comparing three oxidation modifications, Wang, et al. [198] discovered that the  $\text{H}_2\text{O}_2$  yield of electrochemically oxidized carbon fiber generated was  $9 \text{ mg h}^{-1}$ , 11.6 times that of raw CFs, and 16–98% higher than  $\text{H}_2\text{O}_2$  oxidized CFs and Fenton ( $\cdot\text{OH}$ ) oxidized CFs. However, after 10-rounds of continuous runs, the  $\text{H}_2\text{O}_2$  production of electrochemical modified GFs decreased by 42–61% due to the loss of  $\text{O}=\text{C}-\text{OH}$  species, and the destruction of the electrode structure. In the most recent research, the activity and selectivity of GF electrodes were improved for  $\text{H}_2\text{O}_2$  electrogeneration by integrating chemical oxidation, electrochemical oxidation, and thermal treatment [199]. It was reported that  $\text{HNO}_3$  oxidation facilitated OFGs and defects formation, while electrochemical oxidation favored carboxyl removal and carbonyl groups formation. Moreover, the following thermal treatment engendered the rebounded hydrophilicity and thus enhanced the activity. The modified electrode (GF– $\text{HNO}_3$ –EC– $\text{N}_2$ ) benefited from the above treatments, and exhibited a 5-fold higher  $\text{H}_2\text{O}_2$  yield,  $9 \text{ mg h}^{-1}$  with CE of 86% at 0 V (vs. RHE) than the pristine samples.

Highly active and selective materials were also applied onto GFs to improve the  $\text{H}_2\text{O}_2$  yield. For example, ZIF-8 was carbonized under a  $\text{N}_2$  atmosphere to load N-doped porous carbon onto the GF [200]. The existing graphitic-N and  $sp^2$  carbon promoted the electron transfer between catalyst surface and  $\text{O}_2$  molecules, as well as accelerating the

ORR. With optimal condition,  $\text{H}_2\text{O}_2$  yield increased 10 times and reached  $6 \text{ mg h}^{-1}$  with CE of about 9% at 100 mA. Another N-doped carbon modified GF prepared by electro-deposition of PANI, carbonization, and activation was applied in electro-Fenton to generate and activate  $\text{H}_2\text{O}_2$  to remove 85% of phenol in 180 min with a residual  $\text{H}_2\text{O}_2$  accumulation of  $4.6 \text{ mg h}^{-1}$  [201].

Vulcan XC-72R CB was deposited on GF to increase the surface area as well as the pore volume of the electrode. This modification improved the  $\text{H}_2\text{O}_2$  yield by about 10.7 times to reach  $\text{H}_2\text{O}_2 47.3 \text{ mg h}^{-1}$  with CE of 74.6% at 100 mA [202]. This was a milestone in developing a highly efficient modified GF electrode, because  $\text{H}_2\text{O}_2$  yield was improved to tens of  $\text{mg h}^{-1}$  at 100 mA with CE far more than 10%. Vertical-flow electro-Fenton reactor, peroxide-coagulation system, and flow-through electro-peroxone systems were developed based on this CB modified GF electrode to realize different wastewater treatment functions [203–205]. Most recently, an MWCNT & CB co-modified GF was fabricated [206]. Although the hydrophobicity was slightly increased (contact angle increased from  $145.2^\circ$  to  $154.9^\circ$ ), higher BET surface, pore volume, and OFGs content caused by modification still improved the ORR activity. As a result, a comparable  $\text{H}_2\text{O}_2$  yield of  $48 \text{ mg h}^{-1}$  with CE of 63% was obtained at 120 mA.

#### 6.1.3. Graphene decorated cathodes

In the past 7–8 years, graphene has been regarded as a promising material for  $\text{H}_2\text{O}_2$  electrogeneration. In 2016, Mousset et al. [207] tested three commercial pristine graphene materials (2D graphene monolayer, 2D graphene multilayer, and 3D graphene foam) as electrodes for  $\text{H}_2\text{O}_2$  generation. Although 3D graphene foam exhibited the least hydrophilicity, it could surprisingly achieve the highest  $\text{H}_2\text{O}_2$  generation,  $0.6 \text{ mg cm}^{-2}\text{cat}^{-3}$  at  $-0.61 \text{ V}$  (vs. Ag/AgCl), due to the contribution of higher surface area as well as superior electrical conductivity. However, compared with other carbon materials, the  $\text{H}_2\text{O}_2$  electrogeneration from graphene was not satisfactory, indicating that pristine graphene itself was not the preferred electrode for two-electron ORR. Graphene was mostly used for coating various substrates to improve the surface area and the conductivity of raw electrodes and thus increase the catalytic performance.

Le et al. [208] loaded homogeneous dispersion of GO onto the CF and investigated the effect of electrochemical, chemical, and thermal reduction of GO on the electrodes performance. The reduction of GO was beneficial to  $\text{H}_2\text{O}_2$  production because it enhanced hydrophilic characteristics and conductivity, as well as created more active sites. Though thermal reduction exhibited the highest electrochemical properties, electrochemical reduction had both high performance as well as low cost, which is regarded as the best modification method [209]. Analogously, GO was drop-casted onto a substrate disposed of liquid crystal display (LCD) glass, and then electrochemically reduced to form an ErGO-LCD electrode [210], which generated  $\text{H}_2\text{O}_2$  with the yield of  $2.3 \text{ mg h}^{-1}$  at  $-1.5 \text{ V}$  (vs. Ag/AgCl).

Encouraged by the above results, electrochemically exfoliated graphene (EEGr) was utilized as the functional coating material to decorate carbon cloth (CC) [211] and carbon-fiber brush [212]. After the optimization of EEGr and Nafion concentration, the EEGr decorated cathodes increased by 40–100% in  $\text{H}_2\text{O}_2$  yield, and 26.3–106% in phenol degradation rate in EF processes.

Quinone-functionalized electrochemically exfoliated graphene (QEEGr) was coated on the CC electrode to generate  $5 \text{ mg h}^{-1} \text{ H}_2\text{O}_2$ , which was 9 times higher than the unmodified CC [213]. The presence of the quinone group was thought to facilitate two-electron ORR, thus initiating  $\text{H}_2\text{O}_2$  generation without compromising the electrode electrical property. Moreover, QEEG- $\text{Fe}_3\text{O}_4$  coated CC composite electrode could continuously generate reactive oxygen species for complete degradation of Bisphenol A.

EEGr and Vulcan XC-72R CB co-modified GF cathode were

developed to generate  $38.5 \text{ mg h}^{-1}$  of  $\text{H}_2\text{O}_2$  at  $-0.9 \text{ V}$  (vs. SCE) in a neutral solution, which was 2 times that of the unmodified cathode [214]. N-doped graphene (N-EEGr) was derived by mixing the EEGr with ammonium nitrate followed by calcination under a  $\text{N}_2$  atmosphere to activate  $\text{H}_2\text{O}_2$  to  $\cdot\text{OH}$  for organics degradation, rather than increase the electrochemical generation of  $\text{H}_2\text{O}_2$  [215]. A significantly different result was obtained with another N-EEGr modified electrode by loading the mixture of CB,  $\text{N}_x$ -EEGr, and PTFE on the GF [216]. The  $\text{N}_x$ -EEGr was prepared by annealing of melamine and graphene mixture under a  $\text{N}_2$  atmosphere, where  $x$  represented the mass ratio of melamine to graphene. The optimized  $\text{N}_3$ -EEGr-CB-GF cathode improved  $\text{H}_2\text{O}_2$  yield to  $86 \text{ mg h}^{-1}$  due to the generated active graphite N and pyridinic N species and  $\text{C}=\text{C}$ . Moreover, the presence of pyridinic N was able to catalyze  $\text{H}_2\text{O}_2$  to produce  $\cdot\text{OH}$ , which is beneficial to overcoming the effect of the initial pH on EF [201,217].

#### 6.2. Reticulated vitreous carbon-based cathode

RVC is a disordered glassy porous carbonaceous material with a solid foam network structure (Fig. 9c). RVC has an exceptionally high surface area, high void volume, rigid structure, and low resistance to fluid flow [218]. These properties encouraged the applications of RVC in diverse areas such as sensors and monitors, chemical catalyst supports, and energy conversion [219]. Over the last 10 years, the corresponding research showed that the performance of RVC as cathodes for  $\text{H}_2\text{O}_2$  synthesis are comparable or even better relative to the GF electrode.

Coria et al. [220] investigated the mass transport of GF, RVC and boron-doped diamond (BDD) cathodes during two-electron ORR in a filter-press electrolyzer to discover that the performances of porous GF and RVC with higher limiting currents were obviously better than the non-porous BDD cathode. Petrucci et al. [221] confirmed that electrogeneration of  $\text{H}_2\text{O}_2$  on a RVC electrode was 210% and 60% higher than that of graphite and CF, respectively, under  $5 \text{ mA cm}^{-2}$ . This observation was due to the better oxygen diffusion and larger reactive surface from a porous 3D structure.

Recently a RVC electrode modified by anodic polarization was developed for drinking water disinfection. The  $\text{H}_2\text{O}_2$  yield was  $6.4 \text{ mg h}^{-1}$  with a CE of 43% at 24 mA, which was about 4 times of the unmodified RVC cathode [222]. The modification and application of RVC electrodes has gradually gained attention [223].

#### 6.3. Activated carbon-based cathodes

ACFs are considered as a group of advanced porous materials with a fiber shape and a well-defined porous structure (Fig. 9d) [224]. Except for the extremely large surface area ( $2000$ – $2500 \text{ m}^2 \text{ g}^{-1}$ ), the micropores of the ACFs are directly exposed to the surface, which reduces the mass transfer resistance and enhances the adsorption of various compounds. ACFs and their modification composites were extensively utilized in environmental remediation, such as the adsorption of organic and inorganic pollutants in water/air, capacitive deionization, the degradation of organic pollutants, and microbial decontamination [225]. However, only a few studies have focused on the catalytic production of  $\text{H}_2\text{O}_2$  from ACF.

Commercial ACF felt was utilized in an electro-Fenton system to degrade Acid Red 14 and levofloxacin [226,227]. Although almost 100% of Acid Red 14 or levofloxacin and 61–70% TOC were removed, the  $\text{H}_2\text{O}_2$  yield property of the ACF cathode was only about  $3.6 \text{ mg h}^{-1}$  at 500 mA with poor CE of 1.1% in the absence of  $\text{Fe}^{2+}$  during 180 min of electrolysis, which means most of the electricity was wasted. Similarly, a commercial ACF cathode was utilized in an electro-Fenton system for cationic red X-GRL degradation with a

maximum  $\text{H}_2\text{O}_2$  yield of  $4.8 \text{ mg h}^{-1}$  and CE of about 1% [228]. Zhang et al. [229] compared the electrocatalytic properties of two ACFs, which shared similar pore volumes as well as pore diameters but varied BET surface areas. Results showed that ACF with a higher surface area was correlated to faster  $\text{H}_2\text{O}_2$  and  $\cdot\text{OH}$  accumulation. However, the better ACF only had a  $\text{H}_2\text{O}_2$  yield of  $4.1 \text{ mg h}^{-1}$  and CE of about 1.8%.

In 2018, Zhou et al. [230] proposed an activated carbon-stainless steel mesh composite cathode (ACSS), which integrated  $\text{H}_2\text{O}_2$  electrogeneration and activation together with pollutants adsorption. Although  $\text{H}_2\text{O}_2$  yield was only  $1.9 \text{ mg h}^{-1}$  at  $100 \text{ mA}$  with a CE of 3%, the ACSS enabled the iron-free electro-Fenton feasible under neutral pH to remove 61.5% of reactive blue after 90 min. Ren et al. [231] successfully prepared a novel multilayer ACF-based composite cathode with rGO as the conducting layer and OMC as the oxygen diffusion channel. The electroactive surface area, oxygen diffusion rate and electron transport rate were all increased, and the  $\text{H}_2\text{O}_2$  yield of ACF@rGO@OMC electrode reached  $2.8 \text{ mg h}^{-1}$  with CE of 40.4% at  $-0.7 \text{ V}$  (vs. SCE).

In summary, on a few activated carbon-based cathodes have been employed for  $\text{H}_2\text{O}_2$  production and until its catalytic selectivity is substantially improved the potential for further applications will be limited [232].

## 7. Development of gas diffusion electrode

Generally, cathodes mentioned in the last chapter are immersed in the electrolyte. The gaseous  $\text{O}_2$  is dissolved into the electrolyte by aeration, and then the dissolved  $\text{O}_2$  diffuses with the electrolyte into the internal pores of the cathodes and reacts at active sites (Fig. 10b). However, the immersed cathodes are usually unable to maintain high  $\text{H}_2\text{O}_2$  yield and CE at large current densities (usually  $>10 \text{ mA cm}^{-2}$ ) because of the low solubility and inferior  $\text{O}_2$  mass transfer [164]. Lower CE of immersed cathodes results in the waste of the electricity and brings hidden safety trouble due to higher parasitic HER [233]. The birth of gas diffusion electrode (GDE) solved these challenges. As a kind of film electrode, GDE often consists of a reactive catalyst layer (CL), a gas diffusion layer (GDL), and an optional current collector. Applied for the electrogeneration of  $\text{H}_2\text{O}_2$ , the hydrophilic CL, which faces to the electrolyte, provides the reactive sites for the ORR, while the hydrophobic GDL facing to reactant gas provides a stable gas diffusion channel for the oxygen towards the catalyst layer and prevents electrolyte leakage. CLs are usually fabricated from the mixture of carbon-based catalyst powder and the binder, followed by being coated/rolled/painted/sprayed onto the gas diffusion layer. Based on the species of the main catalyst in the CL, the GDE can be sorted into carbon black-based-, carbon nanotube-based- and hybrid carbon GDE.

### 7.1. Carbon black-based GDE

The most widely utilized carbon materials for GL preparation are the Vulcan XC-72(R) and Printex L6 CB. GDE has been developed by E-TEK by painting Vulcan XC-72 CB and PTFE wet paste mixture uniformly onto a face of the carbon cloth. The  $\text{H}_2\text{O}_2$  yield of Vulcan XC-72 CB-based GDE was  $82.7 \text{ mg h}^{-1}$  with CE of about 29% at  $450 \text{ mA}$ . Based on this electrode, several different EAOP systems were developed, and numerous target POPs were successfully degraded [18,234–240]. Although the advent of GDE substantially altered the mass transfer of  $\text{O}_2$ , there is still much room for CE further improvement by promoting the CL catalytic activity and selectivity. Developing from Vulcan XC-72R CB and PTFE via a rolling method, the harvested GDE produced  $158 \text{ mg h}^{-1} \text{ H}_2\text{O}_2$  at  $520 \text{ mA}$  with CE of 48%. Unlike traditional GDE, the CL of the electrode simultaneously acted as a GDL [241]. The GDE was also

prepared by pressing and sintering a series of metal oxide modified Vulcan XC-72R CB mentioned in Chapter 4.3.2. With 0.2 bar pressurized pure  $\text{O}_2$  supply,  $\text{H}_2\text{O}_2$  yield of W@Au/CB GDE, CeO<sub>2</sub>/CB GDE and MnO<sub>2</sub>/CB GDE were 21, 51, and  $68 \text{ mg h}^{-1}$  at  $-1.1 \text{ V}$  (vs. Ag/AgCl) [141,145,147]. Meanwhile,  $102 \text{ mg h}^{-1}$  of  $\text{H}_2\text{O}_2$  was generated from WO<sub>2.72</sub>/CB GDE at  $-1.3 \text{ V}$  [144], and  $102 \text{ mg h}^{-1}$  of  $\text{H}_2\text{O}_2$  was generated from V<sub>2</sub>O<sub>5</sub>/CB GDE at  $-1.5 \text{ V}$  [142]. Nevertheless, CE was not calculated or mentioned in those studies, which makes it hard to compare those GDE with others' intuitively.

Compared to Vulcan XC-72 CB, Printex L6 CB was demonstrated to be a better choice for  $\text{H}_2\text{O}_2$  generation due to more oxygenated acid species content and higher hydrophilicity [242–244]. When the aforementioned 5% Ta<sub>2</sub>O<sub>5</sub>/CB material was made into GDE, the  $\text{H}_2\text{O}_2$  yield was  $11 \text{ mg h}^{-1}$  at  $-1.0 \text{ V}$  (vs. Ag/AgCl) [148]. As quinones have been investigated as efficient catalysts for the improvement of two-electron ORR [245], GDEs were developed by modifying CB with different amounts of tert-butyl-anthraquinone (TBAQ) [246]. According to RRDE results, 1% TBAQ/CB showed the highest selectivity (89.6% with 2.2 electrons exchanged). The obtained GDE realized a  $\text{H}_2\text{O}_2$  yield of  $80 \text{ mg h}^{-1}$  at  $-1 \text{ V}$  (vs. SCE). Rocha et al. [171] investigated the electro-activity of various quinone compounds (acenaphthoquinone (APQ; acenaphthylene-1,2-dione), menadione (MDA; 2-Methyl-1,4-naphthoquinone), and Alizarin Red S (ALZ; 1,2-dihydroxyanthraquinone)) modified CB for  $\text{H}_2\text{O}_2$  production in an acid medium. The results showed that 1% of 1,2-dihydroxyanthraquinone was efficient for two-electron ORR and the resultant GDE realized a  $\text{H}_2\text{O}_2$  yield of  $77.1 \text{ mg h}^{-1}$  at  $1900 \text{ mA}$  (CE = 6.4%), which was 116% higher than the unmodified CB GDE.

### 7.2. Carbon nanotube based GDE

In 2009, Zarei et al. [247] developed CNT-based GDE by bonding the ointment mixture of commercial MWCNT and PTFE to 50% PTFE-loaded carbon papers and calcined at  $350 \text{ }^\circ\text{C}$  under  $\text{N}_2$  atmosphere.  $\text{H}_2\text{O}_2$  yield was  $24 \text{ mg h}^{-1}$  with CE of about 38% at  $100 \text{ mA}$ . The prepared GDE was utilized for C.I. Basic Yellow 2 removal via peroxy-coagulation, as well as C.I. Basic Red 46 degradation through the oxalate catalyzed photo-electro-Fenton [248,249].

During the synthesis of modified GDE, the carbon materials also serve as a template or a platform that will disperse or adsorb the modifying reagents. The subsequent heat/hydrothermal treatment caused a uniform distribution of active sites associated with modified moieties. Therefore, the impact of carbon supports was different. Considering the contribution of quinone compounds toward two-electron ORR, Lu, et al. [250] investigated the ORR activity of different TBAQ modified carbon materials (carbon aerogel, CNT, CB, graphene doped CB) to discover the TBAQ modified CNT exhibited the highest  $\text{H}_2\text{O}_2$  yield ( $30.1 \text{ mg h}^{-1}$  at  $50 \text{ mA}$ ), which was 27% higher than the unmodified CNT GDE and 9–56.4% higher than other TBAQ modified carbon GDEs. The characterization results showed more C–C  $sp^3$  carbon, and OFGs content together with the mesoporous structure resulting in the outstanding performance of the TBAQ modified CNT GDEs.

According to the former results in Chapter 4, Co-based catalysts in the form of Co oxides, Co chalcogenides, or Co nanoparticles are the most efficient electrocatalysts for enhancing two-electron ORR in the acidic medium [133,251–253]. The spraying of CoS<sub>2</sub>-MWCNTs was employed to manufacture GDE [254]. In the galvanostatic test, the  $\text{H}_2\text{O}_2$  yield of CoS<sub>2</sub>-MWCNTs GDE reached  $95 \text{ mg h}^{-1}$  with CE of about 50%. CoS<sub>2</sub> particles were proven to play a significant role in enhancing the two-electron ORR as well as preventing  $\text{H}_2\text{O}_2$  from further reduction to  $\text{H}_2\text{O}$  to some extent. Enlightened by the above research, (Co, S, P)-decorated MWCNTs were prepared through a hydrothermal route [255]. The

electrocatalyst was mixed with 2-propanol and Nafion. The mixture ink was sprayed onto a carbon cloth several times together with a carbon microporous layer to form the GDE. Compared with undecorated MWCNT GDE, (Co, S, P)-decorated MWCNTs GDE enhance the electrocatalytic  $\text{H}_2\text{O}_2$  production to about  $225 \text{ mg h}^{-1}$  with CE of 51–53% at 800 mA.

Recently, GDE was fabricated by rolling, pressing, and calcining the mixture of P-doped CNTs and PTFE [256]. The successful doping of P increased the activity of CNT, which exhibited about 0.2 V more positive onset potential and 100% higher current density at  $-0.8 \text{ V}$  (vs. SCE). However, P-doping decreased the selectivity of two-electron ORR with  $n$  changing from 2.6 (CNTs) to 3.06 (P-CNTs). Although P-CNTs tended to four-electron pathway, the P-CNTs GDE still had excellent performance with a  $\text{H}_2\text{O}_2$  yield of  $207 \text{ mg h}^{-1}$  and CE of 88.5%, which was obviously higher than CNTs-GDE ( $67 \text{ mg h}^{-1}$  with CE of 64.7%). This result demonstrated the difference between the RRDE calculated selectivity and electrolysis calculated CE, which in fact was the difference between the theoretic selectivity of the material and the actual selectivity of the electrode in operation.

### 7.3. Hybrid carbon GDE

Recently, researchers began to take advantage of the structural and physical properties of different carbon materials and started to investigate the mixture of different carbon materials as a catalyst. Carbon composite materials containing at least two kinds of carbons were reviewed in this section.

Xu et al. [257] investigated the performance of graphite-PTFE GDE and rGO & graphite-PTFE GDE to discover  $\text{H}_2\text{O}_2$  yield of rGO & graphite-PTFE GDE ( $12.5 \text{ mg h}^{-1}$  with CE of about 40% at 24 mA) was nearly four times higher relative to graphite-PTFE GDE, due to the addition of rGO improved electrochemical conductivity and mesopores contents [258].

Typically, rGO aggregation is an overlooked issue during the fabrication of electrodes. Because of the strong hydrophobic interactions between nano-sheets, rGO can aggregate easily in solution or in the drying process [115,259], which substantially reduces the accessibility of the reactants toward rGO basal planes on the electrodes [118]. CNTs stacked between rGO nano-sheets prevent the rGO from restacking to increase basal space and bridge the defects to enhance the electrical conductivity [260]. Liu et al. [261] fabricated a novel N-rGO & CNT-PTFE GDE by doping N atoms in the rGO & CNT composite. RRDE results showed that the onset potential of N-rGO & CNT shifted positively in the range of 146–363 mV with reference to bare rGO, CNT, and graphite. Moreover, N-rGO & CNT-PTFE GDE generated  $1 \text{ mg h}^{-1}$   $\text{H}_2\text{O}_2$  at a relatively positive potential ( $-0.2 \text{ V}$  vs. SCE), which was 2–10 times higher than the reference GDEs.

Chen et al. [262] reported that trace MWCNTs could construct “electron-bridges” interconnecting the CB particles and thus increase the conductivity and porosity of CB. Therefore  $\text{H}_2\text{O}_2$  yield of CB & MWCNT-PTFE GDE was  $41.3 \text{ mg h}^{-1}$  with a high CE of 65.1% at 100 mA. However, once poorly conductive AC embedding into the hybrid material, the CB particles would be huddled to some scattered aggregates to destroy the bridges, resulting in poor porous structure and conductivity. Furthermore,  $\text{H}_2\text{O}_2$  is prone to be further reduced to  $\text{H}_2\text{O}$  with the presence of AC.

Zhu et al. [263] mixed graphite powder with g-C<sub>3</sub>N<sub>4</sub> to fabricated g-C<sub>3</sub>N<sub>4</sub>@GDE via the rolling method. Characterization results showed that hydrophilicity could be increased by a g-C<sub>3</sub>N<sub>4</sub> modification, which could induce fast electrolyte penetration to the cathode surface. With moderate g-C<sub>3</sub>N<sub>4</sub> mixing, g-C<sub>3</sub>N<sub>4</sub>@GDE generated the highest  $\text{H}_2\text{O}_2$  ( $457.5 \mu\text{M}$ ) compared with pure graphite GDE ( $328.2 \mu\text{M}$ ) and pure g-C<sub>3</sub>N<sub>4</sub> GDE ( $302.2 \mu\text{M}$ ).

In summary, multiple GDEs based on newly designed high-performance catalysts were developed, which could realize maximum  $\text{H}_2\text{O}_2$  yield in the case of the excellent three-phase interface provided by GDE. Nevertheless, some technical issues remain, which require special attention, such as flooding issues caused by improper water management [264]. When the porous GDE was supersaturated, the electrolyte hindered the ability of oxygen to diffuse towards the active sites and thus destroyed the three-phase interfaces (TPIs) equilibrium and decreased the electrode performance. Characterizing, measuring, and solving flooding issues are still challenges for both two-electron and four-electron reactions [265,266].

## 8. Recent development of air self-diffusion electrode

Compared with the immersed electrode, GDE greatly improved the utilization rate of oxygen during  $\text{H}_2\text{O}_2$  production relative to the CE of the electrode [164]. However, the aforementioned GDE always needs pressurized air or pure oxygen gas, which increases the construction cost, reactor complexity, and safety. In order to reduce costs, while ensuring the satisfied cathodic performance in engineering applications, a novel sandwich-like air self-diffusion cathode manufactured via rolling method was developed by our group in 2015 [267], which was a deformation and expansion of our formerly developed AC-PTFE air cathodes for four-electron ORR [268–272]. Instead of expensive and multistep-prepared CNTs, OMC or graphene, commercial carbon powder Vulcan XC-72R CB and graphite were used to fabricate CL. The mixture of carbon powders and PTFE was rolled onto a stainless steel mesh (SSM), while the CB-PTFE breathable waterproof GDL was rolled onto the other side. This air self-diffusion cathode is a practical design where oxygen in the air can actively diffuse through GDL to the internal interface of the CL, which needs no aeration or pressurized gas to generate  $\text{H}_2\text{O}_2$ . In order to distinguish our air cathode from GDE, the former is named “air-breathing cathode” (ABC).

During the exploration of different proportions of CB and graphite in CL, it was found the pore area and volume of pure CB-PTFE electrode were 11.6 and 4 times of those of pure graphite-PTFE electrode, but the pore diameter of the former was only 31.6% of the latter. Both electrodes exhibited poor performance in electrogenerating  $\text{H}_2\text{O}_2$  due to the indirect four-electron reaction or lack of active sites [267]. When two kinds of carbon materials were mixed together, the hybrid carbon-PTFE CL had moderate pore diameter, area, and volume. With the optimal mass ratio of CB to graphite (1:5),  $\text{H}_2\text{O}_2$  yield reached  $50 \text{ mg h}^{-1}$  (with CE of 92%) in an electrolysis cell at 86 mA. Aimed at improving the two-electron ORR activity for efficient  $\text{H}_2\text{O}_2$  generation, Zhao et al. tuned catalyst mesostructure and hydrophilicity/hydrophobicity by adjusting PTFE content in CB & graphite-PTFE CL and avoiding calcination under atmospheric conditions [273,274]. It was found that the electroactive area was more relevant to the specific surface area of the 3–10 nm mesopores rather than the total BET surface area, and the electroactive area decreased from  $41 \text{ cm}^2 \text{ g}_{\text{cat}}^{-1}$  to  $19 \text{ cm}^2 \text{ g}_{\text{cat}}^{-1}$  with PTFE increased from 0.57 g to 4.56 g. Higher PTFE content led to an excessive supply of  $\text{H}^+$  and induced the  $\text{H}_2\text{O}_2$  decomposition and decreased the hydrophilicity to limit the amount of  $\text{O}_2$  diffused to catalytic sites. The ABC PTFE<sub>0.57</sub> with the lowest PTFE content exhibited super-hydrophobic, highest  $\text{H}_2\text{O}_2$  yield of  $74.6 \text{ mg h}^{-1}$ , and highest CE of 84% at 140 mA.

These researchers emphasized the balance among the pore diameter, specific area, and volume, as well as the balance between hydrophilicity and hydrophobicity. In former studies, people devoted themselves to increasing the surface area together with the hydrophilicity of the electrode by numerous treatments

[192,197,208,214,275]. However, conflicting results were obtained in our research. Compared with the coating or sparging method, the rolling method was an advanced method for catalyst layer fabrication because it could load more active sites onto the unit area [233]. On the one hand, higher active sites density improves the activity of the cathode. On the other hand, excessive active sites would further reduce H<sub>2</sub>O<sub>2</sub> in the porous rolling cathode. Dissimilar to the immersed electrodes, our rolling ABC mainly utilized the O<sub>2</sub> from the air rather than the dissolved O<sub>2</sub> in the electrolyte by aeration. Consider the two-electron ORR need electron, proton, and O<sub>2</sub> as reactants, and each of those is from solid, liquid, air, respectively, the solid-liquid-air three-phase equilibrium inside the porous catalyst layer is critical to the high performance of the electrode. Excessive pursuit of hydrophilicity in the cathode would induce the three-phase interfaces out of balance and engender the decrease of H<sub>2</sub>O<sub>2</sub> production. Recently, the hydrophobicity property of the electrode has attracted a growing number of research, and H<sub>2</sub>O<sub>2</sub> yield, as well as stability of the newly developed hydrophobic/super-hydrophobic/super-aerophilic electrode, have been significantly improved [276–278]. Some scholars also preferred to use more hydrophobic materials as substrates for GDE [124].

Based on our optimized highly efficient ABC, multiple electrochemical systems have been built for various wastewater (cyanobacterial boom water [279], formaldehyde-containing wastewater [280], phenolic wastewater [163], antiviral drug-containing wastewater [281]) treatments as well as sterilization and disinfection [274]. In conclusion, our series of research demonstrated highly efficient production of H<sub>2</sub>O<sub>2</sub> via two-electron ORR can be realized by rolling hybrid carbon cathodes without using noble metals or other complex chemical promoters. The cheap commercial raw carbon materials combined with an easy manufacturing process makes the rolling ABC potential for large-scale application of in situ electrosynthesis of H<sub>2</sub>O<sub>2</sub>.

In recent years, the active gas diffusion electrode has attracted growing attention, and multiple electrodes were developed with various names. rGO@graphite-based air diffusion cathode (rGO@-GADC) was applied in an electro-UV/H<sub>2</sub>O<sub>2</sub> system for penicillin sodium degradation to remove 91.1% of penicillin sodium with 56.8% of mineralization current efficiency [282]. A novel “floating cathode” with half submerged inside the electrolyte synergistic utilized gaseous O<sub>2</sub> from ambient air and the dissolved O<sub>2</sub> in the electrolyte. With the formation of TPIs, the optimized floating GF electrode realized a H<sub>2</sub>O<sub>2</sub> yield of 13.3 mg h<sup>-1</sup> with CE of 21% at 100 mA, which was 4.3 times of the submerged GF electrode [283]. A super-hydrophobic natural air diffusion electrode (NADE) was developed by coating CB onto CF followed by calcination. After the catalyst loading optimization, H<sub>2</sub>O<sub>2</sub> yield reached 518.5 mg h<sup>-1</sup> with CE of 66.8% at 1200 mA [277,284]. In the catalysis materials fabrication field, researchers are also beginning to use self-diffusing substrates for material modifications to reduce electrode complexity [285,286].

## 9. Summary and conclusion

### 9.1. Difficulty and challenge

The electrosynthesis of H<sub>2</sub>O<sub>2</sub> via two-electron ORR provides an alternative to the mature AO process or the emerging direct synthesis and photo-catalysis. The increased usage and decreased cost of renewable electricity will transform the chemicals industry. However, current developments of the cathode are still limited by at least four major challenges, including designing catalyst materials with high activity and selectivity, establishing theoretical calculation models closer to the actual experiments, fabricating

materials and electrodes by simple and low-cost methods, maintaining stability over the long-term operation.

#### 1) Designing catalyst materials with high activity and selectivity

Two major challenges, namely improving activity and selectivity, need to be addressed before carbon-based electrocatalysts can compete with the current state-of-the-art. There is plenty of scope for the improvement of pristine catalyst materials via changing the substrate composition, architecture & defects, and surface property. However, the catalysis mechanism and critical active sites for ORR on carbonaceous electrocatalyst are still confusing and controversial [138,287]. There are remaining debates and discrepancies on the intrinsic properties of the catalytic sites, the effect of heteroatom/functional groups/defect, micro/mesoporous, hydrophilic/hydrophobic nature of the materials to the selectivity to the two-electron ORR process. This ambiguity in determining the true nature of two-electron ORR active sites in those carbon-based catalysts hinders the development of efficient catalysts. The current cutting-edge research is to identify the influence of a single factor on ORR catalytic activity and selectivity. Further development is still primarily based on trial-and-error approaches until now [288], and it is still difficult to realize the controllable synthesis of various defective or doping carbon materials. Meanwhile, new mechanisms are emerging continuously: In contrast to the ordinary ad-O<sub>2</sub> mechanism, Chai, et al. [39] found O<sub>2</sub> adsorption is not required in the new mechanism. Instead, the H atom on carbon catalyst is abstracted by O<sub>2</sub> molecule to generate either a HO<sub>2</sub><sup>-</sup> ion or a HO<sub>2</sub><sup>·</sup> radical and thus generate H<sub>2</sub>O<sub>2</sub>.

#### 2) Establish a theoretical calculation model closer to the actual experiments

In most studies, researchers have reported to successfully develop ideal two-electron ORR catalysts based on the RRDE or RDE results when the electron transfer numbers of catalysts were close to 2. However, there is a significant leap from pure material testing to realistic electrode operation that is needed. The (R)RDE measurements are in O<sub>2</sub> saturated, high electrolyte content solution together with almost unlimited mass transfer. These idealized systems only provide an upper boundary to the CE to H<sub>2</sub>O<sub>2</sub> at most, while practical equipment tends to underperform. On the one hand, the internal channels and pore structures of the final fabricated electrode are relatively different from those of a pure carbon material or testing modes on the (R)RDE. On the other hand, even with pure O<sub>2</sub> aeration and magnetic stirring, the O<sub>2</sub> supply and mass transfer in 100–1000 mL level real reactors cannot compare with the conditions of RRDE. At this point, the reference value of the DFT model and (R)RDE results decrease. Such phenomena require modeling experiments in order to predict or represent the real equipment conditions more accurately.

#### 3) Fabricate materials & electrodes by simple and low-cost methods

It should be noted that catalytic activity and the selectivity of novel catalysts have only exhibited a marginal increase while the preparation methods become more intricate, making the materials deviate from the target of more cost effective approaches. For many of the aforementioned high-performance catalysts, it is reported that a lower catalysts loading engenders the active sites sparse distribution, which decreases the probability of H<sub>2</sub>O<sub>2</sub> further reduction. The selectivity toward H<sub>2</sub>O<sub>2</sub> increases while decreasing the loading amount [87,93]. Typically, catalyst loading density on

the RRDE was controlled at one hundred  $\mu\text{g cm}^{-2}$  level. Considering the mass transfer limitations in practical devices, catalyst loading density on the real electrode should be lower to keep high selectivity. This calls for the highly precise electrode fabrication method.

In the future development, a simple fabrication method with low costs should be another critical criterion in designing catalysts and fabricating electrodes.

#### 4) Maintaining stability over the long-term operation

Except for catalytic activity and selectivity, the practical value of any material or electrode also relies on its long-term stability. Wang et al. [198] found the performance of the OFGs modified cathode was reduced after 10-times continuous runs, which was ascribed to the cathode structure destruction and OFGs content decrease due to the  $\text{H}_2\text{O}_2$  oxidation. This illustrated the poor stability of the cathode in the long-term operation [289]. Meanwhile, the stability tests in most previous research are far from enough. Presently, researchers often document the stability of new fabricated electrodes by showing negligible changes in current response or  $\text{H}_2\text{O}_2$  yield after 5–20 h of operation [87,101,102,118,196]. These are not convincing results to obtain a stable performance conclusion. Active materials should not be proven stable until they are subjected to more rigorous electrosynthesis trials conducted over hundreds or even thousands of hours. In the most recent research, Cao, et al. [290] presented a highly hydrophobic architecture GDE consisting of densely distributed N-doped carbon nano-polyhedra, thus enabling the 200 h durable electrolysis at  $100 \text{ mA cm}^{-2}$ . Li et al. [291] evaluated the feasibility of electrochemical  $\text{H}_2\text{O}_2$  production with CB-PTFE GDE. The results showed that the GDE could maintain high CE (>85%) as well as low energy consumption (<10 kWh per kg  $\text{H}_2\text{O}_2$ ) for about 1000 h. This research suggests that electrochemical  $\text{H}_2\text{O}_2$  production with GDE holds great promise for the development of compact treatment technologies. In the following exploratory research, the long-term stability and decay mechanism of materials, as well as electrodes in the EAOP systems, also need special attention. In our recent research [163], although the rolling ABC showed good stability under the condition of generating  $\text{H}_2\text{O}_2$  ( $\text{H}_2\text{O}_2$  yield decreased 17.8% after 200 h of operation), the electrodes decayed obviously when operated in the EAOP systems. It was found salt precipitation occurred due to the local alkalization and enrichment of  $\text{Na}^+$ , which would cause the block of the active sites and mass transfer channels. Meanwhile, the  $\cdot\text{OH}$  generated in the EAOP system would cause damage to the carbonaceous electrode by adding defects and oxygen-containing functional groups onto the electrode during the non-selective oxidation. Four electrode performance decay factors were illustrated during the synthetic phenol wastewater degradation. For actual wastewater treatment, the operating life of the cathode in such conditions will only be shorter because the components of sewage are more complex and diverse. Thus, lifetime experiments under different conditions with longer testing times are suggested to analyze the correlations of physicochemical properties and catalyst/electrode performance decay. When the decay mechanism of the electrode performance in long-term operation is clear and definite, it can further guide the development and upgrading of the new long-life electrodes [292,293].

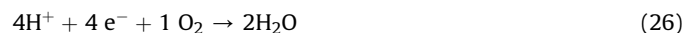
#### 9.2. Future and outlook

The development of carbon-based materials should be combined with theoretical studies, regarded as a requisite aid for catalysts designed or electrode modification to tune ORR selectivity to  $\text{H}_2\text{O}_2$ . In particular, the models which can better reflect the performance of catalysts in realistic devices will be more popular. To

achieve these ends, further studies of the fundamental principles is needed to fully understand the origin of activity enhancement.

Although multiple theoretical simulations and physicochemical techniques have been applied to reveal the catalytic mechanism of various carbonaceous materials, it's still hard to distinguish the nature of active sites of two-electron & four-electron ORR at the current technology state. More advanced characterization techniques and sophisticated experimental design are needed to distinguish the active sites for two-electron and four-electron pathways. Pinpointing such sites or chemical motifs would have guiding significance for both two-electron and four-electron carbon-based catalyst designs in the future. Once the two-electron active sites are determined, these sites could be purposefully increased to enable more efficient two-electron ORR or be eliminated from catalysts where four-electron ORR is required.

The ORR needs  $\text{O}_2$ , protons and electrons with mole ratio of 1:4:4 (four-electron pathway) or 1:2:2 (two-electron pathway) as reactants, from liquid, gas, and electrode, respectively. The active sites that stay in liquid-gas-solid TPIs could efficiently catalyze the ORR [233,294,295]. The accessibility of the active sites to  $\text{O}_2$  molecules is critical, but usually deficient due to the low  $\text{O}_2$  solubility in the realistic aqueous solution. Therefore, series electrodes styles, such as 3D particle electrodes [167], "floating" electrodes [283,296], and GDE, were invented to optimize the catalytic interface. Recently, scholars tried to accelerate the gas diffusion or tune water distribution to create more adequate TPIs inside the porous electrodes by porosity control and microarchitecture engineering. Therefore, superaerophilic CNT-array electrodes [294], super-wetting electrodes [297], and breathing-mimicking electrodes [298] were invented to improve four-electron ORR activity. It could be observed from Eqs. (26) and (27) that the  $\text{O}_2$  demand of a two-electron pathway is twice that for a four-electron reaction at the same Faraday electron flux and proton supply, which means  $\text{O}_2$  supply is more vital. More simple surface/structure engineering techniques need to be developed in the future to enhance overall catalytic performances in  $\text{H}_2\text{O}_2$  production.



Process optimization and cost-efficiency are at the core of a suitable treatment strategy [299]. From the engineering perspective, reducing the cost to an acceptable level is a prerequisite for the application of this technology. According to Yang et al.'s calculation [12], the total costs per mole of  $\text{H}_2\text{O}_2$  ( $C_{\text{total}}$ ) via two-electron ORR can be calculated and expressed as the sum of two parameters, electricity costs ( $C_{\text{electricity}}$ ) and cathode costs ( $C_{\text{cathode}}$ ) (Eq. (28))

$$\begin{aligned} C_{\text{total}} &= C_{\text{electricity}} + C_{\text{cathode}} \\ &= p_{\text{electricity}} UIt + p_{\text{cathode}} S \\ &= p_{\text{electricity}} UnF/\lambda_{FE} + p_{\text{cathode}} nF/jt\lambda_{FE} \end{aligned} \quad (28)$$

Where,  $p_{\text{electricity}}$  represents the cost per unit energy of electricity ( $\$/\text{J}^{-1}$ ),  $U$  stands for the cell potential (V),  $n = 2$ , which represents the electrons transfer number for generating  $\text{H}_2\text{O}_2$ ,  $F$  stands for Faraday constant ( $96486 \text{ C mol}^{-1}$ ), and  $\lambda_{FE}$  is the Faradaic current efficiency. Meanwhile,  $p_{\text{cathode}}$  is the capital cost per unit cathode area ( $\$/\text{cm}^{-2}$ ),  $j$  represents the current density ( $\text{A cm}^{-2}$ ), and  $t$  is the total operating time of the cathode over its lifetime (s). As  $\lambda_{FE}$  stands for the denominator for electricity costs as well as cathode costs, it is clear that high CE plays a significant role in the performance of the electrode as well as the economic efficacy of the process.

Meanwhile, in the cathode costs part, decreasing the numerator  $p_{\text{cathode}}$  and increasing cathode lifetime  $t$  can also reduce the overall cost of the  $\text{H}_2\text{O}_2$  synthesis, which highlights the relevance of costs of raw materials and preparation process together with electrode stability.

Except for stability [163], longer-term goals for  $\text{H}_2\text{O}_2$  electro-synthesis should focus on scalability: moving from benchtop experiments to syntheses on pilot or even industrially relevant scales [29]. Rapid  $\text{H}_2\text{O}_2$  accumulation to desired concentration in large volume aqueous solution is the prerequisite of up-scaling [233]. Therefore, a more realistic aim would be to increase the current density on the electrodes in the  $\text{H}_2\text{O}_2$  electrosynthesis without lowering selectivity. This would improve the synthesis efficiency and decrease the costs (Eq. (26)). Traditional carbon electrodes such as graphite rod/plate/particle, GF, and ACF are inefficient for  $\text{H}_2\text{O}_2$  production in bi-dimensional configurations due to the limited dissolved  $\text{O}_2$  mass transfer in water [300]. In the presently available literature, most studies focus on selectivity on the premise of neglecting the current density. For those electrodes that can only withstand low current density, they have to be fabricated bigger and bigger to increase  $\text{H}_2\text{O}_2$  production at higher current flux, which makes them impractical for applications. Recently, multiple GDEs have been reported for faster  $\text{H}_2\text{O}_2$  productions with high current efficiencies. These GDEs could maintain the current efficiency over 70% at current densities  $>25 \text{ mA cm}^{-2}$  [301–304]. Based on these electrodes, numerous contaminations were degraded in EAOP systems at pilot/pre-pilot plant scale (2.5–100 L). Developing electrodes with efficient  $\text{H}_2\text{O}_2$  production at large current flux is the inevitable trend in the future. Until now, the largest air cathode so far came from Zhang et al. [305]. A 707  $\text{cm}^2$  air cathode was utilized in a 3 L EF reactor for efficient Rhodamine B degradation. The shape and operating conditions of film air cathode determine that it cannot be enlarged without limit. As a result, new electrode and auxiliary equipment structures need to be developed to accommodate modular assembly. Reactors applied for EAOP treatments of wastewater are also needed to be well developed to fulfill the optimum properties of the electrodes [306]. More effort should be dedicated to other aspects such as equipment, scale-up, engineering, and economic issues in applying EAOP technologies to real wastewaters at an industrial scale [300].

The various applications of aqueous  $\text{H}_2\text{O}_2$  will require a certain  $\text{H}_2\text{O}_2$  concentration and may only tolerate a certain pH range [29]. According to RRDE & RDE measurements shown in Tables 1 and 2, all the catalysts showed higher  $\text{O}_2$  reduction activity in alkaline media than in acid media. However, they were also less selective toward  $\text{H}_2\text{O}_2$ . In the practical application of  $\text{H}_2\text{O}_2$ , wastewater treated by AOPs is often in acid media, while pulp and paper bleaching is usually in an alkaline environment. Here it is recommended that researchers could first focus their efforts on  $\text{H}_2\text{O}_2$  electrogenerating under acid conditions: AOP treatments only need 0.1% (wt) content of  $\text{H}_2\text{O}_2$ , which is two orders of magnitude below the demand for bleaching, making the application relatively easier. Moreover, Proton conducting polymeric membranes are much more technologically mature and cheaper than hydroxide conducting counterparts [307].

### 9.3. Guidance and suggestions

In our review, there are multiple differences in systems, method, expression and, calculations, which make comparisons among the different research difficult. We suggest the following studies can use more unified experimental methods and expressions while avoiding mistakes described below.

- 1) System: in the electrogeneration of  $\text{H}_2\text{O}_2$  experiments or (R)RDE tests, except for pH value, different types and concentrations of electrolyte were used. Until now, the most commonly used electrolyte in the electrolysis is 50 mM  $\text{Na}_2\text{SO}_4$  with a pH of 3 or 7, while  $\text{O}_2$  saturated 100 mM KOH or 500 mM  $\text{H}_2\text{SO}_4$  electrolyte is often employed in the (R)RDE tests.
- 2) Method: in general, the cathodic electrogeneration of  $\text{H}_2\text{O}_2$  was conducted through galvanostatic mode in a two-electrode system connecting to a DC power or via chronoamperometry at constant potentials in a three-electrode system powered by a potentiostat. We found that a slight change in the distance between the reference electrode and the working electrode would dramatically change in  $\text{H}_2\text{O}_2$  yield. Therefore, it is not easy to transversely compare the  $\text{H}_2\text{O}_2$  yield at chronoamperometry because the researchers did not specify the distance between the electrodes. Moreover, as shown in Table 3, CE of electrodes operated in chronoamperometry mode are usually unknown and even cannot be calculated by us due to the unpublished current flux. Considering the three-electrode system has many disadvantages, including the high cost of the equipment and the fuzzy parameters in the practical water treatment processes, the electrogeneration of  $\text{H}_2\text{O}_2$  through galvanostatic mode in a two-electrode system is recommended in future investigations. As summarized in Tables 1 and 2, in the RDE and RRDE tests, some parameters like onset potential, the definition of onset potential, and the potential range of calculated  $n$  were not given by authors. This would also bring troubles for readers, which should be avoided in the future.
- 3) Expression: various expressions were utilized to describe the  $\text{H}_2\text{O}_2$  yield in different studies, including  $\text{mg L}^{-1} \text{ h}^{-1}$ ,  $\text{mg h}^{-1} \text{ cm}^{-2}$ ,  $\mu\text{M h}^{-1}$ ,  $\text{mmol h}^{-1} \text{ g}_{\text{cat}}^{-1}$ . The disunity of units makes direct comparison different. Although we convert the most  $\text{H}_2\text{O}_2$  yield into  $\text{mg h}^{-1}$  in this review, there are still several results that cannot be normalized due to the incomplete system parameters (Table 3). Furthermore, in some research, the newly fabricated or modified electrodes were directly utilized in the EAOP systems. The target pollutant removal efficiency/TOC removal efficiency was the only indicators to evaluate the electrodes, and the  $\text{H}_2\text{O}_2$  yield of the cathodes were not mentioned. In our point of view,  $\text{H}_2\text{O}_2$  yield expressed in the form of "mg  $\text{h}^{-1}$ " could visualize the performance, and it would not be affected by solution volume and electrode area. Furthermore, the CE at a certain current is the most significant indicator of the cathode performance. We highly recommend the publishing of  $\text{H}_2\text{O}_2$  yield together with the CE and current in the future papers. Meanwhile, with the development of materials, electrodes, and the continuous improvement of material requirements, more advanced and rational parameters or criteria are welcomed to be proposed in the future.
- 4) Calculation: there is also divergence in the reactive area of the immersed cathodes. Some calculated the current density ( $\text{mA cm}^{-2}$ ) or  $\text{H}_2\text{O}_2$  yield (in the form of  $\text{mg h}^{-1} \text{ cm}^{-2}$ ) via dividing the projection area of the electrode. However, another group of researchers [193,200,201], including us [279], all believe the effective area should be at least twice the projected area because each side of the electrode is in contact with the electrolyte. This error in the arithmetic will double the calculation result and mislead the readers, which should be avoided in the future.

In summary, with the comprehensive and critical review, we hope to attract scholars from different research fields and use their knowledge to push electrosynthesis of  $\text{H}_2\text{O}_2$  to pilot or even industrially relevant scales.

## Declaration of interests

The authors declare that they have no known competing financial interests or personal relationships that could have appeared to influence the work reported in this paper.

## Acknowledgments

This research was financially supported by the National Natural Science Foundation of China (No. 52070140), the Open Project of State Key Laboratory of Urban Water Resource and Environment, Harbin Institute of Technology (No. HC202151) and the Post-doctoral Science Foundation of China (2021M702439). Jingkun An also thank the scholarship from the Shanghai Tongji Gao Tingyao Environmental Science & Technology Development Foundation (STGEF).

## References

- [1] R. Hage, A. Lienke, Applications of transition-metal catalysts to textile and wood-pulp bleaching, *Angew. Chem., Int. Ed. Engl.* 45 (2) (2006) 206–222.
- [2] B. Puertolas, A.K. Hill, T. Garcia, B. Solsona, L. Torrente-Murciano, In-situ synthesis of hydrogen peroxide in tandem with selective oxidation reactions: a mini-review, *Catal. Today* 248 (2015) 115–127.
- [3] E. Brillas, I. Sires, M.A. Oturan, Electro-Fenton process and related electrochemical technologies based on fenton's reaction chemistry, *Chem. Rev.* 109 (12) (2009) 6570–6631.
- [4] A. Sharma, J. Ahmad, S.J.S. Flora, Application of advanced oxidation processes and toxicity assessment of transformation products, *Environ. Res.* 167 (2018) 223–233.
- [5] E.G. Janzen, Y. Kotake, R.D. Hinton, Stabilities of hydroxyl radical spin adducts of PBN-type spin traps, *Free Radical Biol. Med.* 12 (2) (1992) 169–173.
- [6] S.A. Fast, V.G. Gude, D.D. Truax, J. Martin, B.S. Magbanua, A critical evaluation of advanced oxidation processes for emerging contaminants removal, *Environ. Proc. 4* (1) (2017) 283–302.
- [7] A. Soares, Wastewater treatment in 2050: challenges ahead and future vision in a European context, *Environ. Sci. Ecotechnol.* 2 (2020).
- [8] W.A. Tarpeh, X. Chen, Making wastewater obsolete: selective separations to enable circular water treatment, *Environ. Sci. Ecotechnol.* 5 (2021).
- [9] J.M. Campos-Martín, G. Blanco-Brieva, J.L. Fierro, Hydrogen peroxide synthesis: an outlook beyond the anthraquinone process, *Angew. Chem., Int. Ed. Engl.* 45 (42) (2006) 6962–6984.
- [10] J.K. Edwards, S.J. Freakley, R.J. Lewis, J.C. Pritchard, G.J. Hutchings, Advances in the direct synthesis of hydrogen peroxide from hydrogen and oxygen, *Catal. Today* 248 (2015) 3–9.
- [11] R.B. Rankin, J. Greeley, Trends in selective hydrogen peroxide production on transition metal surfaces from first principles, *ACS Catal.* 2 (12) (2012) 2664–2672.
- [12] S. Yang, A. Verdaguera-Casadevall, L. Arnarson, L. Silvio, V. Colic, R. Frydendal, J. Rossmeisl, I. Chorkendorff, I.E.L. Stephens, Toward the decentralized electrochemical production of H<sub>2</sub>O<sub>2</sub>: a focus on the catalysis, *ACS Catal.* 8 (5) (2018) 4064–4081.
- [13] J.K. Edwards, S.J. Freakley, A.F. Carley, C.J. Kiely, G.J. Hutchings, Strategies for designing supported gold–palladium bimetallic catalysts for the direct synthesis of hydrogen peroxide, *Acc. Chem. Res.* 47 (3) (2014) 845–854.
- [14] Z. Zhu, H. Pan, M. Murugananthan, J. Gong, Y. Zhang, Visible light-driven photocatalytically active g-C<sub>3</sub>N<sub>4</sub> material for enhanced generation of H<sub>2</sub>O<sub>2</sub>, *Appl. Catal. B Environ.* 232 (2018) 19–25.
- [15] H. Hou, X. Zeng, X. Zhang, Production of hydrogen peroxide through photocatalytic processes: a critical review of recent advances, *Angew. Chem., Int. Ed. Engl.* 59 (40) (2020) 17356–17376.
- [16] X. Qu, S. Hu, J. Bai, P. Li, G. Lu, X. Kang, Synthesis of band gap-tunable alkali metal modified graphitic carbon nitride with outstanding photocatalytic H<sub>2</sub>O<sub>2</sub> production ability via molten salt method, *J. Mater. Sci. Technol.* 34 (10) (2018) 1932–1938.
- [17] E. Berl, A new cathodic process for the production of H<sub>2</sub>O<sub>2</sub>, *Transac. Electrochem. Soc.* 76 (1) (1939) 359–369.
- [18] E. Brillas, E. Mur, R. Sauleda, L. Sanchez, J. Peral, X. Domenech, J. Casado, Aniline mineralization by AOP's: anodic oxidation, photocatalysis, electro-Fenton and photoelectro-Fenton processes, *Appl. Catal. B Environ.* 16 (1) (1998) 31–42.
- [19] M.A. Oturan, J.J. Aaron, N. Oturan, J. Pinson, Degradation of chlorophenoxy-acid herbicides in aqueous media, using a novel electrochemical method, *Pestic. Sci.* 55 (5) (1999) 558–562.
- [20] F.C. Moreira, S. García-Segura, V.J.P. Vilar, R.A.R. Boaventura, E. Brillas, Decolorization and mineralization of Sunset Yellow FCF azo dye by anodic oxidation, electro-Fenton, UVA photoelectro-Fenton and solar photoelectro-Fenton processes, *Appl. Catal. B Environ.* 142–143 (2013) 877–890.
- [21] S. García-Segura, E.B. Cavalcanti, E. Brillas, Mineralization of the antibiotic chloramphenicol by solar photoelectro-Fenton, *Appl. Catal. B Environ.* 144 (2014) 588–598.
- [22] M.A. Oturan, J. Pinson, N. Oturan, D. Deprez, Hydroxylation of aromatic drugs by the electro-Fenton method. Formation and identification of the metabolites of Riluzole, *New J. Chem.* 23 (8) (1999) 793–794.
- [23] C. Flox, P. Cabot, F. Centellas, J. Garrido, R. Rodriguez, C. Arias, E. Brillas, Solar photoelectro-Fenton degradation of cresols using a flow reactor with a boron-doped diamond anode, *Appl. Catal. B Environ.* 75 (1–2) (2007) 17–28.
- [24] C. Minero, M. Lucchiari, D. Vione, V. Maurino, Fe(III)-enhanced sonochemical degradation of methylene blue in aqueous solution, *Environ. Sci. Technol.* 39 (22) (2005) 8936–8942.
- [25] B. Boye, M.M. Dieng, E. Brillas, Electrochemical degradation of 2,4,5-trichlorophenoxyacetic acid in aqueous medium by peroxy-coagulation. Effect of pH and UV light, *Electrochim. Acta* 48 (7) (2003) 781–790.
- [26] M. Hou, Y. Chu, X. Li, H. Wang, W. Yao, G. Yu, S. Murayama, Y. Wang, Electro-peroxone degradation of diethyl phthalate: cathode selection, operational parameters, and degradation mechanisms, *J. Hazard Mater.* 319 (2016) 61–68.
- [27] M. Melchionna, P. Fornasiero, M. Prato, The rise of hydrogen peroxide as the main product by metal-free catalysis in oxygen reductions, *Adv. Mater.* 31 (13) (2019), e1802920.
- [28] W. Zhou, X.X. Meng, J.H. Gao, A.N. Alshawabkeh, Hydrogen peroxide generation from O<sub>2</sub> electroreduction for environmental remediation: a state-of-the-art review, *Chemosphere* 225 (2019) 588–607.
- [29] S.C. Perry, D. Pangotra, L. Vieira, L.I. Csepei, V. Sieber, L. Wang, C.P. de Leon, F.C. Walsh, Electrochemical synthesis of hydrogen peroxide from water and oxygen, *Nat. Rev. Chem.* 3 (7) (2019) 442–458.
- [30] J. Zhang, H. Zhang, M.J. Cheng, Q. Lu, Tailoring the electrochemical production of H<sub>2</sub>O<sub>2</sub> : strategies for the rational design of high-performance electrocatalysts, *Small* (2019), e1902845.
- [31] X. Hu, X. Zeng, Y. Liu, J. Lu, X. Zhang, Carbon-based materials for photo- and electrocatalytic synthesis of hydrogen peroxide, *Nanoscale* 12 (30) (2020) 16008–16027.
- [32] H. Zhao, Z.Y. Yuan, Design strategies of non-noble metal-based electrocatalysts for two-electron oxygen reduction to hydrogen peroxide, *ChemSusChem* 14 (7) (2021) 1616–1633.
- [33] J.J. Gao, B. Liu, Progress of electrochemical hydrogen peroxide synthesis over single atom catalysts, *ACS Mater. Let.* 2 (8) (2020) 1008–1024.
- [34] E. Jung, H. Shin, W.H. Antink, Y.E. Sung, T. Hyeon, Recent advances in electrochemical oxygen reduction to H<sub>2</sub>O<sub>2</sub>: catalyst and cell design, *ACS Energy Lett.* 5 (6) (2020) 1881–1892.
- [35] W. Zhou, L. Xie, J.H. Gao, R. Nazari, H.Q. Zhao, X.X. Meng, F. Sun, G.B. Zhao, J. Ma, Selective H<sub>2</sub>O<sub>2</sub> electrosynthesis by O-doped and transition-metal-O-doped carbon cathodes via O-2 electroreduction: a critical review, *Chem. Eng. J.* 410 (2021) 16.
- [36] S. Siahrostami, A. Verdaguera-Casadevall, M. Karamad, D. Deiana, P. Malacrida, B. Wickman, M. Escudero-Escribano, E.A. Paoli, R. Frydendal, T.W. Hansen, I. Chorkendorff, I.E. Stephens, J. Rossmeisl, Enabling direct H<sub>2</sub>O<sub>2</sub> production through rational electrocatalyst design, *Nat. Mater.* 12 (12) (2013) 1137–1143.
- [37] Z.W. Seh, J. Kibsgaard, C.F. Dickens, I. Chorkendorff, J.K. Nørskov, T.F. Jaramillo, Combining theory and experiment in electrocatalysis: insights into materials design, *Science* 355 (6321) (2017).
- [38] Y. Jiao, Y. Zheng, M.T. Jaroniec, S.Z. Qiao, Design of electrocatalysts for oxygen- and hydrogen-involving energy conversion reactions, *Chem. Soc. Rev.* 44 (8) (2015) 2060–2086.
- [39] G.-L. Chai, Z. Hou, T. Ikeda, K. Terakura, Two-electron oxygen reduction on carbon materials catalysts: mechanisms and active sites, *J. Phys. Chem. C* 121 (27) (2017) 14524–14533.
- [40] M.T.M. Koper, Thermodynamic theory of multi-electron transfer reactions: implications for electrocatalysis, *J. Electroanal. Chem.* 660 (2) (2011) 254–260.
- [41] V. Viswanathan, H.A. Hansen, J. Rossmeisl, J.K. Nørskov, Universality in oxygen reduction electrocatalysis on metal surfaces, *ACS Catal.* 2 (8) (2012) 1654–1660.
- [42] R. Jinnouchi, K. Kodama, T. Hatanaka, Y. Morimoto, First principles based mean field model for oxygen reduction reaction, *Phys. Chem. Chem. Phys.* 13 (47) (2011) 21070–21083.
- [43] V. Viswanathan, H.A. Hansen, J. Rossmeisl, J.K. Nørskov, Unifying the 2e(-) and 4e(-) Reduction of Oxygen on Metal Surfaces, *J. Phys. Chem. Lett.* 3 (20) (2012) 2948–2951.
- [44] E. Pizzutillo, O. Kasian, C.H. Choi, S. Cherevko, G.J. Hutchings, K.J.J. Mayrhofer, S.J. Freakley, Electrocatalytic synthesis of hydrogen peroxide on Au-Pd nanoparticles: from fundamentals to continuous production, *Chem. Phys. Lett.* 683 (2017) 436–442.
- [45] J.S. Jirkovsky, I. Panas, E. Ahlberg, M. Halasa, S. Romani, D.J. Schiffirin, Single atom hot-spots at Au-Pd nanoalloys for electrocatalytic H<sub>2</sub>O<sub>2</sub> production, *J. Am. Chem. Soc.* 133 (48) (2011) 19432–19441.
- [46] W.P. Mounfield, A. Garg, Y. Shao-Horn, Y. Román-Leshkov, Electrochemical oxygen reduction for the production of hydrogen peroxide, *Inside Chem.* 4 (1) (2018) 18–19.
- [47] D.S. Su, S. Perathoner, G. Centi, Nanocarbons for the development of advanced catalysts, *Chem. Rev.* 113 (8) (2013) 5782–5816.
- [48] X. Ge, A. Sumboja, D. Wuu, T. An, B. Li, F.W.T. Goh, T.S.A. Hor, Y. Zong, Z. Liu, Oxygen reduction in alkaline media: from mechanisms to recent advances of

- catalysts, *ACS Catal.* 5 (8) (2015) 4643–4667.
- [49] R. Zhou, Y. Zheng, M. Jaroniec, S.-Z. Qiao, Determination of the electron transfer number for the oxygen reduction reaction: from theory to experiment, *ACS Catal.* 6 (7) (2016) 4720–4728.
- [50] A.J. Bard, L.R. Faulkner, J. Leddy, C.C. Zoski, *Electrochemical Methods: Fundamentals and Applications*, Wiley New York, 1980.
- [51] C. Hu, L. Dai, Doping of carbon materials for metal-free electrocatalysis, *Adv. Mater.* 31 (7) (2019), e1804672.
- [52] G.-F. Norra, L. Baptista-Pires, E. Cuervo Lumbaque, C.M. Borrego, J. Radjenovic, Chlorine-free electrochemical disinfection using graphene sponge electrodes, *Chem. Eng. J.* 430 (2022).
- [53] K.S. Novoselov, A.K. Geim, S.V. Morozov, D. Jiang, Y. Zhang, S.V. Dubonos, I.V. Grigorieva, A.A. Firsov, Electric field effect in atomically thin carbon films, *Science* 306 (5696) (2004) 666–669.
- [54] X.S. Li, W.W. Cai, J.H. An, S. Kim, J. Nah, D.X. Yang, R. Piner, A. Velamakanni, I. Jung, E. Tutuc, S.K. Banerjee, L. Colombo, R.S. Ruoff, Large-area synthesis of high-quality and uniform graphene films on copper foils, *Science* 324 (5932) (2009) 1312–1314.
- [55] C. Berger, Z.M. Song, X.B. Li, X.S. Wu, N. Brown, C. Naud, D. Mayou, T.B. Li, J. Hass, A.N. Marchenkov, E.H. Conrad, P.N. First, W.A. de Heer, Electronic confinement and coherence in patterned epitaxial graphene, *Science* 312 (5777) (2006) 1191–1196.
- [56] B. Qi, L. He, X.J. Bo, H.J. Yang, L.P. Guo, Electrochemical preparation of free-standing few-layer graphene through oxidation-reduction cycling, *Chem. Eng. J.* 171 (1) (2011) 340–344.
- [57] O.C. Compton, B. Jain, D.A. Dikin, A. Abouimrane, K. Amine, S.T. Nguyen, Chemically active reduced graphene oxide with tunable C/O ratios, *ACS Nano* 5 (6) (2011) 4380–4391.
- [58] M. Dresselhaus, Carbon connections promise nanoelectronics, *Phys. World* 9 (5) (1996) 18.
- [59] A.K. Geim, K.S. Novoselov, *The Rise of Graphene, Nanoscience and Technology: A Collection of Reviews from Nature Journals*, World Scientific, 2010, pp. 11–19.
- [60] L. Dai, *Carbon Nanotechnology: Recent Developments in Chemistry, Physics, Materials Science and Device Applications*, Elsevier, 2006.
- [61] S. Iijima, Helical microtubules of graphitic carbon, *Nature* 354 (6348) (1991) 56–58.
- [62] A. Thess, R. Lee, P. Nikolaev, H. Dai, P. Petit, J. Robert, C. Xu, Y.H. Lee, S.G. Kim, A.G. Rinzler, Crystalline ropes of metallic carbon nanotubes, *Science* 273 (5274) (1996) 483–487.
- [63] S. Amelinckx, X. Zhang, D. Bernaerts, X. Zhang, V. Ivanov, J. Nagy, A formation mechanism for catalytically grown helix-shaped graphite nanotubes, *Science* 265 (5172) (1994) 635–639.
- [64] M.F. De Volder, S.H. Tawfick, R.H. Baughman, A.J. Hart, Carbon nanotubes: present and future commercial applications, *Science* 339 (6119) (2013) 535–539.
- [65] C.M. Long, M.A. Nasarella, P.A. Valberg, Carbon black vs. black carbon and other airborne materials containing elemental carbon: physical and chemical distinctions, *Environ. Pollut.* 181 (2013) 271–286.
- [66] A.Y. Watson, P.A. Valberg, Carbon black and soot: two different substances, *AIHaj Am. Ind. Hygiene Assoc.* 62 (2) (2001) 218–228.
- [67] S. Tang, G. Sun, J. Qi, S. Sun, J. Guo, Q. Xin, G.M. Haarberg, Review of new carbon materials as catalyst supports in direct alcohol fuel cells, *Chin. J. Catal.* 31 (1) (2010) 12–17.
- [68] D. Pantea, H. Darmstadt, S. Kaliaguine, L. Sümichen, C. Roy, Electrical conductivity of thermal carbon blacks: influence of surface chemistry, *Carbon* 39 (8) (2001) 1147–1158.
- [69] B. Marinho, M. Ghislandi, E. Tkalya, C.E. Koning, G. de With, Electrical conductivity of compacts of graphene, multi-wall carbon nanotubes, carbon black, and graphite powder, *Powder Technol.* 221 (2012) 351–358.
- [70] T.A. Silva, F.C. Moraes, B.C. Janegitz, O. Fatibello-Filho, Electrochemical biosensors based on nanostructured carbon black: a review, *J. Nanomater.* (2017) 1–14, 2017.
- [71] T.Y. Ma, L. Liu, Z.Y. Yuan, Direct synthesis of ordered mesoporous carbons, *Chem. Soc. Rev.* 42 (9) (2013) 3977–4003.
- [72] A. Stein, Advances in microporous and mesoporous solids—highlights of recent progress, *Adv. Mater.* 15 (10) (2003) 763–775.
- [73] A. Verdaguera-Casadevall, D. Deiana, M. Karamad, S. Siahrostami, P. Malacrida, T.W. Hansen, J. Rossmeisl, I. Chorkendorff, I.E. Stephens, Trends in the electrochemical synthesis of  $H_2O_2$ : enhancing activity and selectivity by electrocatalytic site engineering, *Nano Lett.* 14 (3) (2014) 1603–1608.
- [74] L. Yang, J. Shui, L. Du, Y. Shao, J. Liu, L. Dai, Z. Hu, Carbon-based metal-free ORR electrocatalysts for fuel cells: past, present, and future, *Adv. Mater.* 31 (13) (2019), e1804799.
- [75] K. Gong, F. Du, Z. Xia, M. Durstock, L. Dai, Nitrogen-doped carbon nanotube arrays with high electrocatalytic activity for oxygen reduction, *Science* 323 (5915) (2009) 760–764.
- [76] N. Daems, X. Sheng, I.F. Vankelecom, P.P. Pescarmona, Metal-free doped carbon materials as electrocatalysts for the oxygen reduction reaction, *J. Mater. Chem. 2* (12) (2014) 4085–4110.
- [77] Z. Yang, Z. Yao, G. Li, G. Fang, H. Nie, Z. Liu, X. Zhou, X.a. Chen, S. Huang, Sulfur-doped graphene as an efficient metal-free cathode catalyst for oxygen reduction, *ACS Nano* 6 (1) (2012) 205–211.
- [78] T. Asefa, Metal-free and noble metal-free heteroatom-doped nanostructured carbons as prospective sustainable electrocatalysts, *Acc. Chem. Res.* 49 (9) (2016) 1873–1883.
- [79] X. Liu, L. Dai, Carbon-based metal-free catalysts, *Nat. Rev. Mater.* 1 (11) (2016) 1–12.
- [80] D. Guo, R. Shibuya, C. Akiba, S. Saji, T. Kondo, J. Nakamura, Active sites of nitrogen-doped carbon materials for oxygen reduction reaction clarified using model catalysts, *Science* 351 (6271) (2016) 361–365.
- [81] K. Artyushkova, A. Serov, S. Rojas-Carbonell, P. Atanassov, Chemistry of multitudinous active sites for oxygen reduction reaction in transition metal–nitrogen–carbon electrocatalysts, *J. Phys. Chem. C* 119 (46) (2015) 25917–25928.
- [82] I. Matanovic, K. Artyushkova, P. Atanassov, Understanding PGM-free catalysts by linking density functional theory calculations and structural analysis: perspectives and challenges, *Cur. Opin. Electrochem.* 9 (2018) 137–144.
- [83] D. Geng, Y. Chen, Y. Chen, Y. Li, R. Li, X. Sun, S. Ye, S. Knights, High oxygen-reduction activity and durability of nitrogen-doped graphene, *Energy Environ. Sci.* 4 (3) (2011) 760–764.
- [84] S. Kabir, K. Artyushkova, A. Serov, B. Kiefer, P. Atanassov, Binding energy shifts for nitrogen-containing graphene-based electrocatalysts – experiments and DFT calculations, *Surf. Interface Anal.* 48 (5) (2016) 293–300.
- [85] T.P. Fellinger, F. Hasche, P. Strasser, M. Antonietti, Mesoporous nitrogen-doped carbon for the electrocatalytic synthesis of hydrogen peroxide, *J. Am. Chem. Soc.* 134 (9) (2012) 4072–4075.
- [86] J.P. Paraknowitsch, J. Zhang, D. Su, A. Thomas, M. Antonietti, Ionic liquids as precursors for nitrogen-doped graphitic carbon, *Adv. Mater.* 22 (1) (2010) 87–92.
- [87] Y. Sun, I. Sinev, W. Ju, A. Bergmann, S. Dresp, S. Kühl, C. Spöri, H. Schmies, H. Wang, D. Berndsmeyer, B. Paul, R. Schmack, R. Krahnert, B. Roldan Cuenya, P. Strasser, Efficient electrochemical hydrogen peroxide production from molecular oxygen on nitrogen-doped mesoporous carbon catalysts, *ACS Catal.* 8 (4) (2018) 2844–2856.
- [88] Y. Sun, S. Li, Z.P. Jovanov, D. Berndsmeyer, H. Wang, B. Paul, X. Wang, S. Kuhl, P. Strasser, Structure, activity, and faradaic efficiency of nitrogen-doped porous carbon catalysts for direct electrochemical hydrogen peroxide production, *ChemSusChem* 11 (19) (2018) 3388–3395.
- [89] Y.-H. Lee, F. Li, K.-H. Chang, C.-C. Hu, T. Ohsaka, Novel synthesis of N-doped porous carbons from collagen for electrocatalytic production of  $H_2O_2$ , *Appl. Catal. B Environ.* 126 (2012) 208–214.
- [90] X. Sheng, N. Daems, B. Geboes, M. Kurtepeeli, S. Bals, T. Breugelmans, A. Hubin, I.F. Vankelecom, P.P. Pescarmona, N-doped ordered mesoporous carbons prepared by a two-step nanocasting strategy as highly active and selective electrocatalysts for the reduction of  $O_2$  to  $H_2O_2$ , *Appl. Catal. B Environ.* 176 (2015) 212–224.
- [91] J. Park, Y. Nabae, T. Hayakawa, M.A. Kakimoto, Highly selective two-electron oxygen reduction catalyzed by mesoporous nitrogen-doped carbon, *ACS Catal.* 4 (10) (2014) 3749–3754.
- [92] F. Hasché, M. Oezaslan, P. Strasser, T.-P. Fellinger, Electrocatalytic hydrogen peroxide formation on mesoporous non-metal nitrogen-doped carbon catalyst, *J. Energy Chem.* 25 (2) (2016) 251–257.
- [93] Y. Wu, A. Muthukrishnan, S. Nagata, Y. Nabae, Kinetic understanding of the reduction of oxygen to hydrogen peroxide over an N-doped carbon electrocatalyst, *J. Phys. Chem. C* 123 (7) (2019) 4590–4596.
- [94] J.P. Paraknowitsch, A. Thomas, Doping carbons beyond nitrogen: an overview of advanced heteroatom doped carbons with boron, sulphur and phosphorus for energy applications, *Energy Environ. Sci.* 6 (10) (2013).
- [95] X. Bai, E. Zhao, K. Li, Y. Wang, M. Jiao, F. He, Y. Sun, H. Sun, Z. Wu, Theoretical insights on the reaction pathways for oxygen reduction reaction on phosphorus doped graphene, *Carbon* 105 (2016) 214–223.
- [96] X. Zhang, Z. Lu, Z. Fu, Y. Tang, D. Ma, Z. Yang, The mechanisms of oxygen reduction reaction on phosphorus doped graphene: a first-principles study, *J. Power Sources* 276 (2015) 222–229.
- [97] L. Yang, S. Jiang, Y. Zhao, L. Zhu, S. Chen, X. Wang, Q. Wu, J. Ma, Y. Ma, Z. Hu, Boron-doped carbon nanotubes as metal-free electrocatalysts for the oxygen reduction reaction, *Angew. Chem., Int. Ed. Engl.* 50 (31) (2011) 7132–7135.
- [98] L. Zhang, J. Niu, M. Li, Z. Xia, Catalytic mechanisms of sulfur-doped graphene as efficient oxygen reduction reaction catalysts for fuel cells, *J. Phys. Chem. C* 118 (7) (2014) 3545–3553.
- [99] H.Y. Liu, Z.F. Hou, C.H. Hu, Y. Yang, Z.Z. Zhu, Electronic and magnetic properties of fluorinated graphene with different coverage of fluorine, *J. Phys. Chem. C* 116 (34) (2012) 18193–18201.
- [100] Z. Ju, S. Zhang, Z. Xing, Q. Zhuang, Y. Qiang, Y. Qian, Direct synthesis of few-layer F-doped graphene foam and its lithium/potassium storage properties, *ACS Appl. Mater. Interfaces* 8 (32) (2016) 20682–20690.
- [101] K. Zhao, X. Quan, S. Chen, H. Yu, Y. Zhang, H. Zhao, Enhanced electro-Fenton performance by fluorine-doped porous carbon for removal of organic pollutants in wastewater, *Chem. Eng. J.* 354 (2018) 606–615.
- [102] K. Zhao, Y. Su, X. Quan, Y.M. Liu, S. Chen, H.T. Yu, Enhanced  $H_2O_2$  production by selective electrochemical reduction of  $O_2$  on fluorine-doped hierarchically porous carbon, *J. Catal.* 357 (2018) 118–126.
- [103] Y. Xia, X. Zhao, C. Xia, Z.Y. Wu, P. Zhu, J.Y.T. Kim, X. Bai, G. Gao, Y. Hu, J. Zhong, Y. Liu, H. Wang, Highly active and selective oxygen reduction to  $H_2O_2$  on boron-doped carbon for high production rates, *Nat. Commun.* 12 (1) (2021) 4225.
- [104] V. Perazzolo, C. Durante, R. Pilot, A. Paduano, J. Zheng, G.A. Rizzi, A. Martucci, G. Granozzi, A. Gennaro, Nitrogen and sulfur doped mesoporous carbon as metal-free electrocatalysts for the in situ production of hydrogen peroxide,

- Carbon 95 (2015) 949–963.
- [105] L. Roldán, L. Truong-Phuoc, A. Ansón-Casaos, C. Pham-Huu, E. García-Bordejé, Mesoporous carbon doped with N,S heteroatoms prepared by one-pot auto-assembly of molecular precursor for electrocatalytic hydrogen peroxide synthesis, *Catal. Today* 301 (2018) 2–10.
- [106] Y. Zhu, F. Deng, S. Qiu, F. Ma, Y. Zheng, R. Lian, Enhanced electro-Fenton degradation of sulfonamides using the N, S co-doped cathode: mechanism for H<sub>2</sub>O<sub>2</sub> formation and pollutants decay, *J. Hazard Mater.* 403 (2021) 123950.
- [107] Y. Zhao, L. Yang, S. Chen, X. Wang, Y. Ma, Q. Wu, Y. Jiang, W. Qian, Z. Hu, Can boron and nitrogen co-doping improve oxygen reduction reaction activity of carbon nanotubes? *J. Am. Chem. Soc.* 135 (4) (2013) 1201–1204.
- [108] S. Wang, E. Iyyappaperumal, A. Roy, Y. Xue, D. Yu, L. Dai, Vertically aligned BCN nanotubes as efficient metal-free electrocatalysts for the oxygen reduction reaction: a synergistic effect by Co-doping with boron and nitrogen, *Angew. Chem., Int. Ed. Engl.* 50 (49) (2011) 11756–11760.
- [109] S. Chen, Z. Chen, S. Siahrostami, D. Higgins, D. Nordlund, D. Sokaras, T.R. Kim, Y. Liu, X. Yan, E. Nilsson, R. Sinclair, J.K. Norskov, T.F. Jaramillo, Z. Bao, Designing boron nitride islands in carbon materials for efficient electrochemical synthesis of hydrogen peroxide, *J. Am. Chem. Soc.* 140 (25) (2018) 7851–7859.
- [110] J.W.F. To, J.W.D. Ng, S. Siahrostami, A.L. Koh, Y.J. Lee, Z.H. Chen, K.D. Fong, S.C. Chen, J.J. He, W.G. Bae, J. Wilcox, H.Y. Jeong, K. Kim, F. Studt, J.K. Norskov, T.F. Jaramillo, Z.N. Bao, High-performance oxygen reduction and evolution carbon catalysis: from mechanistic studies to device integration, *Nano Res.* 10 (4) (2017) 1163–1177.
- [111] J.K. Norskov, J. Rossmeisl, A. Logadottir, L. Lindqvist, J.R. Kitchin, T. Bligaard, H. Jonsson, Origin of the overpotential for oxygen reduction at a fuel-cell cathode, *J. Phys. Chem. B* 108 (46) (2004) 17886–17892.
- [112] K. Li, J. Liu, J. Li, Z. Wan, Effects of N mono- and N/P dual-doping on H<sub>2</sub>O<sub>2</sub>, OH generation, and MB electrochemical degradation efficiency of activated carbon fiber electrodes, *Chemosphere* 193 (2018) 800–810.
- [113] R.-S. Zhong, Y.-H. Qin, D.-F. Niu, J.-W. Tian, X.-S. Zhang, X.-G. Zhou, S.-G. Sun, W.-K. Yuan, Effect of carbon nanofiber surface functional groups on oxygen reduction in alkaline solution, *J. Power Sources* 225 (2013) 192–199.
- [114] B. Li, D. Su, The nucleophilicity of the oxygen functional groups on carbon materials: a DFT analysis, *Chemistry* 20 (26) (2014) 7890–7894.
- [115] H.W. Kim, M.B. Ross, N. Kornienko, L. Zhang, J. Guo, P. Yang, B.D. McCloskey, Efficient hydrogen peroxide generation using reduced graphene oxide-based oxygen reduction electrocatalysts, *Nat. Catal.* 1 (4) (2018) 282–290.
- [116] H.W. Kim, V.J. Lukas, H. Park, S. Park, K.M. Diederichsen, J. Lim, Y.H. Cho, J. Kim, W. Kim, T.H. Han, J. Voss, A.C. Luntz, B.D. McCloskey, Mechanisms of two-electron and four-electron electrochemical oxygen reduction reactions at nitrogen-doped reduced graphene oxide, *ACS Catal.* 10 (1) (2019) 852–863.
- [117] F. Sun, C. Yang, Z. Qu, W. Zhou, Y. Ding, J. Gao, G. Zhao, D. Xing, Y. Lu, Inexpensive activated coke electrocatalyst for high-efficiency hydrogen peroxide production: coupling effects of amorphous carbon cluster and oxygen dopant, *Appl. Catal. B Environ.* 286 (2021).
- [118] Z.Y. Lu, G.X. Chen, S. Siahrostami, Z.H. Chen, K. Liu, J. Xie, L. Liao, T. Wu, D.C. Lin, Y.Y. Liu, T.F. Jaramillo, J.K. Norskov, Y. Cui, High-efficiency oxygen reduction to hydrogen peroxide catalysed by oxidized carbon materials, *Nat. Catal.* 1 (2) (2018) 156–162.
- [119] H. Zhang, Y. Li, Y. Zhao, G. Li, F. Zhang, Carbon black oxidized by air calcination for enhanced H<sub>2</sub>O<sub>2</sub> generation and effective organics degradation, *ACS Appl. Mater. Interfaces* 11 (31) (2019) 27846–27853.
- [120] X. Lu, D. Wang, K.-H. Wu, X. Guo, W. Qi, Oxygen reduction to hydrogen peroxide on oxidized nanocarbon: identification and quantification of active sites, *J. Colloid Interface Sci.* 573 (2020) 376–383.
- [121] M. Qin, S. Fan, L. Wang, G. Gan, X. Wang, J. Cheng, Z. Hao, X. Li, Oxygen and nitrogen co-doped ordered mesoporous carbon materials enhanced the electrochemical selectivity of O<sub>2</sub> reduction to H<sub>2</sub>O<sub>2</sub>, *J. Colloid Interface Sci.* 562 (2020) 540–549.
- [122] A. Bonakdarpour, D. Esau, H. Cheng, A. Wang, E. Gyenge, D.P. Wilkinson, Preparation and electrochemical studies of metal–carbon composite catalysts for small-scale electrosynthesis of H<sub>2</sub>O<sub>2</sub>, *Electrochim. Acta* 56 (25) (2011) 9074–9081.
- [123] D. Strmcnik, M. Escudero-Escribano, K. Kodama, V.R. Stamenkovic, A. Cuesta, N.M. Marković, Enhanced electrocatalysis of the oxygen reduction reaction based on patterning of platinum surfaces with cyanide, *Nat. Chem.* 2 (10) (2010) 880–885.
- [124] Q. Zhang, X. Tan, N.M. Bedford, Z. Han, L. Thomsen, S. Smith, R. Amal, X. Lu, Direct insights into the role of epoxy groups on cobalt sites for acidic H<sub>2</sub>O<sub>2</sub> production, *Nat. Commun.* 11 (1) (2020) 4181.
- [125] R. Jasinski, A new fuel cell cathode catalyst, *Nature* 201 (4925) (1964) 1212–1213.
- [126] M. Shen, C. Wei, K. Ai, L. Lu, Transition metal–nitrogen–carbon nanostructured catalysts for the oxygen reduction reaction: from mechanistic insights to structural optimization, *Nano Res.* 10 (5) (2017) 1449–1470.
- [127] H. Liu, L. Zhang, J. Zhang, D. Ghosh, J. Jung, B.W. Downing, E. Whittemore, Electrocatalytic reduction of O<sub>2</sub> and H<sub>2</sub>O<sub>2</sub> by adsorbed cobalt tetramethoxyphenyl porphyrin and its application for fuel cell cathodes, *J. Power Sources* 161 (2) (2006) 743–752.
- [128] K. Singh, F. Razmjooei, J.-S. Yu, Active sites and factors influencing them for efficient oxygen reduction reaction in metal-N coordinated pyrolyzed and non-pyrolyzed catalysts: a review, *J. Mater. Chem. 5* (38) (2017) 20095–20119.
- [129] G. Wu, A. Santandreu, W. Kellogg, S. Gupta, O. Ogoke, H. Zhang, H.-L. Wang, L. Dai, Carbon nanocomposite catalysts for oxygen reduction and evolution reactions: from nitrogen doping to transition-metal addition, *Nano Energy* 29 (2016) 83–110.
- [130] M. Shao, Q. Chang, J.P. Dodelet, R. Chenitz, Recent advances in electrocatalysts for oxygen reduction reaction, *Chem. Rev.* 116 (6) (2016) 3594–3657.
- [131] F. Jaouen, J.-P. Dodelet, Average turn-over frequency of O<sub>2</sub> electro-reduction for Fe/N/C and Co/N/C catalysts in PEFCs, *Electrochim. Acta* 52 (19) (2007) 5975–5984.
- [132] C.W.B. Bezerra, L. Zhang, K. Lee, H. Liu, A.L.B. Marques, E.P. Marques, H. Wang, J. Zhang, A review of Fe–N/C and Co–N/C catalysts for the oxygen reduction reaction, *Electrochim. Acta* 53 (15) (2008) 4937–4951.
- [133] M. Campos, W. Siriwatcharapiboon, R.J. Potter, S.L. Horswell, Selectivity of cobalt-based catalysts towards hydrogen peroxide formation during the reduction of oxygen, *Catal. Today* 202 (2013) 135–143.
- [134] T.S. Olson, S. Pylypenko, P. Atanassov, K. Asazawa, K. Yamada, H. Tanaka, Anion-exchange membrane fuel cells: dual-site mechanism of oxygen reduction reaction in alkaline media on cobalt–polypyrrole electrocatalysts, *J. Phys. Chem. C* 114 (11) (2010) 5049–5059.
- [135] Wu Gang, Karren More L., Christina Johnston M., Zelenay, Piotr, High-performance electrocatalysts for oxygen reduction derived from polyaniline, iron, and cobalt, *Science* 332 (6028) (2011) 443–447.
- [136] A. Byeon, J. Cho, J.G.M. Kim, K.H. Chae, H.Y. Park, S.W. Hong, H.C. Ham, S.W. Lee, K.R. Yoon, J.Y. Kim, High-yield electrochemical hydrogen peroxide production from an enhanced two-electron oxygen reduction pathway by mesoporous nitrogen-doped carbon and manganese hybrid electrocatalysts, *Nanoscale Horizons* 5 (5) (2020) 832–838.
- [137] B.Q. Li, C.X. Zhao, J.N. Liu, Q. Zhang, Electrosynthesis of hydrogen peroxide synergistically catalyzed by atomic Co-Nx –C sites and oxygen functional groups in noble-metal-free electrocatalysts, *Adv. Mater.* 31 (35) (2019), e1808173.
- [138] J. Kong, W. Cheng, Recent advances in the rational design of electrocatalysts towards the oxygen reduction reaction, *Chin. J. Catal.* 38 (6) (2017) 951–969.
- [139] R.F.B. De Souza, A.E.A. Flausino, D.C. Rascio, R.T.S. Oliveira, E.T. Neto, M.L. Calegaro, M.C. Santos, Ethanol oxidation reaction on PtCeO<sub>2</sub>/C electrocatalysts prepared by the polymeric precursor method, *Appl. Catal. B Environ.* 91 (1–2) (2009) 516–523.
- [140] H.B. Suffredini, V. Tricoli, L.A. Avaca, N. Vatistas, Sol–gel method to prepare active Pt–RuO<sub>2</sub> coatings on carbon powder for methanol oxidation, *Electrochim. Commun.* 6 (10) (2004) 1025–1028.
- [141] M.H.M.T. Assumpção, A. Moraes, R.F.B. De Souza, I. Gaubeur, R.T.S. Oliveira, V.S. Antonin, G.R.P. Malpass, R.S. Rocha, M.L. Calegaro, M.R.V. Lanza, M.C. Santos, Low content cerium oxide nanoparticles on carbon for hydrogen peroxide electrosynthesis, *Appl. Catal. Gen.* 411–412 (2012) 1–6.
- [142] A. Moraes, M.H.M.T. Assumpção, R. Papai, I. Gaubeur, R.S. Rocha, R.M. Reis, M.L. Calegaro, M.R.V. Lanza, M.C. Santos, Use of a vanadium nanostructured material for hydrogen peroxide electrogeneration, *J. Electroanal. Chem.* 719 (2014) 127–132.
- [143] V.S. Antonin, M.H.M.T. Assumpção, J.C.M. Silva, L.S. Parreira, M.R.V. Lanza, M.C. Santos, Synthesis and characterization of nanostructured electrocatalysts based on nickel and tin for hydrogen peroxide electrogeneration, *Electrochim. Acta* 109 (2013) 245–251.
- [144] M.H.M.T. Assumpção, R.F.B. De Souza, R.M. Reis, R.S. Rocha, J.R. Steter, P. Hammer, I. Gaubeur, M.L. Calegaro, M.R.V. Lanza, M.C. Santos, Low tungsten content of nanostructured material supported on carbon for the degradation of phenol, *Appl. Catal. B Environ.* 142–143 (2013) 479–486.
- [145] L.R. Aveiro, A.G.M. da Silva, V.S. Antonin, E.G. Candido, L.S. Parreira, R.S. Geonmonond, I.C. de Freitas, M.R.V. Lanza, P.H.C. Camargo, M.C. Santos, Carbon-supported MnO<sub>2</sub> nanoflowers: introducing oxygen vacancies for optimized volcano-type electrocatalytic activities towards H<sub>2</sub>O<sub>2</sub> generation, *Electrochim. Acta* 268 (2018) 101–110.
- [146] E.C. Paz, L.R. Aveiro, V.S. Pinheiro, F.M. Souza, V.B. Lima, F.L. Silva, P. Hammer, M.R.V. Lanza, M.C. Santos, Evaluation of H<sub>2</sub>O<sub>2</sub> electrogeneration and decolorization of Orange II azo dye using tungsten oxide nanoparticle-modified carbon, *Appl. Catal. B Environ.* 232 (2018) 436–445.
- [147] V.S. Antonin, L.S. Parreira, L.R. Aveiro, F.L. Silva, R.B. Valim, P. Hammer, M.R.V. Lanza, M.C. Santos, W@Au nanostructures modifying carbon as materials for hydrogen peroxide electrogeneration, *Electrochim. Acta* 231 (2017) 713–720.
- [148] J.F. Carneiro, R.S. Rocha, P. Hammer, R. Bertazzoli, M.R.V. Lanza, Hydrogen peroxide electrogeneration in gas diffusion electrode nanostructured with Ta<sub>2</sub>O<sub>5</sub>, *Appl. Catal. Gen.* 517 (2016) 161–167.
- [149] M.H.M.T. Assumpção, A. Moraes, R.F.B. De Souza, M.L. Calegaro, M.R.V. Lanza, E.R. Leite, M.A.L. Cordeiro, P. Hammer, M.C. Santos, Influence of the preparation method and the support on H<sub>2</sub>O<sub>2</sub> electrogeneration using cerium oxide nanoparticles, *Electrochim. Acta* 111 (2013) 339–343.
- [150] G.V. Fortunato, M.S. Kronka, A.J. dos Santos, M. Ledendecker, M.R.V. Lanza, Low Pd loadings onto Printex L6: synthesis, characterization and performance towards H<sub>2</sub>O<sub>2</sub> generation for electrochemical water treatment technologies, *Chemosphere* 259 (2020) 11.
- [151] J.F. Carneiro, M.J. Paulo, M. Siaj, A.C. Tavares, M.R.V. Lanza, Nb<sub>2</sub>O<sub>5</sub> nanoparticles supported on reduced graphene oxide sheets as electrocatalyst for

- the H<sub>2</sub>O<sub>2</sub> electrogeneration, *J. Catal.* 332 (2015) 51–61.
- [152] W.R.P. Barros, Q. Wei, G. Zhang, S. Sun, M.R.V. Lanza, A.C. Tavares, Oxygen reduction to hydrogen peroxide on Fe3O4 nanoparticles supported on Printex carbon and Graphene, *Electrochim. Acta* 162 (2015) 263–270.
- [153] S. Ni, Z. Li, J. Yang, Oxygen molecule dissociation on carbon nanostructures with different types of nitrogen doping, *Nanoscale* 4 (4) (2012) 1184–1189.
- [154] X. Yan, Y. Jia, X. Yao, Defects on carbons for electrocatalytic oxygen reduction, *Chem. Soc. Rev.* 47 (20) (2018) 7628–7658.
- [155] L. Zhang, Q. Xu, J. Niu, Z. Xia, Role of lattice defects in catalytic activities of graphene clusters for fuel cells, *Phys. Chem. Chem. Phys.* 17 (26) (2015) 16733–16743.
- [156] Y. Jiang, L. Yang, T. Sun, J. Zhao, Z. Lyu, O. Zhuo, X. Wang, Q. Wu, J. Ma, Z. Hu, Significant contribution of intrinsic carbon defects to oxygen reduction activity, *ACS Catal.* 5 (11) (2015) 6707–6712.
- [157] Y. Jia, L. Zhang, A. Du, G. Gao, J. Chen, X. Yan, C.L. Brown, X. Yao, Defect graphene as a trifunctional catalyst for electrochemical reactions, *Adv. Mater.* 28 (43) (2016) 9532–9538.
- [158] Y. Liu, X. Quan, X. Fan, H. Wang, S. Chen, High-yield electrosynthesis of hydrogen peroxide from oxygen reduction by hierarchically porous carbon, *Angew. Chem., Int. Ed. Engl.* 54 (23) (2015) 6837–6841.
- [159] L. Tao, Q. Wang, S. Dou, Z. Ma, J. Huo, S. Wang, L. Dai, Edge-rich and dopant-free graphene as a highly efficient metal-free electrocatalyst for the oxygen reduction reaction, *Chem. Commun. (Camb.)* 52 (13) (2016) 2764–2767.
- [160] S. Chen, Z. Chen, S. Siahrostami, T.R. Kim, D. Nordlund, D. Sokaras, S. Nowak, J.W.F. To, D. Higgins, R. Sinclair, J.K. Nørskov, T.F. Jaraillo, Z. Bao, Defective carbon-based materials for the electrochemical synthesis of hydrogen peroxide, *ACS Sustain. Chem. Eng.* 6 (1) (2017) 311–317.
- [161] H.W. Kim, H. Park, J.S. Roh, J.E. Shin, T.H. Lee, L. Zhang, Y.H. Cho, H.W. Yoon, V.J. Bokas, J. Guo, H.B. Park, T.H. Han, B.D. McCloskey, Carbon defect characterization of nitrogen-doped reduced graphene oxide electrocatalysts for the two-electron oxygen reduction reaction, *Chem. Mater.* 31 (11) (2019) 3967–3973.
- [162] L. Han, Y. Sun, S. Li, C. Cheng, C.E. Halbig, P. Feicht, J.L. Hübner, P. Strasser, S. Eigler, In-plane carbon lattice-defect regulating electrochemical oxygen reduction to hydrogen peroxide production over nitrogen-doped graphene, *ACS Catal.* 9 (2) (2019) 1283–1288.
- [163] J. An, N. Li, Y. Wu, S. Wang, C. Liao, Q. Zhao, L. Zhou, T. Li, X. Wang, Y. Feng, Revealing decay mechanisms of H<sub>2</sub>O<sub>2</sub>-based electrochemical advanced oxidation processes after long-term operation for phenol degradation, *Environ. Sci. Technol.* 54 (17) (2020) 10916–10925.
- [164] A.D. Pozzo, L.D. Palma, C. Merli, E. Petrucci, An experimental comparison of a graphite electrode and a gas diffusion electrode for the cathodic production of hydrogen peroxide, *J. Appl. Electrochem.* 35 (4) (2005) 413–419.
- [165] Z.M. Qiang, J.H. Chang, C.P. Huang, Electrochemical generation of hydrogen peroxide from dissolved oxygen in acidic solutions, *Water Res.* 36 (1) (2002) 85–94.
- [166] L. Fu, S.-J. You, F.-I. Yang, M.-m. Gao, X.-h. Fang, G.-q. Zhang, Synthesis of hydrogen peroxide in microbial fuel cell, *J. Chem. Technol. Biotechnol.* 85 (5) (2010) 715–719.
- [167] J.Y. Chen, N. Li, L. Zhao, Three-dimensional electrode microbial fuel cell for hydrogen peroxide synthesis coupled to wastewater treatment, *J. Power Sources* 254 (2014) 316–322.
- [168] N. Li, S. Wang, J. An, Y. Feng, Acid pretreatment of three-dimensional graphite cathodes enhances the hydrogen peroxide synthesis in bioelectrochemical systems, *Sci. Total Environ.* 630 (2018) 308–313.
- [169] Z. Jiang, J. Yu, T. Huang, M. Sun, Recent advance on polyaniline or polypyrrole-derived electrocatalysts for oxygen reduction reaction, *Polymers* 10 (12) (2018).
- [170] G. Zhang, W. Yang, F. Yang, Electrochemical behavior and electrocatalytic activity of anthraquinonedisulphonate in solution phase and as doping species at polypyrrole modified glassy carbon electrode, *J. Electroanal. Chem.* 602 (2) (2007) 163–171.
- [171] R.S. Rocha, R.B. Valim, L.C. Trevelin, J.R. Steter, J.F. Carneiro, J.C. Forti, R. Bertazzoli, M.R.V. Lanza, Electrocatalysis of hydrogen peroxide generation using oxygen-fed gas diffusion electrodes made of carbon black modified with quinone compounds, *Electrocatalysis* 11 (3) (2020) 338–346.
- [172] G. Zhang, F. Yang, M. Gao, X. Fang, L. Liu, Electro-Fenton degradation of azo dye using polypyrrole/anthraquinonedisulphonate composite film modified graphite cathode in acidic aqueous solutions, *Electrochim. Acta* 53 (16) (2008) 5155–5161.
- [173] A.R. Khataee, M. Safarpour, M. Zarei, S. Aber, Electrochemical generation of H<sub>2</sub>O<sub>2</sub> using immobilized carbon nanotubes on graphite electrode fed with air: investigation of operational parameters, *J. Electroanal. Chem.* 659 (1) (2011) 63–68.
- [174] H. Rabl, D. Wielend, S. Tekoglu, H. Seelajaroen, H. Neugebauer, N. Heitzmann, D.H. Apaydin, M.C. Scharber, N.S. Sariciftci, Are polyaniline and polypyrrole electrocatalysts for oxygen (O<sub>2</sub>) reduction to hydrogen peroxide (H<sub>2</sub>O<sub>2</sub>)? *ACS Appl. Energy Mater.* 3 (11) (2020) 10611–10618.
- [175] H. Rabl, D. Wielend, S. Tekoglu, H. Seelajaroen, N.S. Sariciftci, Are polyaniline and polypyrrole electrocatalysts for oxygen (O<sub>2</sub>) reduction to hydrogen peroxide (H<sub>2</sub>O<sub>2</sub>)? *ACS Appl. Energy Mater.* 3 (11) (2020) 10611–10618.
- [176] R. Babaei-Sati, J. Basiri Parsa, Electrogeneration of H<sub>2</sub>O<sub>2</sub> using graphite cathode modified with electrochemically synthesized polypyrrole/MWCNT nanocomposite for electro-Fenton process, *J. Ind. Eng. Chem.* 52 (2017) 270–276.
- [177] R. Babaei-Sati, J. Basiri Parsa, Electrodeposition of PANI/MWCNT nanocomposite on stainless steel with enhanced electrocatalytic activity for oxygen reduction reaction and electro-Fenton process, *New J. Chem.* 41 (13) (2017) 5995–6003.
- [178] Y. Chu, H. Su, C. Liu, X. Zheng, Fabrication of sandwich-like super-hydrophobic cathode for the electro-Fenton degradation of cefepime: H<sub>2</sub>O<sub>2</sub> electro-generation, degradation performance, pathway and biodegradability improvement, *Chemosphere* 286 (Pt 2) (2021) 131669.
- [179] L.F. Castañeda, F.C. Walsh, J.L. Nava, C. Ponce de León, Graphite felt as a versatile electrode material: properties, reaction environment, performance and applications, *Electrochim. Acta* 258 (2017) 1115–1139.
- [180] S.K. Chaudhuri, D.R. Lovley, Electricity generation by direct oxidation of glucose in mediatorless microbial fuel cells, *Nat. Biotechnol.* 21 (10) (2003) 1229–1232.
- [181] B. Logan, S. Cheng, V. Watson, G. Estadt, Graphite fiber brush anodes for increased power production in air-cathode microbial fuel cells, *Environ. Sci. Technol.* 41 (9) (2007) 3341–3346.
- [182] M.A. Oturan, An ecologically effective water treatment technique using electrochemically generated hydroxyl radicals for in situ destruction of organic pollutants: application to herbicide 2,4-D, *J. Appl. Electrochem.* 30 (4) (2000) 475–482.
- [183] M.A. Oturan, J. Peiroten, P. Chartrin, A.J. Acher, Complete destruction of p-nitrophenol in aqueous medium by electro-Fenton method, *Environ. Sci. Technol.* 34 (16) (2000) 3474–3479.
- [184] M.A. Oturan, N. Oturan, C. Lahitte, S. Trevin, Production of hydroxyl radicals by electrochemically assisted Fenton's reagent - application to the mineralization of an organic micropollutant, pentachlorophenol, *J. Electroanal. Chem.* 507 (1–2) (2001) 96–102.
- [185] M. Diagne, N. Oturan, M.A. Oturan, Removal of methyl parathion from water by electrochemically generated Fenton's reagent, *Chemosphere* 66 (5) (2007) 841–848.
- [186] M.A. Oturan, E. Guivarch, N. Oturan, I. Sirés, Oxidation pathways of malachite green by Fe<sup>3+</sup>-catalyzed electro-Fenton process, *Appl. Catal. B Environ.* 82 (3–4) (2008) 244–254.
- [187] M. Pimentel, N. Oturan, M. Dezotti, M.A. Oturan, Phenol degradation by advanced electrochemical oxidation process electro-Fenton using a carbon felt cathode, *Appl. Catal. B Environ.* 83 (1–2) (2008) 140–149.
- [188] K. Dong, J. Liang, Y. Wang, Z. Xu, Q. Liu, Y. Luo, T. Li, L. Li, X. Shi, A.M. Asiri, Q. Li, D. Ma, X. Sun, Honeycomb carbon nanofibers: a superhydrophilic O<sub>2</sub> -entrapping electrocatalyst enables ultrahigh mass activity for the two-electron oxygen reduction reaction, *Angew. Chem., Int. Ed. Engl.* 60 (19) (2021) 10583–10587.
- [189] L. Zhou, Z. Hu, C. Zhang, Z. Bi, T. Jin, M. Zhou, Electrogeneration of hydrogen peroxide for electro-Fenton system by oxygen reduction using chemically modified graphite felt cathode, *Separ. Purif. Technol.* 111 (2013) 131–136.
- [190] L. Zhou, M. Zhou, Z. Hu, Z. Bi, K.G. Serrano, Chemically modified graphite felt as an efficient cathode in electro-Fenton for p-nitrophenol degradation, *Electrochim. Acta* 140 (2014) 376–383.
- [191] B. Ou, J.X. Wang, Y. Wu, S. Zhao, Z. Wang, A highly efficient cathode based on modified graphite felt for aniline degradation by electro-Fenton, *Chemosphere* 235 (2019) 49–57.
- [192] Y. Wang, Y. Liu, K. Wang, S. Song, P. Tsiaikaras, H. Liu, Preparation and characterization of a novel KOH activated graphite felt cathode for the electro-Fenton process, *Appl. Catal. B Environ.* 165 (2015) 360–368.
- [193] W.K. Lai, G.Y. Xie, R.Z. Dai, C.Z. Kuang, Y.B. Xu, Z.C. Pan, L. Zheng, L. Yu, S.J. Ye, Z.Y. Chen, H. Li, Kinetics and mechanisms of oxytetracycline degradation in an electro-Fenton system with a modified graphite felt cathode, *J. Environ. Manag.* 257 (2020) 11.
- [194] B. Jiang, Y. Wang, D.F. Wang, M. Yao, C.Y. Fan, J. Dai, Modifying graphite felt cathode by HNO<sub>3</sub> or KOH to improve the degradation efficiency of electro-Fenton for landfill leachate, *Water Sci. Technol.* 80 (12) (2019) 2412–2421.
- [195] Z. Pan, K. Wang, Y. Wang, P. Tsiaikaras, S. Song, In-situ electrosynthesis of hydrogen peroxide and wastewater treatment application: a novel strategy for graphite felt activation, *Appl. Catal. B Environ.* 237 (2018) 392–400.
- [196] L. Zhou, M. Zhou, C. Zhang, Y. Jiang, Z. Bi, J. Yang, Electro-Fenton degradation of p-nitrophenol using the anodized graphite felts, *Chem. Eng. J.* 233 (2013) 185–192.
- [197] W. Zhou, L. Rajic, X. Meng, R. Nazari, Y. Zhao, Y. Wang, J. Gao, Y. Qin, A.N. Alshawabkeh, Efficient H<sub>2</sub>O<sub>2</sub> electrogeneration at graphite felt modified via electrode polarity reversal: utilization for organic pollutants degradation, *Chem. Eng. J.* 364 (2019) 428–439.
- [198] Y. Wang, W. Zhou, J. Gao, Y. Ding, K. Kou, Oxidative modification of graphite felts for efficient H<sub>2</sub>O<sub>2</sub> electrogeneration: enhancement mechanism and long-term stability, *J. Electroanal. Chem.* 833 (2019) 258–268.
- [199] J. Zhou, X.Q. An, H.C. Lan, H.J. Liu, J.H. Qu, New insights into the surface-dependent activity of graphitic felts for the electro-generation of H<sub>2</sub>O<sub>2</sub>, *Appl. Surf. Sci.* 509 (2020) 8.
- [200] F. Yu, L. Tao, T. Cao, High yield of hydrogen peroxide on modified graphite felt electrode with nitrogen-doped porous carbon carbonized by zeolitic imidazolate framework-8 (ZIF-8) nanocrystals, *Environ. Pollut.* 255 (Pt 2) (2019) 113119.
- [201] M.R. Haider, W.-L. Jiang, J.-L. Han, H.M.A. Sharif, Y.-C. Ding, H.-Y. Cheng, A.-J. Wang, In-situ electrode fabrication from polyaniline derived N-doped carbon nanofibers for metal-free electro-Fenton degradation of organic contaminants, *Appl. Catal. B Environ.* 256 (2019).

- [202] F. Yu, M. Zhou, X. Yu, Cost-effective electro-Fenton using modified graphite felt that dramatically enhanced on H<sub>2</sub>O<sub>2</sub> electro-generation without external aeration, *Electrochim. Acta* 163 (2015) 182–189.
- [203] G. Ren, M. Zhou, M. Liu, L. Ma, H. Yang, A novel vertical-flow electro-Fenton reactor for organic wastewater treatment, *Chem. Eng. J.* 298 (2016) 55–67.
- [204] G. Ren, M. Zhou, P. Su, L. Liang, W. Yang, E. Mousset, Highly energy-efficient removal of acrylonitrile by peroxy-coagulation with modified graphite felt cathode: influence factors, possible mechanism, *Chem. Eng. J.* 343 (2018) 467–476.
- [205] Y. Zhang, S. Zuo, Y. Zhang, M. Li, J. Cai, M. Zhou, Disinfection of simulated ballast water by a flow-through electro-peroxone process, *Chem. Eng. J.* 348 (2018) 485–493.
- [206] G.F. Pan, X.P. Sun, Z.R. Sun, Fabrication of multi-walled carbon nanotubes and carbon black co-modified graphite felt cathode for amoxicillin removal by electrochemical advanced oxidation processes under mild pH condition, *Environ. Sci. Pollut. Control Ser. A* 27 (8) (2020) 8231–8247.
- [207] E. Mousset, Z. Wang, J. Hammaker, O. Lefebvre, Physico-chemical properties of pristine graphene and its performance as electrode material for electro-Fenton treatment of wastewater, *Electrochim. Acta* 214 (2016) 217–230.
- [208] T.X.H. Le, M. Bechelany, J. Champavert, M. Cretin, A highly active based graphene cathode for the electro-fenton reaction, *RSC Adv.* 5 (53) (2015) 42536–42539.
- [209] T.X.H. Le, M. Bechelany, S. Lacour, N. Oturan, M.A. Oturan, M. Cretin, High removal efficiency of dye pollutants by electron-Fenton process using a graphene based cathode, *Carbon* 94 (2015) 1003–1011.
- [210] G. Divyapriya, P. Thangadurai, I. Nambi, Green approach to produce a graphene thin film on a conductive LCD matrix for the oxidative transformation of ciprofloxacin, *ACS Sustain. Chem. Eng.* 6 (3) (2018) 3453–3462.
- [211] E. Mousset, Z.T. Ko, M. Syafiq, Z. Wang, O. Lefebvre, Electrocatalytic activity enhancement of a graphene ink-coated carbon cloth cathode for oxidative treatment, *Electrochim. Acta* 222 (2016) 1628–1641.
- [212] E. Mousset, Z. Wang, J. Hammaker, O. Lefebvre, Electrocatalytic phenol degradation by a novel nanostructured carbon fiber brush cathode coated with graphene ink, *Electrochim. Acta* 258 (2017) 607–617.
- [213] G. Divyapriya, I.M. Nambi, J. Senthilnathan, An innate quinone functionalized electrochemically exfoliated graphene/Fe<sub>3</sub>O<sub>4</sub> composite electrode for the continuous generation of reactive oxygen species, *Chem. Eng. J.* 316 (2017) 964–977.
- [214] W. Yang, M. Zhou, J. Cai, L. Liang, G. Ren, L. Jiang, Ultrahigh yield of hydrogen peroxide on graphite felt cathode modified with electrochemically exfoliated graphene, *J. Mater. Chem. 5* (17) (2017) 8070–8080.
- [215] W. Yang, M. Zhou, L. Liang, Highly efficient in-situ metal-free electrochemical advanced oxidation process using graphite felt modified with N-doped graphene, *Chem. Eng. J.* 338 (2018) 700–708.
- [216] P. Su, M. Zhou, X. Lu, W. Yang, G. Ren, J. Cai, Electrochemical catalytic mechanism of N-doped graphene for enhanced H<sub>2</sub>O<sub>2</sub> yield and in-situ degradation of organic pollutant, *Appl. Catal. B Environ.* 245 (2019) 583–595.
- [217] G. Li, Y. Zhang, Highly selective two-electron oxygen reduction to generate hydrogen peroxide using graphite felt modified with N-doped graphene in an electro-Fenton system, *New J. Chem.* 43 (32) (2019) 12657–12667.
- [218] J.M. Friedrich, C. Ponce-de-León, G.W. Reade, F.C. Walsh, Reticulated vitreous carbon as an electrode material, *J. Electroanal. Chem.* 561 (2004) 203–217.
- [219] F.C. Walsh, L.F. Arenas, C. Ponce de León, G.W. Reade, I. Whyte, B.G. Mellor, The continued development of reticulated vitreous carbon as a versatile electrode material: structure, properties and applications, *Electrochim. Acta* 215 (2016) 566–591.
- [220] G. Coria, T. Pérez, I. Sirés, J.L. Nava, Mass transport studies during dissolved oxygen reduction to hydrogen peroxide in a filter-press electrolyzer using graphite felt, reticulated vitreous carbon and boron-doped diamond as cathodes, *J. Electroanal. Chem.* 757 (2015) 225–229.
- [221] E. Petrucci, A. Da Pozzo, L. Di Palma, On the ability to electrogenerate hydrogen peroxide and to regenerate ferrous ions of three selected carbon-based cathodes for electro-Fenton processes, *Chem. Eng. J.* 283 (2016) 750–758.
- [222] Y. Jin, Y. Shi, R. Chen, X. Chen, X. Zheng, Y. Liu, Electrochemical disinfection using a modified reticulated vitreous carbon cathode for drinking water treatment, *Chemosphere* 215 (2019) 380–387.
- [223] Q. Li, C. Batchelor-McAuley, N.S. Lawrence, R.S. Hartshorne, C.J.V. Jones, R.G. Compton, A flow system for hydrogen peroxide production at reticulated vitreous carbon via electroreduction of oxygen, *J. Solid State Electrochem.* 18 (5) (2013) 1215–1221.
- [224] D. Attan, M.A. Alghoul, B.B. Saha, J. Assadeq, K. Sopian, The role of activated carbon fiber in adsorption cooling cycles, *Renew. Sustain. Energy Rev.* 15 (3) (2011) 1708–1721.
- [225] A. Gopinath, K. Kadirvelu, Strategies to design modified activated carbon fibers for the decontamination of water and air, *Environ. Chem. Lett.* 16 (4) (2018) 1137–1168.
- [226] A. Wang, J. Qu, H. Liu, J. Ru, Mineralization of an azo dye Acid Red 14 by photoelectro-Fenton process using an activated carbon fiber cathode, *Appl. Catal. B Environ.* 84 (3–4) (2008) 393–399.
- [227] Y. Gong, J. Li, Y. Zhang, M. Zhang, X. Tian, A. Wang, Partial degradation of levofloxacin for biodegradability improvement by electro-Fenton process using an activated carbon fiber felt cathode, *J. Hazard Mater.* 304 (2016) 320–328.
- [228] H. Lei, H. Li, Z. Li, Z. Li, K. Chen, X. Zhang, H. Wang, Electro-Fenton degradation of cationic red X-GRL using an activated carbon fiber cathode, *Process Saf. Environ. Protect.* 88 (6) (2010) 431–438.
- [229] Y. Zhang, A. Wang, S. Ren, Z. Wen, X. Tian, D. Li, J. Li, Effect of surface properties of activated carbon fiber cathode on mineralization of antibiotic cefalexin by electro-Fenton and photoelectro-Fenton treatments: mineralization kinetics and oxidation products, *Chemosphere* 221 (2019) 423–432.
- [230] W. Zhou, L. Rajic, L. Chen, K. Kou, Y. Ding, X. Meng, Y. Wang, B. Mulaw, J. Gao, Y. Qin, A.N. Alshawabkeh, Activated carbon as effective cathode material in iron-free Electro-Fenton process: integrated H<sub>2</sub>O<sub>2</sub> electrogeneration, activation, and pollutants adsorption, *Electrochim. Acta* 296 (2019) 317–326.
- [231] W. Ren, D. Tang, X. Lu, J. Sun, M. Li, S. Qiu, D. Fan, Novel multilayer ACF@rGO@OMC cathode composite with enhanced activity for electro-fenton degradation of phthalic acid esters, *Ind. Eng. Chem. Res.* 55 (42) (2016) 11085–11096.
- [232] F.K. Yu, L.N. Wang, H.R. Ma, Y.W. Pan, Zeolitic imidazolate framework-8 modified active carbon fiber as an efficient cathode in electro-Fenton for tetracycline degradation, *Separ. Purif. Technol.* 237 (2020) 7.
- [233] J. An, N. Li, Q. Zhao, Y. Qiao, S. Wang, C. Liao, L. Zhou, T. Li, X. Wang, Y. Feng, Highly efficient electro-generation of H<sub>2</sub>O<sub>2</sub> by adjusting liquid-gas-solid three phase interfaces of porous carbonaceous cathode during oxygen reduction reaction, *Water Res.* 164 (2019) 114933.
- [234] E. Brillas, B. Boye, I. Sirés, J.A. Garrido, R.M.a. Rodriguez, C. Arias, P.-L. s. Cabot, C. Comninellis, Electrochemical destruction of chlorophenoxy herbicides by anodic oxidation and electro-Fenton using a boron-doped diamond electrode, *Electrochim. Acta* 49 (25) (2004) 4487–4496.
- [235] C. Flox, S. Ammar, C. Arias, E. Brillas, A.V. Vargas-Zavala, R. Abdelhedi, Electro-Fenton and photoelectro-Fenton degradation of indigo carmine in acidic aqueous medium, *Appl. Catal. B Environ.* 67 (1–2) (2006) 93–104.
- [236] I. Sires, C. Arias, P.L. Cabot, F. Centellas, J.A. Garrido, R.M. Rodriguez, E. Brillas, Degradation of clofibric acid in acidic aqueous medium by electro-Fenton and photoelectro-Fenton, *Chemosphere* 66 (9) (2007) 1660–1669.
- [237] E. Brillas, J.C. Calpe, J. Casado, Mineralization of 2,4-D by advanced electrochemical oxidation processes, *Water Res.* 34 (8) (2000) 2253–2262.
- [238] B. Boye, M.M. Dieng, E. Brillas, Degradation of herbicide 4-chlorophenoxyacetic acid by advanced electrochemical oxidation methods, *Environ. Sci. Technol.* 36 (13) (2002) 3030–3035.
- [239] E. Isarain-Chavez, C. Arias, P.L. Cabot, F. Centellas, R.M. Rodriguez, J.A. Garrido, E. Brillas, Mineralization of the drug beta-blocker atenolol by electro-Fenton and photoelectro-Fenton using an air-diffusion cathode for H<sub>2</sub>O<sub>2</sub> electrogeneration combined with a carbon-felt cathode for Fe<sup>2+</sup> regeneration, *Appl. Catal. B Environ.* 96 (3–4) (2010) 361–369.
- [240] F.C. Moreira, S. Garcia-Segura, R.A.R. Boaventura, E. Brillas, V.J.P. Vilar, Degradation of the antibiotic trimethoprim by electrochemical advanced oxidation processes using a carbon-PTFE air-diffusion cathode and a boron-doped diamond or platinum anode, *Appl. Catal. B Environ.* 160 (2014) 492–505.
- [241] H. Luo, C. Li, C. Wu, X. Dong, In situ electrosynthesis of hydrogen peroxide with an improved gas diffusion cathode by rolling carbon black and PTFE, *RSC Adv.* 5 (80) (2015) 65227–65235.
- [242] M.H.M.T. Assumpção, R.F.B. De Souza, D.C. Rascio, J.C.M. Silva, M.L. Calegario, I. Gaubeur, T.R.L.C. Paixão, P. Hammer, M.R.V. Lanza, M.C. Santos, A comparative study of the electrogeneration of hydrogen peroxide using Vulcan and Printex carbon supports, *Carbon* 49 (8) (2011) 2842–2851.
- [243] W.R.P. Barros, T. Ereno, A.C. Tavares, M.R.V. Lanza, In situ electrochemical generation of hydrogen peroxide in alkaline aqueous solution by using an unmodified gas diffusion electrode, *Chemelectrochem* 2 (5) (2015) 714–719.
- [244] R.M. Reis, A.A.G.F. Beati, R.S. Rocha, M.H.M.T. Assumpção, M.C. Santos, R. Bertazzoli, M.R.V. Lanza, Use of gas diffusion electrode for the in situ generation of hydrogen peroxide in an electrochemical flow-by reactor, *Ind. Eng. Chem. Res.* 51 (2) (2011) 649–654.
- [245] Q. Zhu, Z. Pan, S. Hu, J.-H. Kim, Cathodic hydrogen peroxide electrosynthesis using anthraquinone modified carbon nitride on gas diffusion electrode, *ACS Appl. Energy Mater.* 2 (11) (2019) 7972–7979.
- [246] R.B. Valim, R.M. Reis, P.S. Castro, A.S. Lima, R.S. Rocha, M. Bertotti, M.R.V. Lanza, Electrogeneration of hydrogen peroxide in gas diffusion electrodes modified with tert-butyl-anthraquinone on carbon black support, *Carbon* 61 (2013) 236–244.
- [247] M. Zarei, D. Salari, A. Niaezi, A. Khataee, Peroxi-coagulation degradation of C.I. Basic Yellow 2 based on carbon-PTFE and carbon nanotube-PTFE electrodes as cathode, *Electrochim. Acta* 54 (26) (2009) 6651–6660.
- [248] A.R. Khataee, M. Zarei, L. Moradkhanejad, Application of response surface methodology for optimization of azo dye removal by oxalate catalyzed photoelectro-Fenton process using carbon nanotube-PTFE cathode, *Desalination* 258 (1–3) (2010) 112–119.
- [249] M. Zarei, A. Niaezi, D. Salari, A. Khataee, Application of response surface methodology for optimization of peroxy-coagulation of textile dye solution using carbon nanotube-PTFE cathode, *J. Hazard Mater.* 173 (1–3) (2010) 544–551.
- [250] X.Y. Lu, M.H. Zhou, Y.W. Li, P. Su, J.J. Cai, Y.W. Pan, Improving the yield of hydrogen peroxide on gas diffusion electrode modified with tert-butyl-anthraquinone on different carbon support, *Electrochim. Acta* 320 (2019) 13.
- [251] M.R. Gao, J. Jiang, S.H. Yu, Solution-based synthesis and design of late transition metal chalcogenide materials for oxygen reduction reaction (ORR), *Small* 8 (1) (2012) 13–27.

- [252] Y.Y. Liang, Y.G. Li, H.L. Wang, H.J. Dai, Strongly coupled inorganic/nanocarbon hybrid materials for advanced electrocatalysis, *J. Am. Chem. Soc.* 135 (6) (2013) 2013–2036.
- [253] N. Guillet, L. Roué, S. Marcotte, D. Villers, J.P. Dodelet, N. Chhim, S.T. Vin, Electrogeneration of hydrogen peroxide in acid medium using pyrolyzed cobalt-based catalysts: influence of the cobalt content on the electrode performance, *J. Appl. Electrochem.* 36 (8) (2006) 863–870.
- [254] C. Ridruejo, F. Alcaide, G. Alvarez, E. Brillas, I. Sires, On-site  $H_2O_2$  electro-generation at a  $Co_2$ -based air-diffusion cathode for the electrochemical degradation of organic pollutants, *J. Electroanal. Chem.* 808 (2018) 364–371.
- [255] Z.H. Ye, D.R.V. Guelfi, G. Alvarez, F. Alcaide, E. Brillas, I. Sires, Enhanced electrocatalytic production of  $H_2O_2$  at Co-based air-diffusion cathodes for the photoelectro-Fenton treatment of bronopol, *Appl. Catal. B Environ.* 247 (2019) 191–199.
- [256] Y. Xia, H. Shang, Q. Zhang, Y. Zhou, X. Hu, Electrogeneration of hydrogen peroxide using phosphorus-doped carbon nanotubes gas diffusion electrodes and its application in electro-Fenton, *J. Electroanal. Chem.* 840 (2019) 400–408.
- [257] X. Xu, J. Chen, G. Zhang, Y. Song, F. Yang, Homogeneous electro-Fenton oxidative degradation of reactive brilliant blue using a graphene doped gas-diffusion cathode, *Int. J. Electrochem. Sci.* 9 (2014) 569–579.
- [258] Z. Zhang, H. Meng, Y. Wang, L. Shi, X. Wang, S. Chai, Fabrication of graphene@graphite-based gas diffusion electrode for improving  $H_2O_2$  generation in Electro-Fenton process, *Electrochim. Acta* 260 (2018) 112–120.
- [259] L.J. Cote, F. Kim, J. Huang, Langmuir–Blodgett assembly of graphite oxide single layers, *J. Am. Chem. Soc.* 131 (3) (2009) 1043–1049.
- [260] Q. Su, Y. Liang, X. Feng, K. Mullen, Towards free-standing graphene/carbon nanotube composite films via acetylene-assisted thermolysis of organocobalt functionalized graphene sheets, *Chem. Commun. (Camb.)* 46 (43) (2010) 8279–8281.
- [261] T. Liu, K. Wang, S. Song, A. Brouzgou, P. Tsikararas, Y. Wang, New electro-fenton gas diffusion cathode based on nitrogen-doped Graphene/Carbon nanotube composite materials, *Electrochim. Acta* 194 (2016) 228–238.
- [262] Z. Chen, H. Dong, H. Yu, H. Yu, In-situ electrochemical flue gas desulfurization via carbon black-based gas diffusion electrodes: performance, kinetics and mechanism, *Chem. Eng. J.* 307 (2017) 553–561.
- [263] Y. Zhu, S. Qiu, F. Deng, Y. Zheng, K. Li, F. Ma, D. Liang, Enhanced degradation of sulfathiazole by electro-Fenton process using a novel carbon nitride modified electrode, *Carbon* 145 (2019) 321–332.
- [264] A. Forner-Cuenca, J. Biesdorf, L. Gubler, P.M. Kristiansen, T.J. Schmidt, P. Boillat, Engineered water highways in fuel cells: radiation grafting of gas diffusion layers, *Adv. Mater.* 27 (41) (2015) 6317–6322.
- [265] H. Yamada, T. Hatanaka, H. Murata, Y. Morimoto, Measurement of flooding in gas diffusion layers of polymer electrolyte fuel cells with conventional flow field, *J. Electrochem. Soc.* 153 (9) (2006) A1748–A1754.
- [266] V. Gurau, M.J. Blume, E.S. De Castro, Y.M. Tsou, T.A. Zawodzinski, J.A. Mann, Characterization of transport properties in gas diffusion layers for proton exchange membrane fuel cells 2. Absolute permeability, *J. Power Sources* 165 (2) (2007) 793–802.
- [267] N. Li, J. An, L. Zhou, T. Li, J. Li, C. Feng, X. Wang, A novel carbon black graphite hybrid air-cathode for efficient hydrogen peroxide production in bio-electrochemical systems, *J. Power Sources* 306 (2016) 495–502.
- [268] H. Dong, H. Yu, X. Wang, Catalysis kinetics and porous analysis of rolling activated carbon-PTFE air-cathode in microbial fuel cells, *Environ. Sci. Technol.* 46 (23) (2012) 13009–13015.
- [269] H. Dong, H. Yu, X. Wang, Q. Zhou, J. Feng, A novel structure of scalable air-cathode without Nafion and Pt by rolling activated carbon and PTFE as catalyst layer in microbial fuel cells, *Water Res.* 46 (17) (2012) 5777–5787.
- [270] J. An, N. Li, L. Wan, L. Zhou, Q. Du, T. Li, X. Wang, Electric field induced salt precipitation into activated carbon air-cathode causes power decay in microbial fuel cells, *Water Res.* 123 (2017) 369–377.
- [271] N. Li, J. An, X. Wang, H. Wang, L. Lu, Z.J. Ren, Resin-enhanced rolling activated carbon electrode for efficient capacitive deionization, *Desalination* 419 (2017) 20–28.
- [272] N. Li, Y. Liu, J. An, C. Feng, X. Wang, Bifunctional quaternary ammonium compounds to inhibit biofilm growth and enhance performance for activated carbon air-cathode in microbial fuel cells, *J. Power Sources* 272 (2014) 895–899.
- [273] Q. Zhao, J. An, S. Wang, Y. Qiao, C. Liao, C. Wang, X. Wang, N. Li, Superhydrophobic air-breathing cathode for efficient hydrogen peroxide generation through two-electron pathway oxygen reduction reaction, *ACS Appl. Mater. Interfaces* 11 (38) (2019) 35410–35419.
- [274] Q. Zhao, N. Li, C. Liao, L. Tian, J. An, X. Wang, The UV/ $H_2O_2$  process based on  $H_2O_2$  in-situ generation for water disinfection, *J. Hazardous Mater. Let.* 2 (2021).
- [275] K. Dong, J. Liang, Y. Wang, Z. Xu, Q. Liu, Y. Luo, T. Li, L. Li, X. Shi, A.M. Asiri, Q. Li, D. Ma, X. Sun, Honeycomb carbon nanofibers: a superhydrophilic O<sub>2</sub>-entrapping electrocatalyst enables ultrahigh mass activity for the two-electron oxygen reduction reaction, *Angew. Chem. Int. Ed. Engl.* 60 (19) (2021) 10583–10587.
- [276] W. Xu, Z. Liang, S. Gong, B. Zhang, H. Wang, L. Su, X. Chen, N. Han, Z. Tian, T. Kallio, L. Chen, Z. Lu, X. Sun, Fast and stable electrochemical production of H<sub>2</sub>O<sub>2</sub> by electrode architecture engineering, *ACS Sustain. Chem. Eng.* 9 (20) (2021) 7120–7129.
- [277] Q.Z. Zhang, M.H. Zhou, G.B. Ren, Y.W. Li, Y.C. Li, X.D. Du, Highly efficient electrosynthesis of hydrogen peroxide on a superhydrophobic three-phase interface by natural air diffusion, *Nat. Commun.* 11 (1) (2020) 11.
- [278] W. Zhou, X. Meng, J. Gao, F. Sun, G. Zhao, Janus graphite felt cathode dramatically enhance the  $H_2O_2$  yield from O<sub>2</sub> electroreduction by the hydrophilicity-hydrophobicity regulation, *Chemosphere* 278 (2021) 130382.
- [279] J. An, N. Li, S. Wang, C. Liao, L. Zhou, T. Li, X. Wang, Y. Feng, A novel electro-coagulation-Fenton for energy efficient cyanobacteria and cyanotoxins removal without chemical addition, *J. Hazard. Mater.* 365 (2019) 650–658.
- [280] Q. Zhao, J.K. An, S. Wang, C. Wang, J. Liu, N. Li, Heterotopic formaldehyde biodegradation through UV/ $H_2O_2$  system with biosynthetic H<sub>2</sub>O<sub>2</sub>, *Water Environ. Res.* 91 (7) (2019) 598–605.
- [281] J. An, Y. Feng, N. Wang, Q. Zhao, X. Wang, N. Li, Amplifying anti-flooding electrode to fabricate modular electro-fenton system for degradation of antiviral drug lamivudine in wastewater, *J. Hazard. Mater.* 428 (2021) 128185.
- [282] H. Dong, B.B. Dong, L. Sun, Z.X. Chi, M.Y. Wang, H.B. Yu, Electro-UV/ $H_2O_2$  system with RGO-modified air diffusion cathode for simulative antibiotic-manufacture effluent treatment, *Chem. Eng. J.* 390 (2020) 16.
- [283] W. Zhou, X.X. Meng, L. Rajic, F.Y. Xue, S. Chen, Y.N. Ding, K.K. Kou, Y. Wang, J.H. Gao, Y.K. Qin, A.N. Alshawabek, "Floating" cathode for efficient H<sub>2</sub>O<sub>2</sub> electrogeneration applied to degradation of ibuprofen as a model pollutant, *Electrochim. Commun.* 96 (2018) 37–41.
- [284] Q. Zhang, M. Zhou, Z. Lang, X. Du, J. Cai, L. Han, Dual strategies to enhance mineralization efficiency in innovative electrochemical advanced oxidation processes using natural air diffusion electrode: improving both H<sub>2</sub>O<sub>2</sub> production and utilization efficiency, *Chem. Eng. J.* 413 (2021).
- [285] E. Jung, H. Shin, W.H. Antink, Y.E. Sung, T. Hyeon, Correction to "recent advances in electrochemical oxygen reduction to H<sub>2</sub>O<sub>2</sub>: catalyst and cell design", *ACS Energy Lett.* 5 (XXX) (2020), 2130–2130.
- [286] C. Liu, H. Li, F. Liu, J.S. Chen, Z.X. Yu, Z.W. Yuan, C.J. Wang, H.L. Zheng, G. Henkelman, L. Wei, Y. Chen, Intrinsic activity of metal centers in metal-nitrogen-carbon single-atom catalysts for hydrogen peroxide synthesis, *J. Am. Chem. Soc.* 142 (52) (2020) 21861–21871.
- [287] C. Tang, Q. Zhang, Nanocarbon for oxygen reduction electrocatalysis: dopants, edges, and defects, *Adv. Mater.* 29 (13) (2017).
- [288] Z. Zhao, M. Li, L. Zhang, L. Dai, Z. Xia, Design principles for heteroatom-doped carbon nanomaterials as highly efficient catalysts for fuel cells and metal-air batteries, *Adv. Mater.* 27 (43) (2015) 6834–6840.
- [289] M. Moradi, Y. Vasseghian, A. Khataee, M. Kobya, H. Arabzade, E.N. Dragoi, Service life and stability of electrodes applied in electrochemical advanced oxidation processes: a comprehensive review, *J. Ind. Eng. Chem.* 87 (2020) 18–39.
- [290] P. Cao, X. Quan, K. Zhao, X. Zhao, S. Chen, H. Yu, Durable and selective electrochemical H<sub>2</sub>O<sub>2</sub> synthesis under a large current enabled by the cathode with highly hydrophobic three-phase Architecture, *ACS Catal.* 11 (22) (2021) 13797–13808.
- [291] Y. Li, Y. Zhang, G. Xia, J. Zhan, G. Yu, Y. Wang, Evaluation of the techno-economic feasibility of electrochemical hydrogen peroxide production for decentralized water treatment, *Front. Environ. Sci. Eng.* 15 (1) (2021).
- [292] I. Sirés, E. Brillas, Upgrading and expanding the electro-Fenton and related processes, *Cur. Opin. Electrochem.* 27 (2021).
- [293] S. Mosquera-Romero, A. Prévosteau, I. Vanwonterghem, J.B.A. Arends, L. Dominguez, D.P.L. Rousseau, K. Rabaeij, Hydrogen peroxide in bio-electrochemical systems negatively affects microbial current generation, *J. Appl. Electrochem.* 51 (10) (2021) 1463–1478.
- [294] Z. Lu, W. Xu, J. Ma, Y. Li, X. Sun, L. Jiang, Superaerophilic carbon-nanotube-array electrode for high-performance oxygen reduction reaction, *Adv. Mater.* 28 (33) (2016) 7155–7161.
- [295] F.K. Yu, Y. Chen, Y.W. Pan, Y. Yang, H.R. Ma, A cost-effective production of hydrogen peroxide via improved mass transfer of oxygen for electro-Fenton process using the vertical flow reactor, *Separ. Purif. Technol.* 241 (2020) 8.
- [296] H. Zhang, Y. Li, H. Zhang, G. Li, F. Zhang, A three-dimensional floating air cathode with dual oxygen supplies for energy-efficient production of hydrogen peroxide, *Sci. Rep.* 9 (1) (2019) 1817.
- [297] W. Xu, Z. Lu, X. Sun, L. Jiang, X. Duan, Superwetting electrodes for gas-involving electrocatalysis, *Acc. Chem. Res.* 51 (7) (2018) 1590–1598.
- [298] J. Li, Y. Zhu, W. Chen, Z. Lu, J. Xu, A. Pei, Y. Peng, X. Zheng, Z. Zhang, S. Chu, Y. Cui, Breathing-mimicking electrocatalysis for oxygen evolution and reduction, *Joule* 3 (2) (2019) 557–569.
- [299] O. Garcia-Rodriguez, E. Mousset, H. Olvera-Vargas, O. Lefebvre, Electrochemical treatment of highly concentrated wastewater: a review of experimental and modeling approaches from lab- to full-scale, *Crit. Rev. Environ. Sci. Technol.* (2020) 1–70.
- [300] J. Casado, Towards industrial implementation of Electro-Fenton and derived technologies for wastewater treatment: a review, *J. Environ. Chem. Eng.* 7 (1) (2019).
- [301] F. Alcaide, G. Alvarez, D.R.V. Guelfi, E. Brillas, I. Sirés, A stable CoSP/MWCNTs air-diffusion cathode for the photoelectro-Fenton degradation of organic pollutants at pre-pilot scale, *Chem. Eng. J.* 379 (2020).
- [302] B.S. Tawabini, K.V. Plakas, M. Fraim, E. Safi, T. Oyehan, A.J. Karabelas, Assessing the efficiency of a pilot-scale GDE/BDD electrochemical system in removing phenol from high salinity waters, *Chemosphere* 239 (2020) 124714.
- [303] A. Thiam, R. Salazar, E. Brillas, I. Sirés, Electrochemical advanced oxidation of carbofuran in aqueous sulfate and/or chloride media using a flow cell with a

- RuO<sub>2</sub>-based anode and an air-diffusion cathode at pre-pilot scale, *Chem. Eng. J.* 335 (2018) 133–144.
- [304] I. Salmerón, K.V. Plakas, I. Sirés, I. Oller, M.I. Maldonado, A.J. Karabelas, S. Malato, Optimization of electrocatalytic H<sub>2</sub>O<sub>2</sub> production at pilot plant scale for solar-assisted water treatment, *Appl. Catal. B Environ.* 242 (2019) 327–336.
- [305] H.C. Zhang, Y.J. Li, G.H. Li, F. Zhang, Scaling up floating air cathodes for energy-efficient H<sub>2</sub>O<sub>2</sub> generation and electrochemical advanced oxidation processes, *Electrochim. Acta* 299 (2019) 273–280.
- [306] E. Mousset, D.D. Dionysiou, Photoelectrochemical reactors for treatment of water and wastewater: a review, *Environ. Chem. Lett.* 18 (4) (2020) 1301–1318.
- [307] J.R. Varcoe, P. Atanassov, D.R. Dekel, A.M. Herring, M.A. Hickner, P.A. Kohl, A.R. Kucernak, W.E. Mustain, K. Nijmeijer, K. Scott, Anion-exchange membranes in electrochemical energy systems, *Energy Environ. Sci.* 7 (10) (2014) 3135–3191.